Axel Groß

Theoretical Surface Science: A Microscopic Perspective

Physics – Monograph
(Editorial C. Ascheron)

December 13, 2007

Springer-Verlag
Berlin Heidelberg New York
London Paris Tokyo
Hong Kong Barcelona
Budapest

For Daniella,
Noah and Samira

Preface

More than five years have passed since the first edition of this book was published. Surface science is still a very active field of research, and the fact that the Nobel Prize 2007 in chemistry was awarded to Gerhard Ertl "*for his studies of chemical processes on solid surfaces*" reflects the recognition that surface science has received in recent years. Nevertheless, the traditional surface science approach of studying low-index surfaces and simple adsorbates is no longer the focus topic of the research in this field. Instead, the interest has been shifted to the study of more and more complex structures that are also relevant for nanotechnology and even life sciences. The growing complexity of the studied systems makes a close collaboration between theory and experiment actually more essential in order to gain deeper insights into these systems. In fact, there has also been substantial progress in the theoretical treatment of structures and processes on surfaces. Therefore it was time to revise and update this textbook.

First of all, in this second edition there is a new chapter on *Surface Magnetism* which reflects the growing interest in low-dimensional magnetic structures on surfaces for, e.g., the magnetic storage of data. In addition, all other chapters have been updated in order to take into account novel developments in theoretical surface science. This is reflected in the fact that there are now more than one hundred new references. For example, one of the "hot" topics in surface science is the structure and function of thin oxide films, so-called surface oxides; therefore a discussion of their appropriate theoretical description including some examples was added. Furthermore, the short section about STM theory was expanded, and recent *ab initio* based molecular dynamics simulations of molecular adsorption on surfaces are addressed. All other topics were carefully reviewed and new important results were incorporated.

As far as the chapter on perspectives is concerned, I decided to leave the list of topics unchanged. It is true that in every subject covered in this final chapter there has been significant progress in the last years, which is reflected in the new version of the chapter. However, all these fields have in my opinion not sufficiently matured yet so that it is still justified to consider them as promising subjects that deserve further consideration.

For the new parts of this textbook I am in particular indebted to my colleagues Stefan Blügel, George Kresse, Karsten Reuter and Werner Hofer for

sharing their insights with me. Besides, I want to thank the PostDocs and graduate students of my new research group in Ulm, Benjamin Berberich, Christian Carbogno, Arezoo Dianat, Yoshihiro Gohda, Jan Kucera, Daniela Künzel, Thomas Markert, Christian Mosch, Sung Sakong, Armin Sauter, Sebastian Schnur, Katrin Tonigold. Doing research and teaching together with them provided a most stimulating background for the completion of this second edition. I also would like to acknowledge the continuing support of Claus Ascheron from the Springer-Verlag who initiated the completion of this second edition.

Finally I want to thank my wife Daniella and my children Noah and Samira for their encouragement and for reminding me from time to time that there are also other things beyond theoretical surface science.

Ulm, December 2007 *Axel Groß*

Preface to the First edition

Recent years have seen tremendous progress in the theoretical treatment of surface structures and processes. While a decade ago most theoretical studies tried to describe surfaces either on a qualitative level using empirical parameters or invoked rather severe approximative models, there is now a large class of surface system that can be addressed quantitatively based on first-principles electronic structure methods. This progress is mainly due to advances in the computer power as well as to the development of efficient electronic structure algorithms. However, ab initio studies have not only been devoted to microscopic aspects. Instead, starting from a description of the electronic structure and total energies of surfaces, a hierarchy of methods is employed that allows the theoretical treatment of surfaces from the microscopic length and time scales up to the macroscopic regime. This development has led to a very fruitful cooperation between theory and experiment which is reflected in the large number of research papers that result from a close collaboration between experimental and theoretical groups.

Still, in my opinion, this progress had not been reflected in the available surface science textbooks. I felt that there was a need for an advanced textbook on theoretical surface science. Rather than following a macroscopic thermodynamic approach, the textbook should be based on a microscopic point of view, so-to-say in a bottom-up approach. This provided the motivation to start the project this book resulted from. The text is based on a class on theoretical surface science held at the Technical University in Munich. The class and the manuscript evolved simultaneously, taking into account the feedback from the students attending the class.

I have tried to give a comprehensive overview of most fields of modern surface science. However, instead of listing many different data I have rather picked up some benchmark systems whose description allows the presentation and illustration of fundamental concepts and techniques in theoretical surface science. The theoretical results are compared to experiments where possible, but experimental techniques are not introduced. Still this book is not only meant for students and researchers in theoretical surface science, but also for experimentalists who either are interested in the basic concepts underlying the phenomena at surfaces or want to get an introduction into the methods their theoretical colleagues are using. Of course not every aspect of surface

science could have been covered, for example surface magnetism is hardly touched upon.

I have tried to present derivations for most of the theoretical methods presented in this book. However, I did not intend to overburden this book with lengthy calculations. A detailed list of references is provided for the reader who wants to get more detailed information on specific methods or systems. In particular, I have tried to select excellent comprehensive review papers that can serve as a basis for further reading. For that reason, the reference list does not necessarily reflect the scientific priority, but rather the usefulness for the reader. In this context I would also like to apologize to all colleagues who feel that their own work is not properly presented in this book. It is important to note that in fact I am not the first to use a bottom-up approach in the presentation of first-principles calculations. This concept was developed by Matthias Scheffler for his class on theoretical solid-state physics at the Technical University in Berlin, and in using this concept for the present textbook I am deeply indebted to him.

Such a book would indeed not be possible without interaction with colleagues. I am grateful to my students Arezoo Dianat, Christian Bach, Markus Lischka, Thomas Markert, Christian Mosch, Ataollah Roudgar and Sung Sakong for stimulating discussions in the course of the preparation of this book and for their careful proofreading of the manuscript. Special thanks go to my colleagues and friends Wilhelm Brenig, Peter Kratzer, Eckhard Pehlke and again Matthias Scheffler for their careful and competent reading of the manuscript and their helpful suggestions in order to further improve the book.

This book is also a product of the insight gained in the discussions and collaborations with numerous colleagues, in particular Steve Erwin, Bjørk Hammer, Ulrich Höfer, Dimitrios Papaconstantopoulos, Helmar Teichler, Steffen Wilke, Martin Wolf, and Helmut Zacharias. In addition, I am indebted to Claus Ascheron from Springer-Verlag who supported this book project from the early stages on.

Finally I would like to thank my wife Daniella Koopmann, my son Noah and my yet unborn daughter for their patience and understanding for all the time that I devoted to writing this book instead of taking care of them.

München, April 2002 *Axel Groß*

Contents

1. Introduction

It has always been the goal of theoretical surface science to understand the fundamental principles that govern the geometric and electronic structure of surfaces and the processes occuring on these surfaces like gas-surface scattering, reactions at surfaces or growth of surface layers. Processes on surfaces play an enormously important technological role. We are all surrounded by the effects of these processes in our daily life. Some are rather obvious to us like rust and corrosion. These are reactions that we would rather like to avoid. Less obvious are surface reactions that are indeed very advantageous. Many chemical reactions are promoted tremendously if they take place on a surface that acts as a catalyst. Actually most reactions employed in the chemical industry are performed in the presence of a catalyst. Catalysts are not only used to increase the output of a chemical reaction but also to convert hazardous waste into less harmful products. The most prominent example is the car exhaust catalyst.

The field of modern surface science is characterized by a wealth of microscopic experimental information. The positions of both substrate and adsorbate atoms on surfaces can be determined by scanning microscopes, the initial quantum states of molecular beams hitting a surface can be well-controlled, and desorbing reaction products can be analyzed state-specifically. This provides an ideal field to establish a microscopic theoretical description that can either explain experimental findings or in the case of theoretical predictions can be verified by experiment.

And indeed, recent years have seen a tremendous progress in the microscopic theoretical treatment of surfaces and processes on surfaces. While some decades ago a phenomenological thermodynamic approach was prevalent, now microscopic concepts are dominant in the analysis of surface processes. A variety of surface properties can be described from first principles, i.e. without invoking any empirical parameters.

In fact, the field of theoretical surface science is no longer limited to explanatory purposes only. It has reached such a level of sophistication and accuracy that reliable predictions for certain surface science problems have become possible. Hence both experiment and theory can contribute on an equal footing to the scientific progress. In particular, computational surface science may act as a virtual chemistry and physics lab at surfaces. Computer

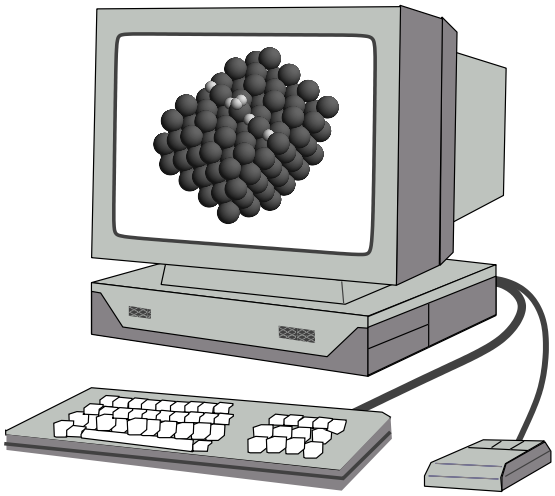

Fig. 1.1. The virtual chemistry and physics lab at surfaces: simulation of surface structures and processes at surfaces on the computer

experiments can thus add relevant information to the research process. Such a computer experiment in the virtual lab is illustrated in Fig. 1.1.

In this book the theoretical concepts and computational tools necessary and relevant for theoretical surface science will be introduced. I will present a microscopic approach towards the theoretical description of surface science. Based on the fundamental theoretical entity, the Hamiltonian, a hierarchy of theoretical methods will be introduced in order to describe surface processes. But even for the largest time and length scales I will develop a statistical rather than a thermodynamic approach, i.e., all necessary parameters will be derived from microscopic properties.

Following this approach, theoretical methods used to describe static properties such as surface structures and dynamical processes such as reactions on surfaces will be presented. An equally important aspect of the theoretical treatment, however, is the proper analysis of the results that leads to an understanding of the underlying microscopic mechanisms. A large portion of the book will be devoted to the establishment of theoretical concepts that can be used to categorize the seemingly immense variety of structures and processes at surfaces. The discussion will be rounded up by the presentation of case studies that are exemplary for a certain class of properties. Thus I will address subjects like surface and adsorbate structures, surface magnetism, reactivity concepts, dynamics and kinetics of processes on surfaces and electronically nonadiabatic effects. All chapters are supplemented by exercises in which the reader is invited either to reproduce some important derivations or to determine typical properties of surfaces.

The theoretical tools employed for surface science problems are not exclusively used for these particular problems. In fact, surface science is a research field at the border between chemistry and solid state physics. Consequently, most of the theoretical methods have been derived either from quantum chemistry or from condensed matter physics. It is outside of the scope of this book to derive all these methods in every detail. However, most of the methods used commonly in theoretical surface science will be addressed and discussed. Hence this book can be used as a reference source for theoretical methods. It is not only meant for graduate students doing research in theoretical surface science but also for experimentalists who want to get an idea about the methods their theoretical colleagues are using.

However, it is fair to say that for a certain class of systems theoretical surface science is still not accurate enough for a reliable description. These problems will be mentioned throughout the book. The open problems and challenges will be presented, but also the opportunities will be illustrated that open up once the problems are solved.

In detail, this book is structured as follows. In the next chapter we first introduce the basic Hamiltonian appropriate for surface science problems. We will consider general properties of this Hamiltonian that are important for solving the Schrödinger equation. At the same time the terminology necessary to describe surface structures will be introduced.

A large part will be devoted to the introduction of electronic structure methods because they are the foundation of any ab initio treatment of surface science problems. Both wave-function and electron-density based methods will be discussed. In addition, the most important techniques used in implementations of electronic structure methods will be addressed.

The structure and energetics of metal, semiconductor and insulators surface are the subject of the following chapter. Using some specific substrates as examples, the different microscopic principles determining the structure of these surfaces will be introduced. In this context, the theoretical treatment of surface phonons is also covered. In the succeeding chapter, the theoretical description of surfaces will be extended to atomic and molecular adsorption systems. Reactivity concepts will be discussed which provide insight into the chemical trends observed in adsorption on clean, precovered and structured surfaces. These concepts are also applied to simple reactions on surfaces.

Magnetic properties of low-dimensional systems can be quite different from those of three-dimensional solids. This is of particular interest due to the tremendous technological importance of the magnetic storage of data. The effects of the dimensionality will be discussed in the chapter on surface magnetism where also the theoretical methods to treat magnetic systems will be briefly introduced.

Dynamics of scattering, adsorption and desorption at surfaces is the subject of the next chapter. Classical and quantum methods to determine the time evolution of processes on surfaces will be introduced. The determina-

tion of reaction probabilities and distributions in gas-surface dynamics will be illustrated. For processes such as diffusion, growth or complex reactions at surfaces, a microscopic dynamical simulation is no longer possible. A theoretical treatment of such processes based on ab initio calculations is still possible using a kinetic approach, as will be shown in the next chapter.

While most of the processes presented in this book are assumed to occur in the electronic ground state, there is an important class of electronically nonadiabatic processes at surfaces. The theoretical description of nonadiabatic phenomena has not reached the same level of maturity as the treatment of electronic ground-state properties, as the following chapter illustrates, but there are promising approaches. Finally, I will sketch future research directions in surface science where theory can still contribute significantly to enhance the understanding, and I will give examples of first successful applications.

2. The Hamiltonian

Any theoretical description has to start with the definition of the system under consideration and a determination of the fundamental interactions present in the system. This information is all contained in the Hamiltonian which is the central quantity for any theoretical treatment. All physical and chemical properties of any system can be derived from its Hamiltonian. Since we are concerned with microscopic particles like electrons and atoms in surface science, the proper description is given by the laws of quantum mechanics. This requires the solution of the Schrödinger equation.

In this chapter we will first describe the Hamiltonian entering the Schrödinger equation appropriate for surface science problems. One general approximation that makes the solution of the full Schrödinger equation tractable is the decoupling of the electronic and nuclear motion which is called the Born–Oppenheimer or adiabatic approximation. We will then have a closer look at the specific form of the Hamiltonian describing surfaces. We will discuss the symmetries present at surfaces. Taking advantage of symmetries can greatly reduce the computational cost in theoretical treatments. Finally, we will introduce and illustrate the nomenclature to describe the structure of surfaces.

2.1 The Schrödinger Equation

In solid state physics as well as in chemistry, the only fundamental interaction we are concerned with is the electrostatic interaction. Furthermore, relativistic effects are usually negligible if only the valence electrons are considered. To start with, we treat core and valence electrons on the same footing and neglect any magnetic effects. Then a system of nuclei and electrons is described by the nonrelativistic Schrödinger equation with a Hamiltonian of a well-defined form,

$$H = T_{\mathrm{nucl}} + T_{\mathrm{el}} + V_{\mathrm{nucl-nucl}} + V_{\mathrm{nucl-el}} + V_{\mathrm{el-el}}\,. \tag{2.1}$$

T_{nucl} and T_{el} are the kinetic energy of the nuclei and the electrons, respectively. The other terms describe the electrostatic interaction between the positively charged nuclei and the electrons. As long as it is not necessary, we will not take the spin into account for the sake of clarity of the equations.

Consequently, neglecting spin the single terms entering the Hamiltonian are explicitly given by

$$T_{\text{nucl}} = \sum_{I=1}^{L} \frac{\boldsymbol{P}_I^2}{2M_I}\,, \tag{2.2}$$

$$T_{\text{el}} = \sum_{i=1}^{N} \frac{\boldsymbol{p}_i^2}{2m}\,, \tag{2.3}$$

$$V_{\text{nucl}-\text{nucl}} = \frac{1}{2}\sum_{I\neq J} \frac{Z_I Z_J e^2}{|\boldsymbol{R}_I - \boldsymbol{R}_J|}\,, \tag{2.4}$$

$$V_{\text{nucl}-\text{el}} = -\sum_{i,I} \frac{Z_I e^2}{|\boldsymbol{r}_i - \boldsymbol{R}_I|}\,, \tag{2.5}$$

and

$$V_{\text{el}-\text{el}} = \frac{1}{2}\sum_{i\neq j} \frac{e^2}{|\boldsymbol{r}_i - \boldsymbol{r}_j|}\,. \tag{2.6}$$

Throughout this book we will use CGS-Gaussian units as it is common practice in theoretical physics textbooks. Atoms will usually be numbered by capital letter indices. Thus, Z_I stands for the charge of the I-th nuclei. The factor $\frac{1}{2}$ in the expressions for $V_{\text{nucl}-\text{nucl}}$ and $V_{\text{el}-\text{el}}$ ensures that the interaction between the same pair of particles is not counted twice.

In principle we could stop here because all what is left to do is to solve the many-body Schrödinger equation using the Hamiltonian (2.1)

$$H\Phi(\boldsymbol{R},\boldsymbol{r}) = E\Phi(\boldsymbol{R},\boldsymbol{r})\,. \tag{2.7}$$

The whole physical information except for the symmetry of the wave functions is contained in the Hamiltonian. In solving the Schrödinger equation (2.7), we just have to take into account the appropriate quantum statistics such as the Pauli principle for the electrons which are fermions. The nuclei are either bosons or fermions, but usually their symmetry does not play an important role in surface science. Often relativistic effects can also be neglected. Only if heavier elements with very localized wave functions for the core electron are considered, relativistic effects might be important since the localization leads to high kinetic energies of these electrons.

Note that only the kinetic and electrostatic energies are directly present in the Hamiltonian. We will later see that the proper consideration of the quantum statistics leads to contributions of the so-called *exchange-correlation energy* in the effective Hamiltonians. However, it is important to realize that the energy gain or cost according to additional effective terms has to be derived from the energy gain or cost in kinetic and electrostatic energy that is caused by the quantum statistics.

Unfortunately, the solution of the Schrödinger equation in closed form is not possible. Even approximative solutions are far from being trivial. In the rest of the book we will therefore be concerned with a hierarchy of approximations that will make possible the solution of (2.7) at least within reasonable accuracy. The first step in this hierarchy will be the so-called Born–Oppenheimer approximation.

2.2 Born–Oppenheimer Approximation

The central idea underlying the Born–Oppenheimer [1] or adiabatic approximation is the separation in the time scale of processes involving electrons and atoms. Except for hydrogen and helium, atoms have a mass that is 10^4 to 10^5 times larger than the mass of an electron. Consequently, at the same kinetic energy electrons are 10^2 to 10^3 times faster than the nuclei. Hence one supposes that the electrons follow the motion of the nuclei almost instantaneously. Most often one simply assumes that the electrons stay in their ground state for any configuration of the nuclei. The electron distribution then determines the potential in which the nuclei moves.

In practice, one splits up the full Hamiltonian and defines the electronic Hamiltonian H_{el} for fixed nuclear coordinates $\{\boldsymbol{R}\}$ as follows

$$H_{\mathrm{el}}(\{\boldsymbol{R}\}) = T_{\mathrm{el}} + V_{\mathrm{nucl-nucl}} + V_{\mathrm{nucl-el}} + V_{\mathrm{el-el}}\,. \tag{2.8}$$

In (2.8) the nuclear coordinates $\{\boldsymbol{R}\}$ do not act as variables but as parameters defining the electronic Hamiltonian. The Schrödinger equation for the electrons for a given fixed configuration of the nuclei is then

$$H_{\mathrm{el}}(\{\boldsymbol{R}\})\Psi(\boldsymbol{r},\{\boldsymbol{R}\}) = E_{\mathrm{el}}(\{\boldsymbol{R}\})\Psi(\boldsymbol{r},\{\boldsymbol{R}\})\,. \tag{2.9}$$

Again, in (2.9) the nuclear coordinates $\{\boldsymbol{R}\}$ are not meant to be variables but parameters. In the Born–Oppenheimer or adiabatic approximation the eigenenergy $E_{\mathrm{el}}(\{\boldsymbol{R}\})$ of the electronic Schrödinger equation is taken to be the potential for the nuclear motion. $E_{\mathrm{el}}(\{\boldsymbol{R}\})$ is therefore called the Born–Oppenheimer energy surface. The nuclei are assumed to move according to the atomic Schrödinger equation

$$\{T_{\mathrm{nucl}} \;+\; E_{\mathrm{el}}(\boldsymbol{R})\}\;\Lambda(\boldsymbol{R}) = E_{\mathrm{nucl}}\Lambda(\boldsymbol{R})\,. \tag{2.10}$$

Often the quantum effects in the atomic motion are neglected and the classical equation of motion are solved for the atomic motion:

$$M_I\frac{\partial^2}{\partial t^2}\boldsymbol{R}_I = -\frac{\partial}{\partial \boldsymbol{R}_I}E_{\mathrm{el}}(\{\boldsymbol{R}\})\,. \tag{2.11}$$

The force acting on the atoms can be conveniently evaluated using the Hellmann–Feynman theorem [2, 3]

$$\mathbf{F}_I = -\frac{\partial}{\partial \boldsymbol{R}_I}E_{\mathrm{el}}(\{\boldsymbol{R}\}) = \langle\Psi(\boldsymbol{r},\{\boldsymbol{R}\})|\frac{\partial}{\partial \boldsymbol{R}_I}H_{\mathrm{el}}(\{\boldsymbol{R}\})|\Psi(\boldsymbol{r},\{\boldsymbol{R}\})\rangle\,. \tag{2.12}$$

In principle, in the Born–Oppenheimer approximation electronic transitions due to the motion of the nuclei are neglected. One can work out the Born–Oppenheimer approximation in much more detail (see, e.g., [4]), however, what it comes down to is that the small parameter m/M is central for the validity of the adiabatic approximation (see Exercise 2.1). In fact, the Born–Oppenheimer approximation is very successful in the theoretical description of processes at surfaces. Still its true validity is hard to prove because it is very difficult to correctly describe processes that involve electronic transition (see Chap. 9).

If it takes a finite amount of energy to excite electronic states, i.e., if the adiabatic electronic states are well-separated, then it can be shown that electronically nonadiabatic transitions are rather improbable (see, e.g., [5]). In surface science this applies to insulator and semiconductor surfaces with a large band gap. At metal surfaces no fundamental band gap exists so that electronic transitions with arbitrarily small excitations energies can occur. Still, the strong coupling of the electronic states in the broad conduction band leads to short lifetimes of excited states and thus to a fast quenching of these states [6] so that their influence on surface processes is often limited.

On the other hand, there are very interesting processes in which electronic nonadiabatic processes are induced, as we will see in Chap. 9. The theoretical treatment of these systems requires special techniques that will also be discussed later in this book.

2.3 Structure of the Hamiltonian

Employing the Born–Oppenheimer approximation means first to solve the electronic structure problem for fixed atomic coordinates. The atomic positions determine the external electrostatic potential in which the electrons move. Furthermore, they determine the symmetry properties of the Hamiltonian.

Surface science studies are concerned with the structure and dynamics of surfaces and the interaction of atoms and molecules with surfaces. If not just ordered surface structures are considered, then the theoretical surface scientists has to deal with a system with only few degrees of freedom, the atom or molecule, interacting with a system, the surface or semi-infinite substrate, that has in principle an infinite number of degrees of freedom. Thus the substrate exhibits a quasi-continuum of states. One faces now the problem that usually different methods are used to treat the single subsystems: molecules are treated by quantum chemistry methods while surfaces are handled by solid-state methods.

To deal with both subsystems on an equal footing represents a real challenge for any theoretical treatment, but it also makes up the special attraction of theoretical surface science. We will focus on this issue in more detail in the next chapter. But before considering a strategy to solve the Schrödinger

3. Electronic Structure Methods and Total Energies

In this chapter, we will discuss electronic structure methods for the determination of total energies of surface systems. The evaluation of total energies is a prerequisite for the theoretical treatment of many properties and processes at surfaces. There are two main techniques, wave-function and electron-density based methods that originate from quantum chemistry and solid-state physics, respectively. Both types of methods will be introduced and discussed in some detail. Special attention will be paid to the discussion of electronic exchange and correlation effects.

Electronic structure calculations for surface science problems are dominated by density functional theory (DFT) methods. Therefore we will have a closer look at some specific implementations of electronic structure algorithms based on DFT. This chapter will be concluded by an introduction to the tight-binding method which is well-suited for a qualitative discussion of band structure effects.

3.1 Hartree–Fock Theory

We start the sections about electronic structure methods with the so-called Hartree and Hartree-Fock methods. This does not only follow the historical development [15,16], but it also allows to introduce important concepts such as self-consistency or electron exchange and correlation.[1] In this whole chapter we are concerned with ways of solving the time-independent electronic Schrödinger equation

$$H_{\mathrm{el}}\Psi(\boldsymbol{r}) = E_{\mathrm{el}}\Psi(\boldsymbol{r})\,. \tag{3.1}$$

Here we have omitted the parametric dependence on the nuclear coordinates (c.f. (2.9)) for the sake of convenience. As already stated, except for the simplest cases there is no way to solve (3.1) in a close analytical form. Hence we have to come up with some feasible numerical scheme to solve (3.1). Mathematically, it corresponds to a second order partial differential equation. There

[1] I thank Matthias Scheffler for providing me with his lecture notes on his theoretical solid-state physics class held at the Technical University Berlin on which the sections about Hartree-Fock and density functional theory are based to a large extent.

are methods to directly integrate partial differential equations (see, e.g., [17]). However, if N is the number of electrons in the system, then we have to deal with a partial differential equation in $3N$ unknowns with N commonly larger than 100. This is completely intractable to solve. The way out is to expand the electronic wave function in some suitable, but necessarily finite basis set whose matrix elements derived from (3.1) can be conveniently determined. This will then convert the partial differential equation into a set of algebraic equations that are much easier to handle. Of course, we have to be aware that by using a finite basis set we will only find an approximative solution to the true many-body wave function. However, by increasing the size of the basis set we have a means to check whether our results are converged with respect to the basis set. Hence this corresponds to a controlled approximation because the accuracy of the calculations can be improved in a systematic way.

Furthermore, for the moment we are mainly interested in the electronic ground-state energy E_0. There is an important quantum mechanical principle – the *Rayleigh–Ritz variational principle* [18] – that provides a route to find approximative solutions for the ground state energy. It states that the expectation value of the Hamiltonian in any state $|\Psi\rangle$ is always larger than or equal to the ground state energy E_0, i.e.

$$E_0 \leq \frac{\langle\Psi|H|\Psi\rangle}{\langle\Psi|\Psi\rangle}\,. \tag{3.2}$$

Hence we can just pick some suitable guess for $|\Psi\rangle$. Then we know that $\langle\Psi|H|\Psi\rangle/\langle\Psi|\Psi\rangle$ will always be an upper bound for the true ground state energy. By improving our guesses for $|\Psi\rangle$, preferentially in a systematic way, we will come closer to the true ground state energy.

Before we proceed, we note that the potential term $V_{\mathrm{nucl-el}}$ (2.5) acts as an effective external one-particle potential for the electrons. Hence we define the external potential for the electrons as

$$v_{ext}(\boldsymbol{r}) = -\sum_{\mathrm{I}} \frac{Z_{\mathrm{I}} e^2}{|\boldsymbol{r} - \boldsymbol{R}_{\mathrm{I}}|}\,. \tag{3.3}$$

Now let us assume that the number of electrons in our system is N and that we have already determined the N lowest eigenfunctions $|\psi_i\rangle$ of the one-particle Schrödinger equation

$$\left\{-\frac{\hbar^2}{2m}\nabla^2 + v_{ext}(\boldsymbol{r})\right\}\psi_i(\boldsymbol{r}) = \varepsilon_i^o \psi_i(\boldsymbol{r})\,. \tag{3.4}$$

Here we have completely neglected the electron-electron interaction. Still, we might simply consider the product wave function

$$\Psi_{\mathrm{H}}(\boldsymbol{r}_1, \ldots, \boldsymbol{r}_{\mathrm{N}}) = \psi_1(\boldsymbol{r}_1) \cdot \ldots \cdot \psi_{\mathrm{N}}(\boldsymbol{r}_{\mathrm{N}})\,, \tag{3.5}$$

in which every one-particle state is only occupied once, as a first crude guess for the true many-particle wave function. Then we can determine the expec-

tation value of the electronic Hamiltonian (2.8) using the wave function (3.5). Thus we obtain

$$\langle \Psi_{\mathrm{H}}|H|\Psi_{\mathrm{H}}\rangle = \sum_{i=1}^{N} \int d^3r \psi_i^*(\boldsymbol{r}) \left(-\frac{\hbar^2}{2m}\nabla^2 + v_{ext}(\boldsymbol{r}) \right) \psi_i(\boldsymbol{r})$$

$$+\frac{1}{2}\sum_{i,j=1}^{N} \int d^3r d^3r' \frac{e^2}{|\boldsymbol{r}-\boldsymbol{r}'|} |\psi_i(\boldsymbol{r})|^2 |\psi_j(\boldsymbol{r}')|^2 + V_{\mathrm{nucl-nucl}}\,. \tag{3.6}$$

Now we would like to minimize the expectation value (3.6) with respect to more suitable single-particle functions $\psi_i(\boldsymbol{r})$ under the constraint that the wave functions are normalized. This is a typical variational problem with the constraint taken into account via Lagrange multipliers. If we consider the wave functions $\psi_i(\boldsymbol{r})$ and $\psi_i^*(\boldsymbol{r})$ as independent, we can minimize (3.6) with respect to the ψ_i^* under the constraint of normalization via

$$\frac{\delta}{\delta\psi_i^*}\left[\langle \Psi_{\mathrm{H}}|H|\Psi_{\mathrm{H}}\rangle - \sum_{i=1}^{N}\{\varepsilon_i(1-\langle\psi_i|\psi_i\rangle)\} \right] = 0\,. \tag{3.7}$$

The ε_i act as Lagrange multipliers ensuring the normalization of the eigenfunctions. This minimization leads to the so-called *Hartree equations* [15]:

$$\left\{ -\frac{\hbar^2}{2m}\nabla^2 + v_{ext}(\boldsymbol{r}) + \sum_{j=1}^{N} \int d^3r' \frac{e^2}{|\boldsymbol{r}-\boldsymbol{r}'|} |\psi_j(\boldsymbol{r}')|^2 \right\} \psi_i(\boldsymbol{r}) = \varepsilon_i \psi_i(\boldsymbol{r})\,. \tag{3.8}$$

The Hartree equations correspond to a mean-field approximation. Equation (3.8) shows that an effective one-particle Schrödinger equation is solved for an electron embedded in the electrostatic field of *all electrons including the particular electron itself*. This causes the so-called *self interaction* which is erroneously contained in the Hartree equations.

Using the electron density

$$n(\boldsymbol{r}) = \sum_{i=1}^{N} |\psi_i(\boldsymbol{r})|^2\,, \tag{3.9}$$

the *Hartree potential* v_{H} can be defined:

$$v_{\mathrm{H}}(\boldsymbol{r}) = \int d^3r' n(\boldsymbol{r}') \frac{e^2}{|\boldsymbol{r}-\boldsymbol{r}'|}\,. \tag{3.10}$$

It corresponds to the electrostatic potential of all electrons. With this definition the Hartree equations can be written in a more compact form as

$$\left\{ -\frac{\hbar^2}{2m}\nabla^2 + v_{ext}(\boldsymbol{r}) + v_{\mathrm{H}}(\boldsymbol{r}) \right\} \psi_i(\boldsymbol{r}) = \varepsilon_i \psi_i(\boldsymbol{r})\,. \tag{3.11}$$

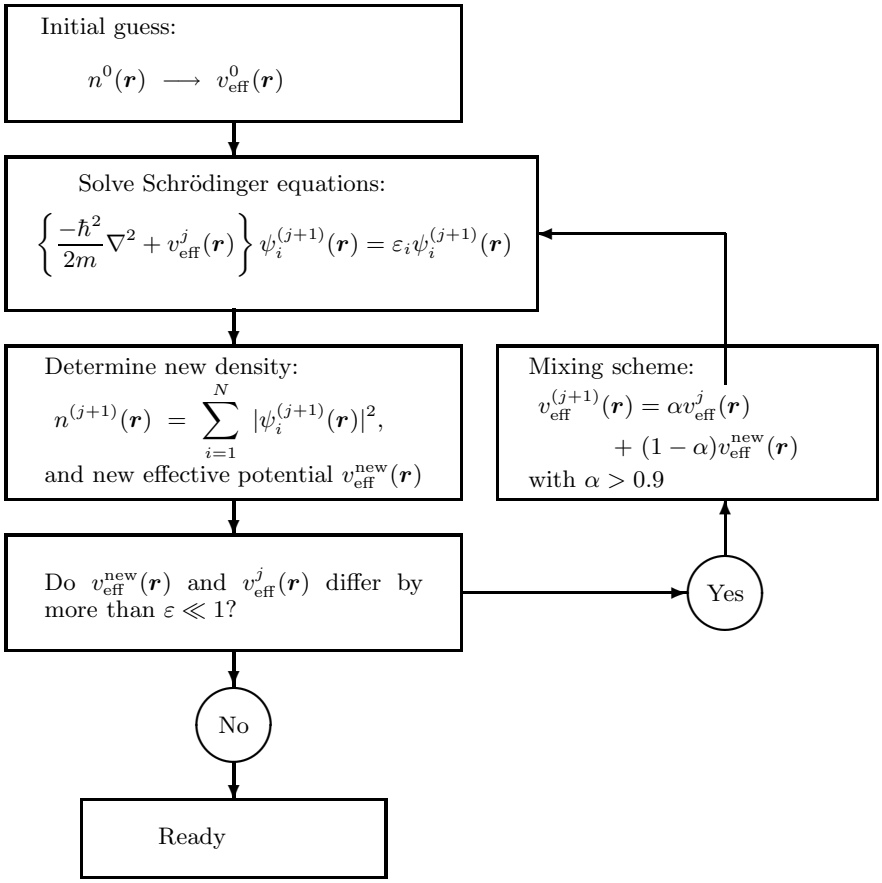

Fig. 3.1. Flow-chart diagram of a self-consistent scheme to solve the Hartree equations

The Hartree equations have the form of one-particle Schrödinger equations. However, the solutions $\psi_i(\boldsymbol{r})$ of the Hartree equations enter the effective one-particle Hamiltonian; hence the exact solutions are needed in order to solve the equations. This dilemma can be resolved in an iterative fashion: One starts with some initial guess for the wave functions which enter the effective one-particle Hamiltonian. The Hartree equations are then solved and a new set of solutions is determined. This cycle is repeated so often until the iterations no longer modify the solutions, i.e. until self-consistency is reached. Methods such as the Hartree approximation that include a self-consistency cycle are also known as *self-consistent field* (SCF) methods.

Such a self-consistent scheme is illustrated in a flow-chart diagram in Fig. 3.1 where we have combined the external and the Hartree potential to an effective potential $v_{\rm eff}(\boldsymbol{r}) = v_{\rm ext}(\boldsymbol{r}) + v_{\rm H}(\boldsymbol{r})$. Furthermore, we have included a

mixing scheme between the new effective potential and the one of the previous step for the construction of the effective potential entering the next iteration cycle. Usually a mixing scheme speeds up the convergence of the iteration scheme significantly; sometimes convergence can even not be reached without a mixing scheme. Note that the general self-consistency cycle depicted in Fig. 3.1 is not only applicable for the solution of the Hartree scheme but for any method that requires a self-consistent solution of one-particle equations.

The expectation value of the total energy in the Hartree approximation E_{H} can be written as

$$\begin{aligned}\langle \Psi_{\mathrm{H}}|H|\Psi_{\mathrm{H}}\rangle &= \sum_{i=1}^{N}\varepsilon_i - \frac{1}{2}\int d^3r d^3r' \frac{e^2 n(\boldsymbol{r})n(\boldsymbol{r}')}{|\boldsymbol{r}-\boldsymbol{r}'|} + V_{\mathrm{nucl-nucl}} \\ &= \sum_{i=1}^{N}\varepsilon_i - V_{\mathrm{H}} + V_{\mathrm{nucl-nucl}} = E_{\mathrm{H}} \end{aligned} \tag{3.12}$$

The integral in (3.12) is the so-called *Hartree energy* V_{H}. It corresponds to the classical (or mean-field) electrostatic energy of the electronic charge distribution. It is contained twice in the Hartree eigenvalue; in order to correct for this double-counting it has to be subtracted in (3.12). In fact, the total energy in (3.12) would only be a sum over single-particle energies if the particles were non-interacting (except for the term $V_{\mathrm{nucl-nucl}}$, which in this context for fixed nuclei just acts as an energy renormalization constant). If we evaluate the total energy for interacting particles by self-consistently solving a set of effective single-particle equations, the total energy is not just a sum over single-particle energies, but there will always be correction terms reflecting the interaction between the particles.

The Hartree ansatz obeys the Pauli principle only to some extent by populating each electronic state once. However, it does not take into account the anti-symmetry of the wave function. The Pauli principle requires that the sign of $|\Psi\rangle$ changes when two electrons are exchanged. The simplest ansatz obeying the antisymmetry requirement is to replace the product wave function (3.5) by a single Slater determinant. In order to correctly incorporate the Pauli principle we have to consider the spin degree of freedom in the following, i.e. we write the single-particle wave functions as $\psi(\boldsymbol{r}\sigma)$, where σ denotes the spin. The Slater determinant is then constructed from the single-particle wave functions by

$$\Psi_{\mathrm{HF}}(\boldsymbol{r}_1\sigma_1,\ldots,\boldsymbol{r}_{\mathrm{N}}\sigma_{\mathrm{N}}) = \frac{1}{\sqrt{N!}}\begin{vmatrix} \psi_1(\boldsymbol{r}_1\sigma_1) & \psi_1(\boldsymbol{r}_2\sigma_2) & \ldots & \psi_1(\boldsymbol{r}_{\mathrm{N}}\sigma_{\mathrm{N}}) \\ \psi_2(\boldsymbol{r}_1\sigma_1) & \psi_2(\boldsymbol{r}_2\sigma_2) & \ldots & \psi_2(\boldsymbol{r}_{\mathrm{N}}\sigma_{\mathrm{N}}) \\ \vdots & \vdots & \ddots & \vdots \\ \psi_{\mathrm{N}}(\boldsymbol{r}_1\sigma_1) & \psi_{\mathrm{N}}(\boldsymbol{r}_2\sigma_2) & \ldots & \psi_{\mathrm{N}}(\boldsymbol{r}_{\mathrm{N}}\sigma_{\mathrm{N}}) \end{vmatrix}. \tag{3.13}$$

Now we follow the same procedure as for the Hartree ansatz; we start by writing down the expectation value of the total energy:

4. Structure and Energetics of Clean Surfaces

In the preceding chapter electronic structure methods were introduced which allow the evaluation of the total energy of a particular system. At zero temperature, the stable structure of a specific system is given by the structure with the minimal total energy. Therefore total-energy calculations are so important for the structural determination of surfaces. As far as finite temperature effects are concerned, the minimum of the free energy is the appropriate quantity. In the following sections, the electronic and geometric structure and the energetics of clean surfaces and their determination by first-principles calculations will be addressed. In addition, the underlying principles that lead to a particular structure will be thoroughly discussed. Since the surface vibrational modes are strongly related to the structure of the surface, surface phonons will also be addressed in this chapter.

4.1 Electronic Structure of Surfaces

Naturally, at the surface of a solid the electronic structure is strongly modified compared to the bulk electronic structure. The three-dimensional periodicity of an infinite crystal is broken so that the wave number k_z of the Bloch waves no longer is a good quantum number. Still the periodicity parallel to the surface is conserved. As we will see, this can lead to electronic bands localized at the surface. Here we will first introduce some basics about the electronic structure at surfaces.

Some fundamental properties of the electronic structure of metal surfaces, in particular simple metal surfaces, can be deduced from a very simple model in which the positive ion charges are replaced by a uniform charge background. In this jellium model, which has already been introduced on p. 26, the positive ion charges at a surface are simply represented by

$$n_+(\boldsymbol{r}) = \begin{cases} \bar{n}, & z \leq 0 \\ 0, & z > 0 \end{cases} . \tag{4.1}$$

Here z denotes, as usual, the direction perpendicular to the surface. The charge density in the jellium model is commonly specified by the corresponding Wigner–Seitz radius in atomic units, i.e., in multiples of the Bohr radius.

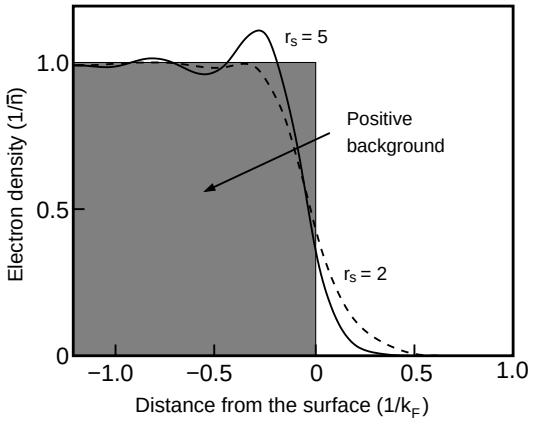

Fig. 4.1. Charge density as a function of the distance from the surface in Fermi wavelengths determined within the jellium model for two different background densities. (After [73])

The electronic charge distribution evaluated within the jellium model using density functional theory in the local density approximation [73] is plotted in Fig. 4.1. Two different background densities have been chosen corresponding to a high-density ($r_s = 2$) and a low-density metal ($r_s = 5$). The electron distribution does not follow the sharp edge of the positive background. Instead, it decreases smoothly and the electrons spill out into the vacuum. In fact this creates an electrostatic dipole layer at the surface because above the surface there is now an excess negative charge density while directly below the jellium edge there is an excess positive charge density. This dipole layer is sometimes also called double layer [11].

Furthermore, the charge density profile exhibits a damped oscillatory structure inside the jellium. These *Friedel oscillations* are a consequence of the sharp edge of the background density in the jellium model. The electrons try to screen out the positive background. Only electrons with wave vectors up to the Fermi wave vector k_F are available while in principle arbitrarily large wave vectors are needed. Thus the screening is incomplete and the Friedel oscillations with wavelength π/k_F result. For the high-density case ($r_s = 2$), however, these oscillations are already rather small.

The work function Φ is defined as the minimum work that must be done to remove an electron from a solid at 0 K. Consider a neutral slab representing the solid. Then the work function is given by

$$\Phi \;=\; \phi(\infty) \;+\; E_{N-1} \;-\; E_N \,. \tag{4.2}$$

Here $\phi(\infty)$ is the total electrostatic potential far from the surface and E_M is the ground-state energy of the slab with M electrons but with an unchanged number of positive charges. As Fig. 4.1 indicates, the spilling out of the electrons at a surface creates a dipole layer. In order to carry the electron

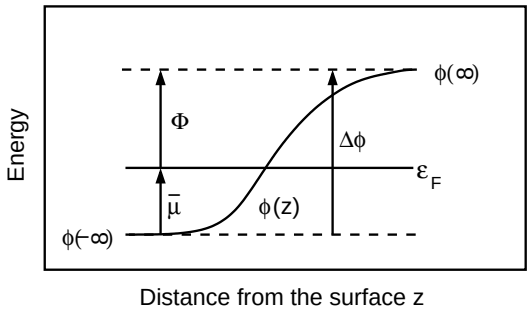

Fig. 4.2. Schematic representation of the electrostatic potential $\phi(z)$, the chemical potential $\bar{\mu}$, and the work function Φ

through the electric field of the dipole double layer at the surface, work has to be done. The work function can therefore be expressed as [74]

$$\begin{aligned} \Phi &= \Delta\phi \; - \; \bar{\mu} \\ &= \phi(\infty) \; - \; \varepsilon_F \; , \end{aligned} \tag{4.3}$$

where $\Delta\phi$ is the change in the electrostatic potential across the dipole layer, $\bar{\mu}$ is the intrinsic chemical potential of the electrons inside the bulk relative to the mean electrostatic potential there (see Fig. 4.2), and ε_F is the Fermi energy. It is important to note that there are two contributions to the work function: an intrinsic one due to the binding of the electrons and the effect of the dipole layer at the surface (see, e.g., the detailed discussion in [11]).

The jellium model has been used to evaluate the work function of simple and noble metals [74]. In order to estimate the variation of the work function from one crystal face to another, the ions have been modeled by pseudopotentials

$$v_{\mathrm{ps}}(\boldsymbol{r}) \; = \; \begin{cases} 0, & r \le r_c \\ -\dfrac{Z}{r}, & r > r_c \end{cases} \; . \tag{4.4}$$

These potentials have been added *a posteori* in this ion lattice model, i.e., the energies and work functions have been evaluated using the electron distribution determined self-consistently within the jellium model without the pseudopotentials.

The calculated values of the work function are compared with experimental results for polycrystalline samples in Fig. 4.3. The plotted results of the ion lattice model correspond to the mean value of the work function for the (110), (100) and (111) surface for the cubic metals and to the (0001) surface for the hcp metals Zn and Mg. For the simple metals there is a rather good agreement between the jellium calculations and the experiment which is even somewhat improved by taking into account the ion lattice contributions. The variations in the work function between the different surface orientations is

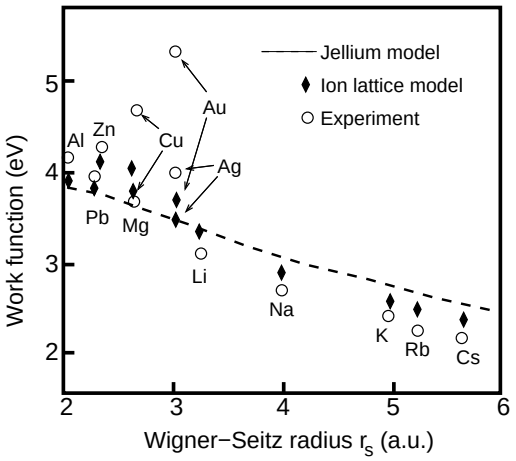

Fig. 4.3. Comparison of theoretical values of the work function obtained in the jellium model and the ion lattice model with the experiment. The experimental values were measured for polycrystalline samples, while the plotted results of the ion lattice gas model correspond to an average over the (110), (100) and (111) surfaces for the cubic metals and to the (0001) surface for the hcp metals Zn and Mg. (After [74])

of the order of 10% of the mean work function [74]. In general, the lowest work function is found for the least densely packed surface considered which is the (110) face for the fcc metals and the (111) face for the bcc metals.

In addition to the simple metals, the work functions for the three noble metals Cu, Au and Ag have been calculated. As Fig. 4.3 demonstrates, there are already large quantitative differences between experiment and jellium calculations for these metals. Although the rather crude jellium model is able to reproduce certain features of the *sp*-bonded simple metals with rather delocalized electron orbitals, the jellium approximation breaks down when it comes to metals with *d* electrons which are much more localized. Thus, for noble and transition metals, a more realistic theoretical description is needed.

Despite its shortcomings, the jellium model is well-suited to describe qualitative aspects of the change of the electron density in *real space* at a surface and related quantities such as the dipole layer. However, it neglects the lattice aspects in the description of the electronic structure at surfaces. These aspects related to the crystal structure can be best addressed qualitatively in the *nearly-free electron model* [11] in which the influence of the screened positive ion cores is approximated by a weak periodic pseudopotential.

Let us first focus on a simplified one-dimensional description. Within the simplest version of the nearly-free electron model, we describe an infinite solid as a chain of atoms creating an effective potential for the electrons given by

$$V(z) \;=\; V_0 \;+ V_G \cos Gz \,, \tag{4.5}$$

where $G = 2\pi/a$ is the shortest reciprocal lattice vector of the chain. Using perturbation theory for degenerate states at the Brillouin zone edge, it is easy to show [12] that the periodic potential causes the opening up of a gap of $E_g = 2V_G$ at the zone boundary (see Exercise 4.1). In the gap, solutions of the one-particle Schrödinger equation with the potential (4.5) also exist, but they correspond to exponentially growing wave functions. Therefore they are physically unreasonable. However, at a surface the wave functions that increase exponentially towards the surface can be matched with wave functions that decay into the vacuum. This leads to the existence of localized states at the surface with energies in the gap that are called *Shockley surface states*.

If the local atomic orbitals are strongly perturbed at the surface, as for example in the case of semiconductor surfaces with broken bonds, additional surface states above and below the bulk continuum can appear. The existence of these so-called Tamm surface states can most easily be derived using a tight-binding description of the surface (see Exercise 3.7).

In the one-dimensional description, the surface state corresponds to a localized *bound* state. In three dimensions, crystal surfaces are still periodic in the lateral directions and can be characterized by a two-dimensional surface Brillouin zone. In other words, the wave vector $k_\parallel$ is still a good quantum number. This leads to a whole band of surface states. On the other hand, due to the broken symmetry in the z-direction, the discrete reciprocal lattice points along the surface normal are turned into rods which reflects that k_z is no longer a good quantum number. In order to analyze the surface band structure and to determine the nature of the electronic states at the surface, the presentation of the projected bulk band structure is rather helpful.

The construction of the projected bulk band structure is illustrated in Fig. 4.4. Two surface state bands are indicated by the solid lines in the band gaps of the projected bulk band structure. The chosen hypothetical example corresponds to a metal since for any energy ε there is at least one bulk state somewhere in the three-dimensional $\boldsymbol{k}$-space. A semiconductor or an insulator would have a band gap completely across the entire surface Brillouin zone (see, e.g., Fig. 4.13).

In the one-dimensional band structure for $\boldsymbol{k} = (0, 0, k_z)$, plotted in Fig. 4.4, two band gaps are present. The lower one is due to the interaction at the Brillouin zone boundary while the upper one results from an avoided crossing of two bands. In such a hybridization gap, also true surface states can exist, as is indicated by the upper surface band. The lower surface band, on the other hand, joins the projected bulk band structure and mixes with delocalized bulk states. By this mixing, a bulk state with a significantly enhanced amplitude at the surface is created. Such a state is called a surface resonance.

The analysis of the band structure is not always a convenient tool for the determination and discussion of the bonding situation a surfaces, in particular when it comes to the understanding of adsorption phenomena [75]. Here, in

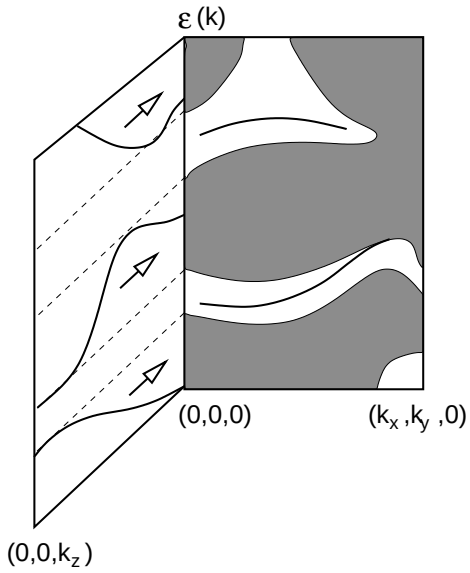

Fig. 4.4. Schematic illustration of the projected bulk band structure which is indicated by the grey-shaded areas. In addition, two surface state bands are included in the band gaps of the projected bulk band structure. While the upper band corresponds to true surface states, the lower surface band mixes with bulk states leading to surface resonances

particular the local density of states $n(\boldsymbol{r}, \varepsilon)$ (LDOS) can be rather useful. The LDOS is defined as

$$n(\boldsymbol{r}, \varepsilon) \;=\; \sum_i \; |\phi_i(\boldsymbol{r})|^2 \; \delta(\varepsilon - \varepsilon_i)\,. \tag{4.6}$$

Using (4.6), the global density of states and the electron density can be conveniently expressed through the following integrals

$$\begin{aligned} n(\varepsilon) &= \int n(\boldsymbol{r}, \varepsilon) \; d^3\boldsymbol{r}\,, \\ n(\boldsymbol{r}) &= \int n(\boldsymbol{r}, \varepsilon) \; d\varepsilon\,. \end{aligned} \tag{4.7}$$

Thus the band-structure energy in the total-energy expression (3.57) can also be written as an integral

$$\sum_{i=1}^{N} \; \varepsilon_i = \int n(\varepsilon) \; \varepsilon \; d\varepsilon\,. \tag{4.8}$$

Furthermore, the projected density of states (PDOS),

$$n_a(\varepsilon) \;=\; \sum_i \; |\langle \phi_i | \phi_a \rangle|^2 \; \delta(\varepsilon - \varepsilon_i)\,, \tag{4.9}$$

is also a useful tool since it allows the determination of the nature and symmetry of chemical bonds. Actually, its analysis is already very illuminating even in the case of a clean surface. In Fig. 4.5, the layer-resolved local d-band density of states is plotted for the three uppermost surface layers of Pd(210).

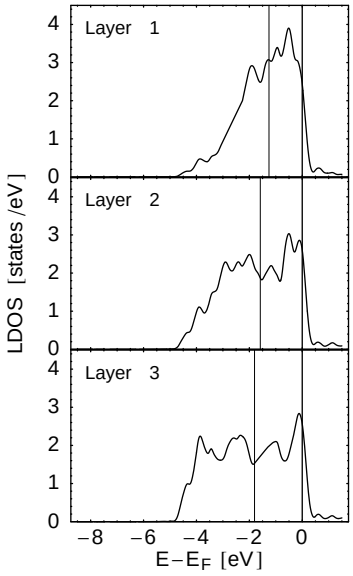

Fig. 4.5. Layer-resolved, local *d*-band density of states of Pd(210) determined by GGA-DFT calculations. The Fermi level and the center of the *d*-band are indicated by vertical lines. The third-layer PDOS is already very close to the bulk density of states of palladium. (After [76])

The electronic structure had been determined by GGA-DFT calculations [76]. The (210) orientation corresponds to a rather open surface that can be regarded as a stepped surface with a high density of steps. Due to the lower coordination of the surface atoms, the *d*-band width is significantly reduced at the surface. Since the number of *d*-electrons remains the same, the local narrowing of the *d*-band leads to an upshift of the *d*-band center which is indicated by the vertical lines in Fig. 4.5. Otherwise the entire *d*-band would be located below the Fermi energy resulting in an increased occupation of the *d*-band. As we will see in the next chapter, the upshift of the *d*-band center leads to a higher reactivity of the surface (see p. 130).

The local *d*-band of the second layer is still somewhat narrower than the Pd bulk *d*-band, but already the third-layer *d*-band is practically indistinguishable from the bulk band. This is a consequence of the good screening properties of metals which lead to a rapid recovery of bulk properties in the vicinity of imperfections, which also includes surfaces.

4.2 Metal Surfaces

After introducing the basic concepts relevant for the discussion of the electronic structure of surfaces, I will first focus on metal surfaces, in particular on first-principles studies of noble and transition metals. Low-index metal surfaces do usually not reconstruct. The electron density of a Cu(100) surface determined by GGA-DFT calculations using ultrasoft pseudopotentials is shown in Fig. 4.6. Recall that the jellium model turned out not to be ap-

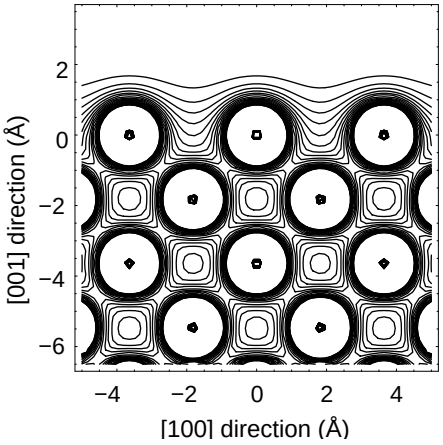

Fig. 4.6. Electron density of a Cu(001) surface along a (010) plane demonstrating electron smoothing at a metal surface. The electronic density has been calculated by DFT-GGA calculations using ultrasoft pseudopotentials

propriate for Cu surfaces (see Fig. 4.3). Figure 4.6 confirms that the electron density of Cu(100) is indeed rather inhomogeneous. Directly at the surface, however, the electron distribution is much smoother than in the bulk. At the surface, the electrons are free to lower their kinetic energy by becoming more uniformly distributed which results in the so-called Smoluchowski smoothing [77].

Let us now turn from the electronic structure in real space to the electronic structure in reciprocal space. The calculated band structure of Cu(111) is shown in Fig. 4.7. The projected bulk d-band is indicated by the darker shaded areas whereas the lighter shaded areas correspond to states of the sp-bands. The sp states exhibit an almost free electron behavior which can be infered from the parabolic shape of the lower and upper band edge. There is a pair of surface states in the upper band gap which also shows nearly-free-electron features. If a parabola $\varepsilon(k) = \hbar^2 k^2/2m^*$ is fitted to the surface band around $\bar{\Gamma}$, a so-called *effective mass* of $m^* = 0.37m_e$ is derived [78]. These surface states correspond to Shockley states in the sp-band gap.

There is another surface state just above the d-band which is located approximately 1.5 eV below the Fermi level. This is a Tamm state which is pushed out of the top of the d-band. Although it lies mostly in the sp-continuum along $\bar{\Gamma}\bar{M}$, it is still a true surface state since it has a different symmetry than the sp-states and is therefore orthogonal to the sp-continuum. There are also surface resonances present at the Cu(111) surface plotted as dashed lines in Fig. 4.7. For example, focus on the Tamm surface state band. This band emanating from $\bar{M}$ bends down and would enter the d-band continuum were it not repelled. At the point where the surface state is repelled, a surface resonance splits off and enters the d-band. Another surface resonance originates at the $\bar{\Gamma}$ point where it is degenerate with the Tamm surface state.

5. Adsorption on Surfaces

The study of adsorption is of central importance in the field of surface science. Adsorption processes are involved in almost all technological processes in which surfaces play a crucial role. Often they are an important step in the preparation of a device as, e.g., in the growth of a semiconductor device. But adsorption can also be of significant importance in industrially relevant processes. The most prominent example is heterogeneous catalysis since usually the reactants have to adsorb on the catalyst before they can react. But of course, also from a fundamental point of view the physical and chemical factors determining adsorption processes are most interesting. In this chapter I will first introduce the basic quantities necessary to describe adsorption. After classifying the different types of adsorption systems the necessary theoretical tools to treat these systems will be addressed. Furthermore, reactivity concepts will be discussed and their usefulness will be demonstrated in some case studies.

5.1 Potential Energy Surfaces

The central quantity in any theoretical description of adsorption is the potential energy surface (PES) of the system. It corresponds to the energy hyperplane over the configuration space of the atomic coordinates of the involved atoms. The PES directly gives information about adsorption sites and energies, vibrational frequencies of adsorbates, reaction paths, and the existence of barriers for adsorption, desorption, diffusion and reactions.

There is a long tradition in surface science of using one-dimensional potential curves to describe adsorption. The most prominent one goes back to Lennard-Jones [148] and is shown in Fig. 5.1. Two curves are plotted: the curve denoted by AB+S represents the potential energy of the molecule AB approaching the surface S. There is a shallow minimum $E_{\mathrm{ad}}^{\mathrm{AB}}$ before the curve rises steeply. The other curve A+B+S corresponds to the interaction of the two widely separated atoms A and B with the surface. Far away from the surface the energetic difference D between the two potential curves is equal to the dissociation energy of the free molecule AB. Close to the surface it is energetically more favorable to have two separate atoms interacting with

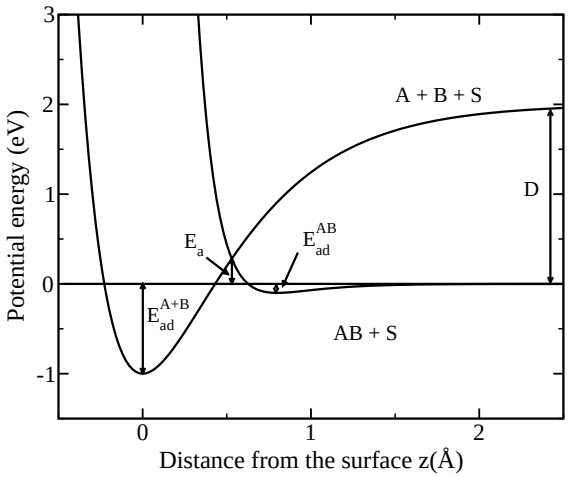

Fig. 5.1. Potential energy curves for molecular and dissociative adsorption according to Lennard-Jones [148]

the surface than the intact molecule. This corresponds to a dissociative adsorption scenario. The energy gain upon the dissociative adsorption of the molecule AB is $E_{\mathrm{ad}}^{\mathrm{A+B}}$ whereas the energy gain upon the adsorption of the two isolated atoms A and B is given by $E_{\mathrm{ad}}^{\mathrm{A+B}} + D$.

The exact location of the crossing point between the curves AB+S and A+B+S determines whether there is a barrier for dissociative adsorption or not. The scenario depicted in Fig. 5.1 illustrates the case of activated dissociative adsorption with the diabatic dissociation barrier given by E_a. The adiabatic barrier will be somewhat lower due to the avoided crossing between the adiabatic potential curves. If the crossing of the two curves is closer to the surface and thus at a potential energy $< 0\,\mathrm{eV}$, the molecule can dissociate spontaneously at the surface and we have non-activated dissociative adsorption.

Potential curves like the ones presented in Fig. 5.1 illustrate the energetics of the adsorption process. However, without any additional information we do not learn anything about the physical and chemical nature of the interaction between the surface and the adsorbates. The shallow molecular adsorption well in Fig. 5.1 usually corresponds to a physisorption well caused by van der Waals attraction while the steep rise of the potential energy is due to the Pauli repulsion between the molecular and substrate wave functions. The energy gain upon dissociative adsorption is typical for the so-called chemisorption which corresponds to the creation of true chemical bonds between adsorbate and substrate. This interaction can be further classified into ionic, metallic or covalent bonding.

In the following sections we will learn how to theoretically describe the interaction of atoms and molecules with surfaces. First we will address physi-

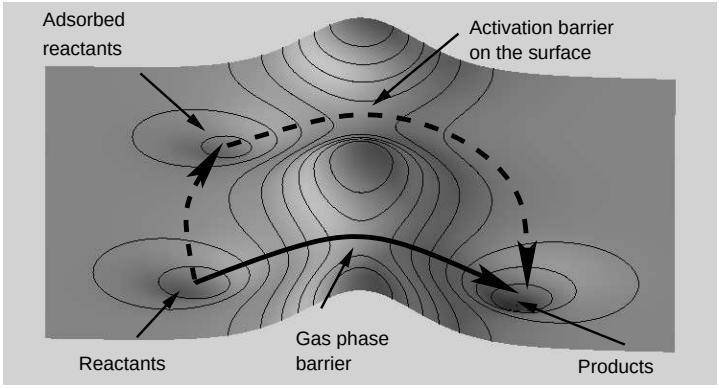

Fig. 5.2. Schematic illustration of the role of a catalyst using a two-dimensional representation of the potential energy surface. A catalyst provides a detour in the multi-dimensional PES with lower activation barriers

sorption which still represents a challenge in density functional theory. In the discussion of chemisorption we will focus on the analysis of the electronic structure which is crucial for the understanding of the nature of the chemical bond.

One note of caution should be added. One-dimensional representations of potential energy surfaces can be quite misleading. For example, it is often argued that the presence of a catalyst lowers activation barriers significantly. However, usually intermediate products are involved in heterogeneous catalysis which can only be illustrated in a multi-dimensional representation of a PES. This is demonstrated in Fig. 5.2. A catalytic reaction corresponds in principle to a detour in the multi-dimensional PES on the path from the reactants to the products. Along this detour, however, the activation barrier is much smaller than for example in the gas phase. Thus the reaction rate is enormously enhanced in the presence of a catalyst since the rate depends exponentially on the barrier height (see Sect. 8.1).

5.2 Physisorption

In the weakest form of adsorption no true chemical bond between surface and adsorbate is established. The bonding is rather due to the induced dipole moment of a nonpolar adsorbate interacting with its own image charges in the polarizable solid, which means that the attraction is caused by van der Waals forces. Although this bonding is usually rather weak ($\sim 0.1\,\mathrm{eV}$), it is in fact crucial for the bonding in a wide range of matter. For example, the exceptional ability of geckos to climb up smooth vertical surfaces is caused by the van der Waals attraction between foot-hairs of the gecko and the surface [149]. Measurements indicate that a single foot of a gecko could produce 100 N of

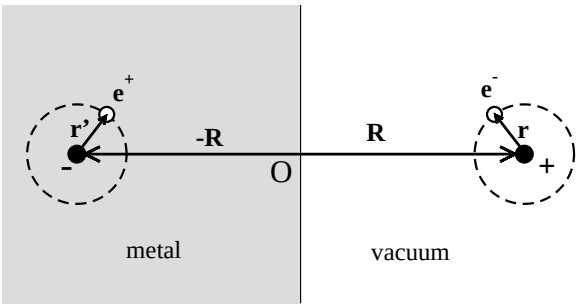

Fig. 5.3. Schematic illustration of a hydrogen atom in front of a perfect conductor interacting with its image charges

adhesive force which means that the feet of a gecko could lift a load of 40 kg. Here we are more concerned with van der Waals interaction of rare gases and molecules with filled electron shells with surfaces since it is the main source of the attraction between these species and surfaces.

I will first give a very elementary introduction into to the essential physics of the van der Waals interaction between an atom and a solid surface [150]. Let us first consider a hydrogen atom in front of a perfect conductor (Fig. 5.3). The positively charged nucleus is located at $\boldsymbol{R} = (0, 0, Z)$, and the electronic coordinates $\boldsymbol{r} = (x, y, z)$ are given with respect to the nucleus. This hydrogen atom is interacting with its image charges of both the nucleus and the electron in the conductor. The total electrostatic energy is then a sum of two repulsive and two attractive terms,

$$\begin{aligned} V_{\rm im} &= -\frac{e^2}{2}\left[\frac{1}{|2\boldsymbol{R}|} + \frac{1}{|2\boldsymbol{R}+\boldsymbol{r}+\boldsymbol{r'}|} - \frac{1}{|2\boldsymbol{R}+\boldsymbol{r}|} - \frac{1}{|2\boldsymbol{R}+\boldsymbol{r'}|}\right] \\ &= -\frac{e^2}{2}\left[\frac{1}{2Z} + \frac{1}{2(Z+z)} - \frac{2}{|2\boldsymbol{R}+\boldsymbol{r}|}\right]. \end{aligned} \tag{5.1}$$

We assume that the atom is not too close to the surface which means that $|\boldsymbol{r}| \ll |\boldsymbol{R}|$. A Taylor expansion of (5.1) in powers of the small quantity $|\boldsymbol{r}|/|\boldsymbol{R}|$ yields

$$V_{\rm im} = -\frac{e^2}{8Z^3}\left[\frac{x^2+y^2}{2} + z^2\right] + \frac{3e^2}{16Z^4}\left[\frac{z}{2}(x^2+y^2) + z^2\right] + O(Z^{-5})\,. \tag{5.2}$$

Let us first consider the leading term of (5.2). The nominator is proportional to the square of the electronic displacement from the nucleus. For the sake of simplicity we model the electronic motion in the free atom by a three-dimensional oscillator:

$$V_{\rm atom}^{\rm free} = \frac{m_e\omega_{\rm vib}^2}{2}\left(x^2+y^2+z^2\right). \tag{5.3}$$

The frequency of the unperturbed oscillator is given by $\omega_{\rm vib}$. The atomic potential (5.3) is modified by the presence of the surface. The image charges

lead to additional potential terms that are quadratic in the displacements. This causes a change in the vibrational frequencies. The modified atomic potential is given by

$$\begin{aligned} V_{\rm atom} &= V_{\rm atom}^{\rm free} \; + \; V_{\rm im} \\ V_{\rm atom} &= \frac{m_e\omega_{\rm vib}^2}{2} \; \left(x^2+y^2+z^2\right) \; - \; \frac{e^2}{8Z^3} \; \left[\frac{x^2+y^2}{2} \; + z^2\right] \; + \ldots \\ &\approx \frac{m_e\omega_\parallel^2}{2} \; \left(x^2+y^2\right) \; + \; \frac{m_e\omega_\perp^2}{2} \; z^2 \, , \end{aligned} \tag{5.4}$$

where the modified vibrational frequencies are

$$\omega_\parallel = \omega_{\rm vib} - \frac{e^2}{16 m_e \omega_{\rm vib} Z^3} \qquad \text{and} \qquad \omega_\perp = \omega_{\rm vib} - \frac{e^2}{8 m_e \omega_{\rm vib} Z^3} \, . \tag{5.5}$$

Here we have used $m_e\omega_{\rm vib}^2 \gg e^2/(4Z)$. If we assume that the atomic oscillator remains in its quantum mechanical ground state, then the van der Waals binding energy in this simple picture is exactly given by the change in the zero-point energy of the atomic oscillator

$$V_{vdW}(Z) = \frac{\hbar}{2} \Delta\omega(Z) = \frac{\hbar}{2}(\omega_\perp(Z) + 2\omega_\parallel(Z) - 3\omega_{\rm vib}) = \frac{-\hbar e^2}{8 m_e \omega_{\rm vib} Z^3} \, . \tag{5.6}$$

This also demonstrates the long-range nature of the van der Waals interaction which is proportional to Z^{-3}.

The van der Waals potential (5.6) can be further simplified by introducing the atomic polarizability

$$\alpha = \frac{e^2}{m_e\omega_{\rm vib}^2} \, . \tag{5.7}$$

Substituting (5.7) into (5.6) yields

$$V_{vdW}(Z) = -\frac{\hbar\omega_{\rm vib}\alpha}{8Z^3} = -\frac{C_v}{Z^3} \tag{5.8}$$

Here $C_v = \hbar\omega_{\rm vib}\alpha/8$ is the van der Waals constant that is directly related to the atomic polarizability.

By writing the fourth-order correction in the Taylor expansion (5.2) as $3C_vZ_0/Z^4$, the so-called *dynamical image plane* at Z_0 is defined

$$V_{\rm im}(Z) = -\frac{C_v}{Z^3} - \frac{3C_vZ_0}{Z^4} + O(Z^{-5}) = -\frac{C_v}{(Z-Z_0)^3} + O(Z^{-5}) \tag{5.9}$$

Note that the $1/Z^3$ long-range van der Waals attraction can also be rationalized from a $1/R^6$ atom-atom dispersion interaction summed over lattice atoms (see Exercise 5.1).

The derivation of the van der Waals force between an hydrogen atom and a perfect conductor given above basically corresponds to the interaction of two dipoles at distance $2Z$. However, a hydrogen atom in the ground state has no permanent dipole moment. Hence there is a rigorous quantum mechanical

derivation necessary of the long-range interaction between a neutral atom and a solid surface. Such a derivation was given by Zaremba and Kohn [151]. They treated the interaction in perturbation theory under the assumption that there is no overlap between the wave functions of the atom and the solid. The full Hamiltonian is given by

$$H = H_a + H_s + V_{as}\,, \tag{5.10}$$

where the subscripts a and s denote the atom and the solid, respectively. The perturbation term V_{as} describes the electrostatic interaction between the atom and the solid

$$V_{as} = \int d^3\boldsymbol{r} d^3\boldsymbol{r}' \frac{\hat{\rho}_s(\boldsymbol{r})\hat{\rho}_a(\boldsymbol{r}')}{|\boldsymbol{r}-\boldsymbol{r}'|}\,, \tag{5.11}$$

where $\hat{\rho}$ corresponds to the total charge density of the positive ion core n^+ and the electron number operator $\hat{n}$,

$$\hat{\rho}_{s,a}(\boldsymbol{r}) = n^+_{s,a}(\boldsymbol{r}) - \hat{n}_{s,a}(\boldsymbol{r})\,. \tag{5.12}$$

It can be shown that the first-order contribution vanishes [151]. The second-order interaction energy $E^{(2)}$ is expressed in terms of the retarded response functions $\chi_{a,s}$ of the atom and the solid, respectively,

$$\begin{aligned} E^{(2)} &= \sum_{\alpha\neq 0}\sum_{\beta\neq 0} \frac{|\langle\psi^a_0\psi^s_0|V'_{as}|\psi^a_\alpha\psi^s_\beta\rangle|}{(E^a_0 - E^a_\alpha) + (E^s_0 - E^s_\beta)} \\ &= -\int d^3\boldsymbol{r}\int d^3\boldsymbol{r}'\int d^3\boldsymbol{x}\int d^3\boldsymbol{x}' \frac{e}{|\boldsymbol{R}+\boldsymbol{x}-\boldsymbol{r}|}\;\frac{e}{|\boldsymbol{R}+\boldsymbol{x}'-\boldsymbol{r}'|} \\ &\quad\times\int_0^\infty \frac{d\omega}{2\pi}\;\chi_a(\boldsymbol{x},\boldsymbol{x}',i\omega)\chi_s(\boldsymbol{r},\boldsymbol{r}',i\omega)\,. \end{aligned} \tag{5.13}$$

Regrouping the terms and integrating over the atomic response function leads to a term proportional to the atomic polarizability α which already appeared in the simple qualitative derivation above. The remaining integrals can be expressed in terms of the dielectric function ϵ of the solid. Finally one arrives at the result that the interaction term $E^{(2)}$ indeed corresponds to the van der Waals atom-metal potential

$$E^{(2)}(Z) = V_{\mathrm{vdW}}(Z) = -\frac{C_v}{(Z-Z_0)^3} + O(Z^{-5})\,, \tag{5.14}$$

where the van der Waals constant is given by

$$C_v = \frac{1}{4\pi}\int_0^\infty d\omega\;\alpha(i\omega)\;\frac{\epsilon(i\omega)-1}{\epsilon(i\omega)+1} \tag{5.15}$$

and the position Z_0 of the dynamical image plane by

Table 5.1. Van der Waals coefficient C_V and dynamical image plane Z_0 for rare-gas atoms on various noble metals obtained by jellium calculations [151]. C_V is given in eV/Å^3 and Z_0 in Å

	He		Ne		Ar		Kr		Xe	
	C_V	Z_0	C_V	Z_0	C_V	Z_0	C_V	Z_0	C_V	Z_0
Cu	0.225	0.22	0.452	0.21	1.501	0.26	2.110	0.27	3.085	0.29
Ag	0.249	0.20	0.502	0.19	1.623	0.24	2.263	0.25	3.277	0.27
Au	0.274	0.16	0.554	0.15	1.768	0.19	2.455	0.20	3.533	0.22

$$Z_0 = \frac{1}{4\pi C_v} \int_0^\infty d\omega \; \alpha(i\omega) \; \frac{\epsilon(i\omega) - 1}{\epsilon(i\omega) + 1} \; \bar{z}(i\omega) \,. \tag{5.16}$$

Here $\bar{z}$ is the centroid of the induced charge density. This derivation confirms that the long-range interaction potential is expressible as a polarization energy. The polarization is due to the interaction of the instantaneous dipole on the atom caused by charge fluctuations with the induced image charge distribution in the solid.

The equations (5.15) and (5.16) provide a convenient scheme to evaluate the van der Waals interaction from first principles. For simple and noble metals the substrate can be reasonably well represented by the jellium model. Calculated values obtained in this way for rare-gas atoms on various noble metal surfaces are listed in Table 5.1 [151]. It is obvious that the van der Waals coefficient increases strongly from He to Ne for all considered metal surfaces. This increase is basically a direct consequence of the larger atomic polarizability of the heavier rare-gas atoms. As far as the dependence on the substrate is concerned, the van der Waals coefficients C_V reflect the increase in the dielectric function from Cu to Au. The positions of the image plane, on the other hand, depend only weakly on the atomic polarizabilities but decrease with increasing dielectric functions. The values for Z_0 are rather small in the order of 0.15–0.3 Å.

The van der Waals interaction (5.14) is purely attractive. However, closer to the surface the wave functions start to overlap with the substrate wave functions. There will be some electrostatic attraction towards the positive ion cores of the substrate. On the other hand, the orbitals of the approaching atom have to be orthogonal to the substrate wave functions which increases their kinetic energy. This Pauli repulsion is particularly strong for atoms with closed valence shells for which it dominates the interaction close to the surface. Thus there will be a balance between the short-range Pauli repulsion and the long-range van der Waals attraction leading to a physisorption minimum. In order to determine the physisorption equilibrium position for rare gases adsorbed on jellium, Zaremba and Kohn divided the total interaction into two parts: a short-range term described by Hartree–Fock theory and the

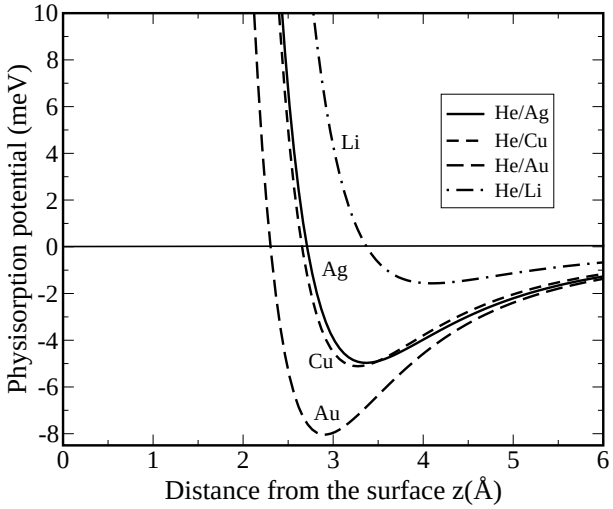

Fig. 5.4. Physisorption potential for He interaction with different jellium surfaces as a function of the distance from the jellium edge. The jellium electronic densities correspond to the noble metals Ag, Cu and Au and the simple metal Li, respectively. (After [152])

longe-range van der Waals interaction. Thus the physisorption potential is given by

$$V(Z) = V_{\mathrm{HF}}(Z) \; + \; V_{\mathrm{vdW}}(Z)\,. \tag{5.17}$$

The physisorption potential for He interaction with jellium surfaces with densities corresponding to Ag, Cu and Au is shown in Fig. 5.4. It is obvious that the attraction due to the van der Waals interaction is rather weak leading to well depths below 10 meV for He. Furthermore Fig. 5.4 demonstrates that the divergence of the van der Waals attraction at $Z_0 \approx 0.2\,\text{Å}$ is irrelevant for physisorption systems since the Pauli repulsion sets in much further away from the surface.

There is, however, a certain inconsistency in the determination of the equilibrium physisorption energy and position using (5.17). In the derivation of the van der Waals attraction $V_{\mathrm{vdW}}(Z)$ (5.14) it was assumed that the wave function were not overlapping while the Pauli repulsion requires a wave function overlap. It would be desirable to have a consistent unified description of both van der Waals interaction and chemical interaction. Unfortunately, density functional theory using the LDA or GGA for the exchange-correlation functional does not properly describe the long-range van der Waals interaction. This is closely related to the fact that in the LDA and the GGA the exchange-correlation hole is still localized. Therefore the effective electron potential outside of a metal falls off exponentially and not proportional to $1/z$. Hence neither image forces nor the van der Waals interaction is appropriately

reproduced. Still there have been calculations of the interaction of rare-gas atoms with surfaces using DFT within the GGA [153] and LDA [154]. These calculations yield reasonable potential well depths for rare-gas adsorption on metal surfaces. It has been argued that this is due to the fact that physisorption can induce a static dipole moment at the adsorbate [154] which is correctly described within LDA or GGA and which contributes significantly to the bond strength [155].

Still there have been several attempts to properly include the van der Waals interaction in density functional theory. Two recent approaches [156, 157] utilize the *adiabatic connection formula*

$$E_{xc}[n] = \frac{1}{2}\int d^3\boldsymbol{r}d^3\boldsymbol{r}'\frac{e^2}{|\boldsymbol{r}-\boldsymbol{r}'|}\int_0^1 d\lambda[\langle\tilde{n}(\boldsymbol{r})\tilde{n}(\boldsymbol{r}')\rangle_{n,\lambda} - \delta(\boldsymbol{r}-\boldsymbol{r}')\langle n(\boldsymbol{r})\rangle]\,. \tag{5.18}$$

For $\lambda = 0$, the Hamiltonian $H(\lambda)$ does not contain any longe-range interaction. This interaction is adiabatically switched on as a function of the coupling parameter λ so that for $\lambda = 1$ the Hamiltonian $H(\lambda)$ corresponds to the true physical Hamiltonian. In (5.18), $\langle\ldots\rangle_{n,\lambda}$ means the expectation value in the ground state $H(\lambda)$ with a potential V_λ which keeps the ground-state density $n_\lambda(\boldsymbol{r})$ equal to the exact physical density $n_{\lambda=1}(\boldsymbol{r})$ for all λ. The advantage of the exact formula (5.18) is that approximate expressions for the interacting system can be used which can still be solved. The adiabatic connection formula then corresponds to an extrapolation to the exact expression.

Hult et al. use second-order perturbation theory equivalent to (5.13) and then introduce a local dielectric function

$$\epsilon(\omega; n(\boldsymbol{r})) = 1 - \kappa(n(\boldsymbol{r}))\,\frac{\omega_p^2(n(\boldsymbol{r}))}{\omega^2} \tag{5.19}$$

with the plasma frequency

$$\omega_p^2(n(\boldsymbol{r})) = \frac{4\pi e^2 n(\boldsymbol{r})}{m_e}\,, \tag{5.20}$$

thus defining a density functional. A cutoff function $\kappa(n(\boldsymbol{r}))$ has to be introduced because the local approximation (5.19) tends to overestimate the response in the low-density tails of the wave functions [157]. Kohn et al. avoid the introduction of a cutoff function by transforming the adiabatic connection formula into the time domain [156].

Both approaches give very satisfactory results for van der Waals constants. However, it would be much more desirable to find a more appropriate nonlocal form for the exchange-correlation functional that reproduces the correct long-range form of the effective one-particle potential. This would avoid the introduction of an explicit van der Waals density functional which requires some extra computational effort to include the long-range van der Waals attraction. Because of this extra effort so far the van der Waals functionals are usually not included in standard DFT implementations.

There is a relativistic modification of the van der Waals potential at distances larger than $Z \sim \lambda/2\pi$, where λ is the effective atomic transition wavelength that contributes to the polarizability. This distance of the order of 0.1 μm. At such a large distance the finite velocity of the photons cannot be neglected which causes retardation effects in the electrostatic interaction. Hence the van der Waals interaction falls off more rapidly with distance and becomes proportional to $-1/Z^4$ [158]. The retarded van der Waals or *Casimir-van der Waals* potential is in fact a manifestation of the *Casimir effect* [159] which is a consequence of the zero-point energy of a quantized field. Although this effect leads to small changes in the attractive potential on an absolute scale, it has still been observed in the scattering of an ultracold beam of metastable neon atoms from silicon and glass surfaces [160].

5.3 Newns–Anderson Model

In contrast to physisorption, in chemisorption true chemical bonds between adsorbate and substrate are formed. This means that there is a significant hybridization between the adsorbate and substrate electronic states which causes a modification of the electronic structure. Let us recall that within the supercell approach the one-electron eigenfunctions of the Kohn–Sham equations are delocalized Bloch functions. In the bulk, their eigenenergies as a function of the crystal momentum $\varepsilon(\boldsymbol{k})$ directly give the electronic band structure which is crucial for the electronic, structural and optical properties of the solid. However, adsorption at surfaces corresponds to the making of localized bonds between the substrate and the adsorbate. The band structure is not a convenient tool for a direct analysis and discussion of the nature of the chemical bonds. Often, an analysis of the local density of states $n(\boldsymbol{r}, \varepsilon)$ (LDOS), in particular the projected density of states, is better suited to analyze the nature and symmetry of chemical bonds between substrate and adsorbate [75].

In order to obtain the change in the density of states upon chemisorption, a full self-consistent electronic structure calculation of the interacting system has to be performed. However, to establish qualitative trends and basic mechanisms, it is often very useful to describe a complex system by a simplified Hamiltonian with a limited number of parameters. The dependence of the properties of the system on these parameters can then be studied in a well-defined way. In the next sections I will discuss approximative theories of chemisorption such as the Newns–Anderson model or the effective medium theory. When these methods were first introduced, they were also meant to provide semiquantitative results for chemisorption properties. Nowadays, due to the relative ease with which self-consistent electronic structure calculations can be performed, these approximative methods are mainly used for explanatory purposes.

6. Surface magnetism

So far, we have entirely ignored any magnetic properties of surfaces. However, the magnetism of surface and interfaces is of great technological interest because of the magnetic storage of data. Furthermore, the so-called spintronics, i.e. spin-dependent charge transport, has also drawn a lot of attention. This has motivated an extensive research of the magnetic properties of surfaces which can be quite different from those of three-dimensional solids. Every solid exhibits magnetic properties related to the properties of the individual atoms or ions, namely *diamagnetism* or *paramagnetism*, which describe the magnetic response of the atoms to an external magnetic field. We do not focus on this kind of magnetism here but rather on magnetic effects that are also present in the absence of any magnetic field, mainly *ferromagnetism* (FM) and *antiferromagnetism* (AF). In order to understand these effects, we will briefly review the theory of the exchange interaction, before discussing the special properties of magnetic surfaces. In fact, in the area of surface magnetism, theory was ahead of the experiment because of difficulties in detecting magnetic properties on the atomic scale. Therefore there are many theoretical predictions, as we will see in this chapter, that have only recently been confirmed by experiment.

6.1 Exchange Interaction

The magnetism of atoms, molecules and solids is mainly related to their electronic properties whereas the magnetic moment of the nuclei can usually be neglected. For free atoms, the magnetic moment of the electrons comes from two contributions, from the angular momentum and from the intrinsic spin of the electrons. Except for the heaviest elements, the particular ground state configuration of the atoms is given by Hund's rules [18].

For solids, the delocalization of the electronic orbitals has to be taken into account. If the overlap of adjacent orbitals is still sufficiently small, as for example for the $4f$ electrons of rare earths elements, the magnetism can be described within a localized picture. In transition metals, on the other hand, such a localized picture is no longer appropriate. Magnetic materials are mainly d-band metals where the magnetic effects originate from the exchange coupling between the d electrons. There is a competition between

these exchange effects and the smearing of the density of state. Broad bands resulting from small nearest-neighbor distances are usually non-magnetic, while transition metals with partially filled d-bands are magnetic for larger volumes and lower densities. As a consequence, a magnetic material such as iron becomes non-magnetic when it is compressed, or conversely, a non-magnetic material such as Pd becomes magnetic upon expansion [262]. With the same arguments, surfaces should show larger magnetic moments as the bulk because of the lower coordination of the atoms.

Although the d-electrons of transition metals are forming bands, they are still rather localized compared to s and p electrons. Therefore the magnetism in these materials is controlled by the hybridization between the d electrons of nearest-neighbor sites. The basic physics underlying the exchange interaction can thus be understood using the simplest molecule, the H_2 molecule, as an example [11]. We will show that a magnetic solution can exist even if no magnetism is explicitly taken into account in the Hamiltonian. The electronic Hamiltonian of a hydrogen molecule for fixed nuclei can be written as

$$\begin{aligned} H = & \frac{\boldsymbol{p}_1}{2m_e} + \frac{\boldsymbol{p_1}}{2m_e} - \frac{e^2}{|\boldsymbol{r}_1 - \boldsymbol{R}_1|} - \frac{e^2}{|\boldsymbol{r}_1 - \boldsymbol{R}_2|} \\ & - \frac{e^2}{|\boldsymbol{r}_2 - \boldsymbol{R}_1|} - \frac{e^2}{|\boldsymbol{r}_2 - \boldsymbol{R}_2|} + \frac{e^2}{|\boldsymbol{r}_1 - \boldsymbol{r}_2|} + \frac{e^2}{|\boldsymbol{R}_1 - \boldsymbol{R}_2|} \,, \end{aligned} \tag{6.1}$$

where $\boldsymbol{p}_i$ and $\boldsymbol{r}_i$ are the momenta and the coordinates of both electrons, respectively, and $\boldsymbol{R}_i$ are the locations of the nuclei, i.e., here the protons. Note that this Hamiltonian does not depend on the spin state of the electrons. Therefore, the two-electron wave function solving the Hamiltonian (6.1) can be separated into a spatial and a spin part,

$$\Psi = \psi(\boldsymbol{r}_1, \boldsymbol{r}_2)\, |m_{s_1} m_{s_2}\rangle \ . \tag{6.2}$$

The spin part consists of a linear combination of the four spin states

$$|\uparrow\uparrow\rangle \,,\ |\uparrow\downarrow\rangle \,,\ |\downarrow\uparrow\rangle \,,\ |\downarrow\downarrow\rangle \ . \tag{6.3}$$

These four states are common eigenvectors of the operators $\boldsymbol{S}_1^2$, $\boldsymbol{S}_2^2$, S_{1z}, and S_{2z}. Alternatively, the spin states may also be expressed in the $\{s, m\}$ or triplet-singlet representation based on the eigenkets of the total spin operator $\boldsymbol{S}^2 = (\boldsymbol{S}_1 + \boldsymbol{S}_2)^2$ and its component S_z along the z-axis:

$$\begin{aligned} |s = 1, m = 1\rangle &= |\uparrow\uparrow\rangle \ , \\ |s = 1, m = 0\rangle &= \left(\frac{1}{\sqrt{2}}\right) (|\uparrow\downarrow\rangle + |\downarrow\uparrow\rangle) \ , \\ |s = 1, m = -1\rangle &= |\downarrow\downarrow\rangle \ , \\ |s = 0, m = 0\rangle &= \left(\frac{1}{\sqrt{2}}\right) (|\uparrow\downarrow\rangle - |\downarrow\uparrow\rangle) \ , \end{aligned} \tag{6.4}$$

The three $|s = 1, m = \pm 1, 0\rangle$ states are referred to as the spin triplet, while $|s = 0, m = 0\rangle$ is called the spin singlet state.

The Pauli exclusion principle requires that the total wave function Ψ is antisymmetric with respect to the interchange of both electrons. The spin singlet state is antisymmetric; hence it has to be coupled with a symmetric spatial wave function. The triplet state, on the other hand, is symmetric with respect to the interchange of the two electrons; therefore the spatial part has to be antisymmetric. We will denote by E_s and E_t the lowest eigenvalues of the singlet (symmetric) and triplet (antisymmetric) solutions of the electronic two-particle Hamiltonian (6.1). The sign of the singlet-triplet splitting $E_s - E_t$ will determine whether the ground state will have spin zero or spin one. It is important to recall that this splitting is a consequence of a spin-independent Schrödinger equation, i.e., there might be a magnetic solution although no magnetic effects are explicitly included.

In order to approximately solve the electronic Schrödinger equation, we follow the so-called *Heitler-London* ansatz of using the single-particle solutions of the isolated hydrogen atom. If we denote with ϕ_i the electronic wave function of the hydrogen atom i, the symmetric and antisymmetric solutions are given by

$$\psi_{s,t}(\boldsymbol{r}_1, \boldsymbol{r}_2) = \frac{1}{\sqrt{2}}\big(\phi_1(\boldsymbol{r}_1)\phi_2(\boldsymbol{r}_2) \pm \phi_1(\boldsymbol{r}_2)\phi_2(\boldsymbol{r}_1)\big)\,. \tag{6.5}$$

The + sign is for the spin singlet, the − sign for the spin triplet. Using these singlet and triplet wave functions, the singlet-triplet splitting can be evaluated in the limit of large spatial separations:

$$\begin{aligned} E_s - E_t \; &= \langle\, \psi_s(\boldsymbol{r}_1, \boldsymbol{r}_2)|H|\psi_s(\boldsymbol{r}_1, \boldsymbol{r}_2)\rangle \;-\; \langle\, \psi_t(\boldsymbol{r}_1, \boldsymbol{r}_2)|H|\psi_t(\boldsymbol{r}_1, \boldsymbol{r}_2)\rangle \\ &= 2\int d^3r_1 d^3r_2\, \phi_1(\boldsymbol{r}_1)\phi_2(\boldsymbol{r}_2)\, \left(\frac{e^2}{|\boldsymbol{r}_1 - \boldsymbol{r}_2|} + \frac{e^2}{|\boldsymbol{R}_1 - \boldsymbol{R}_2|}\right. \\ &\quad \left. - \frac{e^2}{|\boldsymbol{r}_1 - \boldsymbol{R}_1|} - \frac{e^2}{|\boldsymbol{r}_2 - \boldsymbol{R}_2|}\right) \phi_1(\boldsymbol{r}_2)\phi_2(\boldsymbol{r}_1)\,. \end{aligned} \tag{6.6}$$

This singlet-triplet splitting arises from a matrix element between two two-electron states that differ only through the exchange of the coordinates of the electrons; this difference is therefore referred to as the *exchange splitting*. Since the electronic hydrogen wave functions are strongly localized close to the nuclei, the exchange splitting falls off rapidly with increasing distance $|\boldsymbol{R}_1 - \boldsymbol{R}_2|$.

If one only considers the singlet and triplet states, then the two-particles Hamiltonian (6.1) can be cast into a form in which the spin explicitly appears and whose eigenfunctions give the spin of the corresponding state. First we note that

$$\boldsymbol{S}^2 \;=\; (\boldsymbol{S}_1 + \boldsymbol{S}_2)^2 \;=\; \boldsymbol{S}_1^2 + \boldsymbol{S}_2^2 + 2\,\boldsymbol{S}_1 \cdot \boldsymbol{S}_2 \;=\; \frac{3}{2}\,\mathbf{1} \;+\; 2\,\boldsymbol{S}_1 \cdot \boldsymbol{S}_2\;, \tag{6.7}$$

where $\mathbf{1}$ here is the 2×2 unit matrix and where we have used the fact that each individual spin operator satisfies $\boldsymbol{S}_i^2 = \frac{1}{2}(\frac{1}{2} + 1) = \frac{3}{4}$. The total spin operator $\boldsymbol{S}^2$ has the eigenvalues $s(s+1)$. Therefore it is easy to see from

(6.7) that the operator $\boldsymbol{S}_1 \cdot \boldsymbol{S}_2$ has the eigenvalues $-\frac{3}{4}$ in the singlet state ($s = 0$) and $+\frac{1}{4}$ in the triplet state ($s = 1$). Then the eigenvalues of the Hamiltonian

$$H_{\text{spin}} = \frac{1}{4}(E_s + 3E_t) - (E_s - E_t)\,\boldsymbol{S}_1 \cdot \boldsymbol{S}_2 \tag{6.8}$$

are E_s in the singlet state and E_t in each of the three triplet states. This Hamiltonian is referred to as the *spin Hamiltonian*. We can further simplify this spin Hamiltonian by redefining the energy zero so that the constant $(E_s + 3E_t)/4$ vanishes. Thus we get

$$H_{\text{spin}} = -J\,\boldsymbol{S}_1 \cdot \boldsymbol{S}_2 \;, \tag{6.9}$$

where the exchange coupling parameter J corresponds to the singlet-triplet splitting

$$J = (E_s - E_t) \;. \tag{6.10}$$

If J is positive, it is energetically favorable for both spins to be parallel while for negative J the antiparallel configuration is favored.

This derivation for the spin Hamiltonian of the H_2 molecule can be generalized to the case of a solid. If the overlap of the electronic wave functions is rather small, the spin Hamiltonian of a solid can be written as

$$H_{\text{spin}} = -\frac{1}{2}\sum_{i \neq j} J_{ij}\,\boldsymbol{S}_i \cdot \boldsymbol{S}_j \;. \tag{6.11}$$

where the factor $1/2$, as usual, corrects for the double counting. This Hamiltonian is called the *Heisenberg Hamiltonian*, and the coupling constants J_{ij} are known as the exchange coupling constants.

Although the Hamiltonian (6.11) looks rather simple, solving the corresponding Schrödinger equation is far from being trivial. Still one has to take into account that (6.11) only represents an approximate description of magnetic properties caused by the electron-electron interaction.

Because of magnetic interactions, the individual atoms of some solids show non-vanishing magnetic moments below a critical temperature T_c. Those solids are called *magnetically ordered*. If the exchange coupling parameters are all positive, i.e. $J_{ij} = J_{ji} \geq 0$, the material exhibits a *spontaneous magnetization*, and the single localized moments add up to a macroscopic net magnetization density even in the absence of a magnetic field. This ordered state is called *ferromagnetic*. However, it is more common that the individual magnetic moments do not add up to a macroscopic magnetic moment but rather yield a zero total moment. These magnetically ordered states are called *antiferromagnetic* resulting from a Hamiltonian of the form

$$H = \frac{1}{2}\sum_{i \neq j \; n.n.} |J_{ij}|\,\boldsymbol{S}_i \cdot \boldsymbol{S}_j \;. \tag{6.12}$$

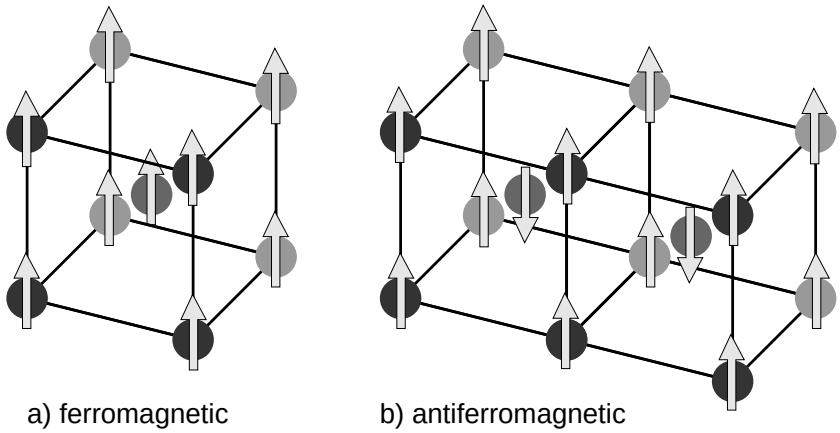

Fig. 6.1. Simple magnetically ordered structures on a body-centered cubic lattice. a) Ferromagnetic structure, b) antiferromagnetic structure.

The simplest cases of ferromagnetic and antiferromagnetic ordering are illustrated in Fig. 6.1 for a body-centered cubic lattice. In Fig. 6.1a, the ferromagnetic structure, all magnetic moments have the same magnitude and direction. The simplest antiferromagnetic structure results from two identical interpenetrating sublattices with magnetic moments of the same magnitude but opposite direction. The bcc lattice can be regarded as two interpenetrating simple cubic sublattices. Fig. 6.1b demonstrates how antiferromagnetic ordering results if these two sublattices have opposite magnetic moments.

In general, the ordered magnetic structures can be much more complicated. If, for example, the two interpenetrating sublattices are occupied by two different kinds of atoms with an antiparallel alignment of the magnetic moments, there will usually be a net magnetic moment when the moments of the two kinds of atoms do not exactly cancel. Such a solid is called *ferrimagnetic*.

For the occurrence of ferromagnetism, there is in fact a simple criterion, the so-called *Stoner criterion*. The total electron density can be divided into spin-dependent densities, $n_\uparrow$ and $n_\downarrow$. Using these densities, the total electron density n and the spin density m can be expressed as

$$n = n_\uparrow + n_\downarrow \,, \qquad m = n_\uparrow - n_\downarrow \,. \tag{6.13}$$

Within a mean-field Hubbard Hamiltonian approach, the energy of a system of N atoms with total spin $S_z = \frac{1}{2}mN$ can be written as

$$E(S_z) = \sum_\sigma \sum_i \varepsilon_{i\sigma} + \frac{1}{4} NI \left(n^2 - m^2\right) \,, \tag{6.14}$$

The first term is the band-structure energy (4.8), while the second term is the exchange term that leads to a stabilization of the magnetic solution for

$m > 0$. I is the Stoner parameter that is related to the exchange interaction. However, changing the system from being paramagnetic to ferromagnetic leads to a rearrangement of the band occupation that in general costs energy. If we assume that the exchange splitting between spin up and spin down states is small and that the density of states at the Fermi level $n(\varepsilon_F)$ is constant close to the Fermi energy and almost the same for both $\sigma =\uparrow$ and $\sigma =\downarrow$ spin states, then the change of the charge density δn and the spin density $m = n_\uparrow - n_\downarrow$ are given by

$$\begin{aligned} \delta n &= n(\varepsilon_F)\left(\delta\varepsilon_\uparrow + \delta\varepsilon_\downarrow\right)/N = 0 \\ m &= n(\varepsilon_F)\left(\delta\varepsilon_\uparrow + \delta\varepsilon_\downarrow\right)/N = 2g_(\varepsilon_F)\delta\varepsilon\,, \end{aligned} \tag{6.15}$$

where $g(\varepsilon_F) = n(\varepsilon_F)/N$ is the density of states per electron at the Fermi level. It is a simple exercise (see Exercise 6.1) to show that under the conditions of Eq. (6.15) the rearrangement of the band occupation corresponds to a change in the band-structure energy (4.8) of

$$\Delta E_{\rm bs} = \frac{N^2}{4}\frac{m^2}{n(\varepsilon_F)} = \frac{N}{4}\frac{m^2}{g(\varepsilon_F)} \tag{6.16}$$

Thus the creation of the ferromagnetic phase is associated with the energy

$$\begin{aligned} \Delta E_{\rm fm} &= E(S_z = \frac{1}{2}mN) - E(S_z = 0) \\ &= \frac{N}{4}\left(\frac{1}{g(\varepsilon_F)} - I\right)\, m^2\,. \end{aligned} \tag{6.17}$$

This leads to the Stoner criterion that a ferromagnetic phase may form for

$$I\, g(\varepsilon_F) \;>\; 1\;. \tag{6.18}$$

6.2 Spin-density Formalism

The first-principles treatment of magnetism in solids and surfaces is usually based on the spin-polarized density functional theory introduced by von Barth and Hedin in 1972 [263] who developed a generalization of the Hohenberg-Kohn theorem for the spin-dependent case. In a fully relativistic treatment, magnetism appears naturally, but in a non-relativistic framework, the magnetic coupling has to be explicitly included. The energy functional of a general magnetic system can be expressed as a functional of the Hermitian 2×2 density matrix ρ which is defined by

$$\rho = \frac{1}{2}\left(n\mathbf{1} + \boldsymbol{\sigma}\cdot\boldsymbol{m}\right) = \frac{1}{2}\begin{pmatrix} n + m_z & m_x - im_y \\ m_x + im_y & n + m_z \end{pmatrix}\,, \tag{6.19}$$

where $\mathbf{1}$ is again the 2×2 unit matrix and $\boldsymbol{\sigma}$ is the vector of the Pauli matrices. n and $\boldsymbol{m}$ are the charge density and the magnetization density

vector field which in the two-component formalism can be expressed in terms of the Kohn-Sham orbitals $\boldsymbol{\psi}_i = (\psi_{i,1}, \psi_{i,2})$ as

$$\begin{aligned} n(\boldsymbol{r}) &= \sum_{i=1}^{N} \boldsymbol{\psi}_i^\dagger(\boldsymbol{r})\, \mathbf{1}\, \boldsymbol{\psi}_i(\boldsymbol{r}) \\ \boldsymbol{m}(\boldsymbol{r}) &= \sum_{i=1}^{N} \boldsymbol{\psi}_i^\dagger(\boldsymbol{r})\, \boldsymbol{\sigma}\, \boldsymbol{\psi}_i(\boldsymbol{r})\,. \end{aligned} \tag{6.20}$$

It is left as an exercise (see problem 6.2) that the density matrix (6.19) can be written as

$$\rho_{kl} = \sum_{i=1}^{N} \psi_{i,k}^* \psi_{i,l}\ , \quad k,l = 1,2\,. \tag{6.21}$$

In the two-component spinor formalism, the potential matrix $\mathbf{V}$ is expressed as

$$\mathbf{V} = V\,\mathbf{1} + \mu_{\mathrm{B}}\, \boldsymbol{\sigma} \cdot \boldsymbol{B}\,. \tag{6.22}$$

The first term contains the external, the Hartree, and the exchange-correlation potential averaged over the two spin directions. μ_B is Bohr's magneton, and the vector $\boldsymbol{B}$ incorporates the external magnetic field B and the difference of the spin-dependent exchange-correlation potential $\frac{1}{2}\left(v_{xc}(\uparrow) - v_{xc}(\downarrow)\right)$ in a local frame of reference where the z axis is parallel to the quantization axis. In the local spin-density approximation (LSDA), the exchange-correlation energy is written as

$$E_{\mathrm{xc}}^{\mathrm{LSDA}}[\rho_{kl}] = \int d^3\boldsymbol{r}\ \left\{\rho^+(\boldsymbol{r}) + \rho^-(\boldsymbol{r})\right\}\ \varepsilon_{\mathrm{xc}}^{\mathrm{LDA}}(\rho^+(\boldsymbol{r}), \rho^-(\boldsymbol{r}))\,, \tag{6.23}$$

where $\rho^+(\boldsymbol{r})$ and $\rho^-(\boldsymbol{r})$ are the eigenvalues of the density matrix $\rho_{kl}(\boldsymbol{r})$. The exchange correlation potential in the LSDA is then given by

$$v_{\mathrm{xc}}^{(\alpha)} = \frac{\partial}{\partial \rho^{(\alpha)}} \left\{\left(\rho^+(\boldsymbol{r}) + \rho^-(\boldsymbol{r})\right)\ \varepsilon_{\mathrm{xc}}^{\mathrm{LDA}}(\rho^+(\boldsymbol{r}), \rho^-(\boldsymbol{r}))\right\}\,. \tag{6.24}$$

Note that there are also spin-polarized versions of all popular GGA functionals.

Using the expression (6.22), the Kohn-Sham equations become

$$\left\{-\frac{\hbar^2}{2m}\nabla^2\,\mathbf{1} + \mathbf{V}\right\}\,\boldsymbol{\psi}_k = \varepsilon_k\,\boldsymbol{\psi}_k\,. \tag{6.25}$$

While the kinetic part of the Hamiltonian is diagonal in the two-dimensional spin space, the two components of the Pauli spinor $\boldsymbol{\psi}_k$ can only be coupled by the off-diagonal elements of the potential matrix. If the B field is collinear, the coordinate system can always be chosen in such a way that the B fields are oriented in the z direction. Then the total Hamiltonian is diagonal in

spin space. This means that the spin-up and the spin-down problem decouple so that they can be treated almost independently as two non-magnetic calculations.

There are, however, situations where the spins are not aligned in a collinear way. The proper theoretical treatment of such non-collinear spin structures is much more involved [264–266]. In addition, the calculations also become computationally much more demanding. The spin-up and spin-down problems can no longer be solved separately so that the Hamiltonian matrix that has to be diagonalized effectively doubles in size. Certain magnetic systems involving non-collinear structures even require orbital functional such as the exact exchange for an appropriate description with density functional theory [267]. Consequently, most of the DFT studies addressing magnetic problems have been restricted to collinear magnetism. We will also first focus on surface magnetism phenomena that can be treated within the collinear formalism, but we will also discuss systems such as frustrated triangular spin structures that require a non-collinear treatment.

It is important to realize that the spin-polarized formalism just introduced is not only relevant for the treatment of magnetism in solids and at surfaces but it is also necessary for an appropriate description of atoms and solids with a non-vanishing magnetic moment, such as the hydrogen atom or the oxygen atom and molecule.

6.3 Two-dimensional Ferro- and Antiferromagnetism

For three-dimensional transition metal bulk systems, spontaneous magnetism is limited to the $3d$ metals, in particular metals and compounds including Fe, Co and Ni. The outer d electrons become less localized when moving from $3d$ to $4d$ and $5d$ metals. Consequently, because of the larger overlap between the d electrons, the d band becomes broader and the density of states at the Fermi energy becomes smaller. At the same time, also the exchange interaction decreases so that the Stoner parameter I becomes smaller. Therefore the Stoner criterion (6.18) is no longer satisfied for $4d$ and $5d$ metals.

However, in a two dimensional layer of transition metal atoms, the coordination of the atoms is lower, and consequently the width of the d band is smaller. In addition, there are band structure effects which can also stabilize magnetic phases. Such two-dimensional systems can be approximately realized by transition metal overlayers grown on noble metal substrates because of the relatively small interaction between the overlayer and the noble metal substrate. Interestingly, according to the Mermin-Wagner theorem [268], at finite temperatures there can be neither a ferromagnetic nor an antiferromagnetic order in one- or two-dimensional isotropic Heisenberg spin models (6.11) with short-range interactions ($\sum_j J_{ij} r_{ij}^2 < \infty$). However, in thin films deposited on substrates the spin interaction is usually not isotropic since the

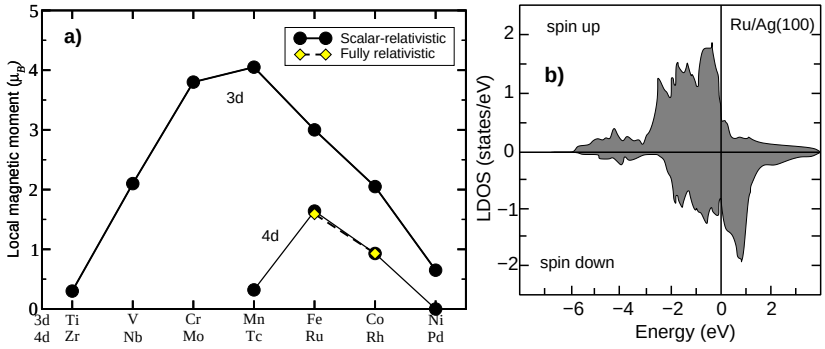

Fig. 6.2. a) Local magnetic moments calculated for 3*d* and 4*d* monolayers on Ag(100) from scalar-relativistic LSDA calculations, i.e. without spin-orbit coupling [270] and from fully relativistic LSDA calculations [271]; b) Local density of states of a Ru overlayer on Ag(100) (after [270]).

surface breaks the symmetry perpendicular to the film. One can show that this magnetic anisotropy stabilizes the long-range order in thin films [269].

Using an scalar-relativistic LSDA approach, the magnetism of transition metal overlayers on the (100) surfaces of Au and Ag has been investigated [270]. The local magnetic moments obtained from these calculations are plotted in Fig. 6.2a. And indeed, according to these calculations, monolayers of the 4*d* metals Tc, Ru and Rh are ferromagnetic although the corresponding bulk materials are non-magnetic. Obviously, band structure effects induced by the lower coordination stabilize the overlayer magnetism for the late 4*d* transition metals.

In Fig. 6.2a, additional results for Ru and Rh from fully relativistic calculations are included [271] which also take the spin-orbit coupling into account. As can be seen, for the 4*d* metals, the spin-orbit coupling hardly has an influence on the magnetic moments. However, the inclusion of this coupling does in fact matter for the 5*d* metals, where scalar-relativistic calculations predict the Os/Ag(100) and Ir/Ag(100) overlayers to be ferromagnetic [270] while the ferromagnetism vanishes when the spin-orbit coupling is taken into account [271].

In addition, Fig. 6.2b displays the local density of states of the Ru overlayer on Ag(100). The majority band, i.e., the band with the larger degree of filling, is about 1 eV lower in energy than the minority band which means that there is an exchange splitting between the spin up and the spin down states of roughly 1 eV. For the 3*d* metals on Ag(100), however, the exchange splitting is much larger, for example, it amounts to about 3 eV for Fe. There are also subtle effects due to the coupling to the substrate. While the Tc overlayer on Ag(100) still exhibits a weak ferromagnetism, on Au(100) this overlayer is non-magnetic because of the stronger interaction with Au *d* states which are higher in energy than the Ag *d* states.

It should be emphasized that the results presented in Fig. 6.2 corresponded to real predictions when they were made because the magnetic moments of these overlayer systems were not measured yet when the calculations were done. In fact, most of these predictions still await an experimental verification.

So far we have just discussed the ferromagnetic state of the metallic monolayers. Depending on the exchange coupling, there might as well be antiferromagnetic solutions. Within a Heisenberg model for a square lattice, as given by the (100) surface, the situation is simple if nearest-neighbor interactions J_1 are dominating: For $J_1 > 0$, the monolayers are ferromagnetic, while for $J_1 < 0$ a $c(2 \times 2)$ antiferromagnetic structure is stable.

DFT calculations indeed suggest that V, Cr, and Mn monolayers on several (100) surfaces of late d transition and noble metals exhibit a $c(2 \times 2)$ antiferromagnetic configuration whereas Fe, Co, and Ni prefer a $p(1 \times 1)$ ferromagnetism. The $c(2 \times 2)$ antiferromagnetic phase was first predicted by theory; later experimental observations of a Mn overlayer on W(110) using a spin-polarized STM were interpreted to be an indication for the existence of this phase [272]. These experiments have then motivated further calculations based on DFT [273, 274] which will be discussed in the following.

Tungsten has an interatomic distance in the bulk that is 7% larger than the one of manganese. Hence the pseudomorphic Mn films on W(110) are significantly strained. Still, experimentally it has been observed that up to four monolayers of Mn can grow pseudomorphically on W(110) [273]. The DFT calculations confirm that the adsorption of Mn on W(110) is associated with a large energy gain of 1.79 eV/atom for a Mn monolayer in the most favorable magnetic configuration [274]. Still it should be noted that this energy is considerably smaller than the bulk cohesive energy of Mn, 2.92 eV [12], which means that the Mn films on W(110) are not thermodynamically stable against the formation of Mn droplets.

The different magnetic structures of the Mn/W(110) film considered in two different GGA-DFT calculations using a FP-LAPW [273] and a plane-wave approach [274] are illustrated in Fig. 6.3. For one Mn monolayer, the antiferromagnetic $c(2 \times 2)$ structure (Fig. 6.3b) where all nearest-neighbor atoms couple antiferromagnetically is the most stable, followed by the antiferromagnetic $p(2\times1)$ structure (Fig. 6.3c), where two nearest-neighbor atoms couple antiferromagnetically and two other couple ferromagnetically, and the ferromagnetic configuration (Fig. 6.3a). While both DFT methods [273, 274] agree qualitatively on the energetic ordering of the structures, there are some quantitative differences. According to the FP-LAPW calculations [273], the $p(2 \times 1)$ AF and the FM structures are 102 and 188 meV/atom higher in energy than the $c(2 \times 2)$ AF configuration, respectively, whereas the corresponding plane-wave values [274] are 151 and 186 meV/atom.

In spite of the relatively strong Mn-W interaction, the Mn atoms in the two-dimensional film on W(110) exhibit a larger magnetic moment

7. Gas-Surface Dynamics

In the preceding chapter we have been concerned with the solution of the electronic Schrödinger equation for fixed nuclear coordinates. By performing total-energy calculations for many different nuclear configurations, energy minima and whole potential energy surfaces for chemical reactions at surfaces can be determined. However, this static information is often not sufficient to really understand how a reaction proceeds. Furthermore, in the experiment the potential energy surface (PES) is never directly measured but just reaction rates and probabilities. For a real understanding of a reaction mechanism a dynamical simulation has to be performed. This also allows a true comparison between theory and experiment and thus provides a reliable check of the accuracy of the calculated PES on which the dynamics simulation is based.

In this chapter methods to perform dynamical simulations will be introduced. In principle the atomic motion should be described by a quantum mechanical treatment, but often classical mechanics is sufficient. I will therefore first present classical methods and then review quantum mechanical methods.

7.1 Classical Dynamics

One can perform classical molecular dynamics studies by integrating the classical equations of motion, either Newton's equation of motion

$$M_i \, \frac{\partial^2}{\partial t^2} \boldsymbol{R}_i = -\frac{\partial}{\partial \boldsymbol{R}_i} V(\{\boldsymbol{R}_j\}) \,, \tag{7.1}$$

or Hamilton's equation of motion

$$\dot{q} = \frac{\partial H}{\partial p} \quad \dot{p} = -\frac{\partial H}{\partial q} \,. \tag{7.2}$$

The solution of the equations of motion can be obtained by standard numerical integration schemes like Runge–Kutta, Bulirsch–Stoer or predictor-corrector methods (see, e.g., [17]). Very often the rather simple Verlet algorithm [290,291] is used which is easily derived from a Taylor expansion of the trajectory.

$$\begin{aligned}\boldsymbol{r}_i(t+h) &= \boldsymbol{r}_i(t) + h\,\left.\frac{d\boldsymbol{r}_i}{dt}\right|_{h=0} + \frac{h^2}{2}\left.\frac{d^2\boldsymbol{r}_i}{dt^2}\right|_{h=0} + \frac{h^3}{6}\left.\frac{d^3\boldsymbol{r}_i}{dt^3}\right|_{h=0} + \ldots \\ &= \boldsymbol{r}_i(t) + h\,\boldsymbol{v}_i(t) \;+\; \frac{h^2}{2}\,\frac{\boldsymbol{F}_i(t)}{m} \;+\; \frac{h^3}{6}\left.\frac{d^3\boldsymbol{r}_i}{dt^3}\right|_{h=0} + \ldots \qquad (7.3)\end{aligned}$$

Here we have introduced the velocity $\boldsymbol{v}_i = d\boldsymbol{r}_i/dt$. Furthermore, we have used Newton's equation of motion to include the force $\boldsymbol{F}_i = md^2\boldsymbol{r}_i/dt^2$ acting on the i-th particle. Analogously we can derive

$$\boldsymbol{r}_i(t-h) = \boldsymbol{r}_i(t) - h\,\boldsymbol{v}_i(t) \;+\; \frac{h^2}{2}\,\frac{\boldsymbol{F}_i(t)}{m} \;-\; \frac{h^3}{6}\left.\frac{d^3\boldsymbol{r}_i}{dt^3}\right|_{h=0} + \ldots \qquad (7.4)$$

Adding (7.3) and (7.4) yields the Verlet algorithm [290]

$$\boldsymbol{r}_i(t+h) = 2\boldsymbol{r}_i(t) \;-\; \boldsymbol{r}_i(t-h) \;+\; h^2\,\frac{\boldsymbol{F}_i(t)}{m} \;+\; O(h^4)\,. \qquad (7.5)$$

There is a simple test whether the numerical integration of the equations of motion is accurate and reliable: the total energy, i.e., the sum of the kinetic energy and potential energy, should be conserved along the trajectory. In order to evaluate the kinetic energies, the velocities at time t are needed. Note that they do not explicitly appear in (7.5). They can be estimated by

$$\boldsymbol{v}_i(t) = \frac{\boldsymbol{r}_i(t+h) - \boldsymbol{r}_i(t-h)}{2h}\,. \qquad (7.6)$$

However, the kinetic energy evaluated with (7.6) belongs to the time step prior to the one used for the positions (7.5) which enter the evaluation of the potential energy. This problem can be avoided in the so-called *velocity* Verlet algorithm [291]

$$\begin{aligned}\boldsymbol{r}_i(t+h) &= \boldsymbol{r}_i(t) \;+\; h\,\boldsymbol{v}_i(t) \;+\; \frac{h^2}{2}\,\frac{\boldsymbol{F}_i(t)}{m} \\ \boldsymbol{v}_i(t+h) &= \boldsymbol{v}_i(t) \;+\; h\,\frac{\boldsymbol{F}_i(t+h) + \boldsymbol{F}_i(t)}{2m}\,, \qquad (7.7)\end{aligned}$$

which is mathematically equivalent to the Verlet algorithm (Problem 7.1).

In order to perform molecular dynamics simulations with the Verlet algorithm, a specific time step has to be chosen. Of course, the error associated with each time step is the smaller, the shorter the time step. On the other hand, a shorter time steps means more iterations for a given trajectory or simulation time which increases the computational cost. Furthermore, the error of each time step may accumulate. Hence the chosen time step will represent a compromise. The change in the total energy during one molecular run should be well below 1%. As a rule of the thumb, the time step should be ten times smaller than the shortest vibrational or rotational period of a given system. If, e.g., hydrogen belongs to the simulation ensemble, then usually the H-H intramolecular vibration corresponds to the fastest time scale with a vibrational period of $\tau_{\mathrm{vib}} \approx 8\,\mathrm{fs}$, hence the time step should be shorter than 0.8 fs.

In a conservative system, the energy is conserved in a molecular dynamics run. In a thermodynamical sense this means that the phase space trajectory belongs to the microcanonical ensemble. Often it is desirable to include dissipation effects in the gas-surface dynamics simulations. The simplest way to achieve this is to add a friction term to the Hamiltonian. If, however, the substrate should not only act as an energy sink but rather as a heat bath in order to model thermalization and accommodation processes, both energy loss and energy gain processes have to be taken into account. This can be achieved by a number of techniques. The most prominent ones are the *generalized Langevin equation* approach [292] and the *Nosé thermostat* [293, 294]. In both approaches, the molecular dynamics simulations sample the canonical ensemble at a specified temperature.

7.2 Quantum Dynamics

There are two ways to determine quantum mechanical reaction probabilities: by solving the time-dependent or the time-independent Schrödinger equation. Both approaches are equivalent [295] and should give the same results. The question which method is more appropriate depends on the particular problem. Time-independent implementations are usually more restrictive as far as the form of the potential is concerned, but often the choice of the method is a matter of training and personal taste.

In the most common time-independent formulation, the concept of defining one specific reaction path coordinate is crucial. Starting from the time-independent Schrödinger equation

$$(H - E)\ \Psi = 0\,, \tag{7.8}$$

one chooses one specific reaction path coordinate s and separates the kinetic energy operator in this coordinate

$$(\frac{-\hbar^2}{2\mu}\partial_s^2 + \tilde{H}E)\ \Psi = 0\,. \tag{7.9}$$

Here $\tilde{H}$ is the original Hamiltonian except for the kinetic energy operator in the reaction path coordinate. Usually the use of curvelinear reaction path coordinates results in a more complicated expression for the kinetic energy operator involving cross terms, but for the sake of clarity I have neglected this in (7.9). As the next step one expands the wave function in the coordinates perpendicular to the reaction path coordinate in some suitable set of basis functions,

$$\Psi = \Psi(s, \ldots) = \sum_n\ \psi_n(s)\ |n\rangle\,. \tag{7.10}$$

Here n is a multi-index, and the expansion coefficients $\psi_n(s)$ are assumed to be a function of the reaction path coordinate. Now we insert the expansion of

Ψ in (7.9) and multiply the Schrödinger equation by $\langle m|$, which corresponds to performing a multi-dimensional integral. Since the basis functions $|n\rangle$ are assumed to be independent of s, we end up with the so-called coupled-channel equations,

$$\sum_n \left\{ \left(\frac{-\hbar^2}{2\mu}\partial_s^2 - E\right) \delta_{m,n} + \langle m|\tilde{H}|n\rangle \right\} \psi_n(s) = 0\,. \tag{7.11}$$

Instead of a partial differential equation – the original time-independent Schrödinger equation (7.8) – we now have a set of coupled ordinary differential equation. Still a straightforward numerical integration of the coupled-channel equations leads to instabilities, except for in simple cases, due to exponentially increasing so-called closed channels. These problems can be avoided in a very stable and efficient coupled-channel algorithm [296–298] that will be briefly sketched in the following.

For the solution Ψ defined in (7.10), which represents a vector in the space of the basis functions, the initial conditions are not specified. This function can also be considered as a matrix

$$\Psi = (\psi)_{nl}\,, \tag{7.12}$$

where the index l labels a solution of the Schrödinger equation with an incident plane wave of amplitude one in channel l and zero in all other channels. Formally one can then write the solution of the Schrödinger equation for a scattering problem in a matrix notation as

$$\begin{aligned} \Psi(s \to +\infty) &= \mathrm{e}^{-iqs} \;-\; \mathrm{e}^{iqs}\; r\,, \\ \Psi(s \to -\infty) &= \mathrm{e}^{-iqs}\; t\,. \end{aligned} \tag{7.13}$$

Here $q = q_m\delta_{m,n}$ is a diagonal matrix, r and t are the reflection and transmission matrix, respectively. Now one makes the following ansatz for the wave function,

$$\Psi(s) = (1 - \rho(s))\;\frac{1}{\tau(s)}\;t\,. \tag{7.14}$$

Equation (7.14) defines the *local reflection matrix* $\rho(s)$ ($LORE$) and the *inverse local transmission matrix* $\tau(s)$ ($INTRA$). The boundary values for these matrices are (except for phase factors which, however, do not affect the transition probabilities):

$$(\rho(s);\tau(s)) \;=\; \begin{cases} (r;t) & s \to +\infty \\ (0;1) & s \to -\infty \end{cases}\,. \tag{7.15}$$

From the Schrödinger equation first order differential equations for both matrices can be derived [296] which can be solved by starting from the known initial values at $s \to -\infty$; at $s \to +\infty$ one then obtains the physical reflection and transmission matrices. Thus the numerically unstable boundary value problem has been transformed into a stable initial value problem.

In the time-dependent or wave-packet formulation, the solution of the time-dependent Schrödinger equation

$$i\hbar \, \frac{\partial}{\partial t} \, \Psi(\boldsymbol{R}, t) = H \, \Psi(\boldsymbol{R}, t) \tag{7.16}$$

can formally be written as

$$\Psi(\boldsymbol{R}, t) = e^{-iHt/\hbar} \, \Psi(\boldsymbol{R}, t = 0) \, . \tag{7.17}$$

Here where we have used the time evolution operator $\exp(-iHt/\hbar)$ with the Hamiltonian $H = T + V$ for time-independent potentials V. The evaluation of the time evolution operator is unfortunately not straightforward because the kinetic energy operator T and the potential V do in general not commute. The most common methods to represent the time-evolution operator $\exp(-iHt/\hbar)$ in the gas-surface dynamics community are the split-operator [299, 300] and the Chebychev [301] methods. In the split-operator method, the time-evolution operator for small time steps Δt is written as

$$\mathrm{e}^{-\mathrm{i}H\Delta t/\hbar} = \mathrm{e}^{-\mathrm{i}T\Delta t/2\hbar} \, \mathrm{e}^{-\mathrm{i}V\Delta t/\hbar} \, \mathrm{e}^{-\mathrm{i}T\Delta t/2\hbar} \; + \; O(\Delta t^3) \, , \tag{7.18}$$

Interestingly enough, the split-operator technique for a certain number of time steps corresponds to a naive successive application of the operator $\exp(-iT\Delta t/\hbar)$ and $\exp(-iV\Delta t/\hbar)$ except for the first and last step. However, apparently this is sufficient to approximately take into account the fact that T and V do not commute.

In the Chebyshev method, the time-evolution operator is expanded as

$$e^{-iH\Delta t/\hbar} = \sum_{j=1}^{j_{\max}} \, a_j(\Delta t) \, T_j(\bar{H}) \, , \tag{7.19}$$

where the T_j are Chebyshev polynomials and $\bar{H}$ is the Hamiltonian rescaled to have eigenvalues in the range $(-1, 1)$. Both propagation schemes use the fact that the kinetic energy operator is diagonal in $\boldsymbol{k}$-space and the potential is diagonal in real-space. The wave function and the potential are represented on a numerical grid, and the switching between the $\boldsymbol{k}$-space and real-space representations is efficiently done by Fast Fourier Transformations (FFT) [17].

Quantum dynamical studies are still computationally very demanding. This prevents the explicit dynamical consideration of surface degrees of freedom. At most, one surface oscillator has been taken into account to model the influence of the substrate vibrations on scattering or adsorption probabilities [302–304]. However, usually one is not interested in the explicit dynamics of the substrate vibrations in the context of gas-surface dynamics as long as there is no strong surface rearrangement due to the interaction with atoms and molecules. In such a case, substrate phonons are then rather treated as a heat bath that lead to thermalization and dissipation effects. In order to describe these effects in terms of an open system dynamics, the system can

be partitioned into a subsystem (often referred to as just *the system*) and the surrounding bath. The *reduced density matrix*

$$\rho = \sum_{m,n} w_{mn} \, |m\rangle\langle n| \, , \tag{7.20}$$

is then defined in the Hilbert space of the system Hamiltonian H. If the functions $|n\rangle$ form a basis of this space, the diagonal matrix elements $w_{nn} = \langle n|\rho|n\rangle$ are interpreted as the population of the state $|n\rangle$, whereas the off-diagonal elements $w_{mn} = \langle m|\rho|n\rangle$ are related to the phase coherence between the states $|m\rangle$ and $|n\rangle$ with respect to interference effects [305]. Physical observables are obtained as usual in a density matrix formulation by forming the trace

$$\langle A \rangle = \mathrm{tr}\,(A\rho) \; . \tag{7.21}$$

The time-evolution of the reduced density matrix is given by the *Liouville–von Neumann equation* [305, 306]

$$\frac{\partial \rho}{\partial t} = -\frac{\mathrm{i}}{\hbar} \, [H, \rho] + \mathcal{L}_B \rho \, , \tag{7.22}$$

where dissipation effects are taken into account through the Liouville bath operator $\mathcal{L}_B$. Without the dissipation term, (7.22) is equivalent to the time-dependent Schrödinger equation. However, solving (7.22) for a closed system is not advisable, since a $N \times N$ matrix has to be determined if the wave functions are expanded in a set of N basis functions while in the ordinary time-dependent Schrödinger equation the wave function is just represented by a N-dimensional vector. Still, the computational effort associated with the density-matrix formalism is necessary in order to include dissipation effects in the quantum dynamics. This is not only essential for scattering and reactive processes at surface, but also for reactions induced by electronic transitions (see Sect. 9.5). The dissipative term can describe vibrational or electronic relaxation effects as well as so-called dephasing processes with corresponding time scales, T_1, T_2 and T_2^*, respectively.

There is no unique way to choose the bath operator $\mathcal{L}_B$. Usually one invokes the *Markov approximation*, which means that one assumes that the change of the density matrix at time t is a function of the reduced density matrix at that time only, i.e. there are no memory effects of the past history. Even in this approximation, $\mathcal{L}_B$ is not fully specified. There is a phenomenological form proposed by Lindblad [307] which guarantees that at all times the diagonal elements of ρ properly correspond to state populations. The Lindblad semigroup functional is given by

$$\mathcal{L}_B \rho = \sum_k \left(C_k \rho C_k^+ - \left\{ C_k^+ C_k, \rho \right\} \right) \, , \tag{7.23}$$

where $\{A, B\} = AB + BA$ denotes the anticommutator. The C_k are the Lindblad operators. The dissipative channel is labeled by the subscript k. In the

Lindblad approach, different diagonal elements are coupled by energy relaxation processes on a timescale T_1. The off-diagonal elements decay because of energy relaxation on the timescale $T_2 = 2T_1$ as well as because of pure dephasing processes due to elastic processes on a time scale T_2^*. A shortcoming of the Lindblad approach is that the operators are not connected in a physically transparent way to the interaction Hamiltonian between system and bath [305].

In the Redfield approach [308], the bath operator $\mathcal{L}_B$ is derived from the system-bath interaction using second-order perturbation theory. This leads to the Redfield equations

$$\mathcal{L}_B \rho = \sum_l \left(\left[G_l^+ \rho, G_l \right] + \left[G_l, \rho G_l^- \right] \right) , \tag{7.24}$$

where the bath modes are labeled by l and the system dependence of the system-bath operators is represented by the operators G_l. Still, the Redfield approach suffers from another deficiency, namely the possible violation of the positivity of the density matrix. There have been further proposals for the construction of $\mathcal{L}_B$ [305] which will not be discussed here.

Often negative imaginary potentials, so-called *optical potentials* have been used in dissipative dynamics. However, it is important to realize that there is a difference between the use of a friction term in classical dynamics and the use of an optical potential in quantum dynamics. Whereas a friction term leads to momentum relaxation processes, an optical potential reduces the norm of the wave function.

It is a wide-spread believe that classical dynamical methods are much less time-consuming than quantum ones. This is certainly true if one compares the computational cost of one trajectory to a quantum calculation. If integrated quantities such as the sticking probability are to be determined, then the statistical error of the result is only related to the number of computed trajectories and not to the dimensionality of the problem. For example, if the sticking probability S lies in the range $0.1 \leq S \leq 1$, then usually 10^3–10^4 trajectories are sufficient to obtain a sufficiently accurate result independent of the complexity of the system.

However, for the evaluation of detailed microscopic distribution function in scattering or desorption processes at surfaces the statistical requirements are much more demanding. Then the delocalized nature of the wave functions in the quantum dynamics can be advantageous. Instead of many trajectory calculations one quantum calculation might be sufficient. Quantum calculations correspond in a sense to the simultaneous determination of many trajectories. The crucial difference between quantum and classical dynamics is that in quantum dynamics the averaging is done coherently while it is done incoherently in classical dynamics. In addition, in wave-packet calculations dynamical simulations are performed for a whole range of energies in one run, and in a time-independent coupled-channel method the microscopic transitions probabilities of all open channels are determined simultaneously.

Consequently, quantum dynamical simulations do not necessarily have to be more time-consuming that classical calculations.

7.3 Parameterization of ab initio Potentials

In order to perform dynamical simulations on a potential energy surface derived from first-principles calculations, one needs a continuous description of the potential. This is especially true for quantum dynamical simulations. Since the wave functions are delocalized, they always probe a certain area of the PES at any time. The total energy calculations, however, just provide total energies for discrete configurations of the nuclei. In classical molecular dynamics simulation, the gradients of the potential are only needed for one particular configuration at any time. This makes ab initio molecular dynamics simulations possible in which the forces necessary to integrate the classical equations of motions are determined by electronic structure calculations in each step [309–312]. The evaluation of the forces for every time step of a MD run is computationally still so demanding that most ab initio molecular dynamics studies have been limited to the simulation of well below 100 trajectories. This number is usually much too small to obtain sufficient statistics for the reliable determination of reaction probabilities or distributions. However, this situation is changing. Recently the first ab initio molecular dynamics studies addressing dissociative adsorption on surface have been performed [313] that is based on more than 4.000 ab initio trajectories so that statistically meaningful results can be obtained, as will be demonstrated at the end of this chapter in Sect. 7.7.

On the other hand, molecular dynamics simulations on a suitable analytic representation of a potential energy surface can be extremely fast. Hence it is desirable to adjust the first-principles energies to an analytical or numerical continuous representation of the PES. This is a highly non-trivial task. On the one hand the representation should be flexible enough to accurately reproduce the ab initio input data, on the other hand it should have a limited number of parameters so that it is still controllable. Ideally a good parameterization should not only accurately interpolate between the actually calculated points, but it should also give a reliable extrapolation to regions of the potential energy surface that have actually not been determined by the ab initio calculations.

The explicit form of the chosen analytical or numerical representation of the ab initio potential varies from application to application. Often the choice is dictated by the dynamics algorithm in which the representation is used. Most applications have been devoted to the interaction of a diatomic molecule with the surface [314, 315]. The angular orientation of the molecule has usually been expanded in spherical harmonics and the center-of-mass coordinates parallel to the surface in a Fourier series [316–319]. For the PES in the plane of the molecular distance from the surface and the interatomic separation a

representation in reaction path coordinate has been employed [317–320], but also two-body potentials have been used [316]. Before detailed ab initio potentials became available, the so-called LEPS (London-Eyring-Polanyi-Sato) form was often used to construct a global PES [321]. This parameterization contains only a small number of adjustable parameters which made it so attractive for model calculations, but which makes it at the same time relatively inflexible. A modified LEPS potential has still been successfully used to fit an ab initio PES of the interaction of atomic hydrogen with the hydrogenated Si(100) surface [322].

Ab initio total energies are often mainly determined at high-symmetry points of the surface in order to reduce the computational cost. It is true that these high-symmetry points usually reflect the extrema in the PES. However, due to this limitation the fitted continuous PES can only contain terms that correspond to these high-symmetry situations. On the one hand this often saves computer time also in the quantum dynamics because certain additional selection rules are introduced which reduces the necessary basis set [316,317]. On the other hand, of course this represents an approximation since it introduces additional artificial symmetries into the simulations. The question, how serious the neglect of terms with lower symmetry is, remains open until these terms have been determined and included in actual dynamical calculations. In fact, the influence of these terms can be quite significant, as has been revealed in ab initio molecular dynamics simulations [313].

Most of the corrugation in molecule-surface potential energy surfaces can already be derived from the atom-surface interaction. This observation has been used in corrugation-reducing procedures [323,324]. The first step is the ab initio determination of the interaction of both the atomic and the molecular species with the surface. From the atomic data, a three-dimensional reference function is constructed which is subtracted from the molecular potential energy surface. The remaining function is much smoother than the original potential energy surface and therefore much easier to fit. In addition, the interpolated PES reflects the correct symmetry of the system. This method has been successfully used for a continuous representation of several gas-surface interaction systems including H_2/Pd(111) [323], H_2/Ni(111) [324], H_2/Pt(211) [325], or H_2/Cu(110) [326].

If more than just the molecular degrees of freedom should be considered in a parameterization of an ab initio PES, analytical forms become very complicated and cumbersome. As an alternative, the interpolation of ab initio points by a neural network has been proposed [327–329]. Neural networks can fit, in principle, any real-valued, continuous function to any desired accuracy. They require no assumptions of the functional form of the underlying problem. On the other hand, there is no physical insight that is used as an input in this parameterization. Hence the parameters of the neural network do not reflect any physical or chemical property.

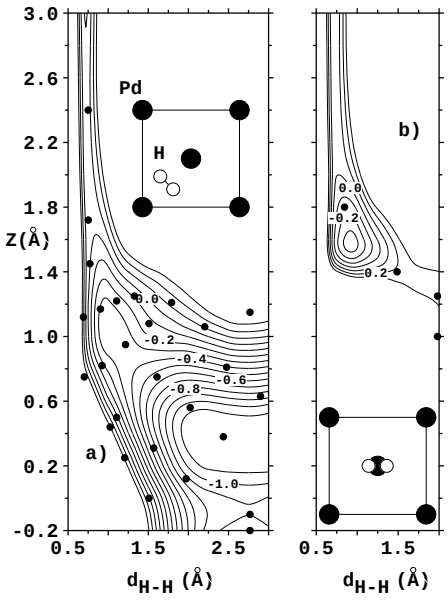

Fig. 7.1. Potential energy surface of H_2/Pd(100) evaluated by a tight-binding Hamiltonian that was adjusted to reproduce ab initio results of [202] (compare with Fig. 5.19). The filled circles indicate the points that have been used to obtain the fit. The insets demonstrate the lateral and angular configuration of the H_2 molecule. (After [330])

This deficiency is avoided if the results of first-principles electronic structure calculations are used to adjust the parameters of a tight-binding formalism [72]. A tight-binding method is more time-consuming than an analytical representation or a neural network since it requires the diagonalization of a matrix. However, due to the fact that the quantum mechanical nature of bonding is taken into account [68] tight-binding schemes need a smaller number of ab initio input points to perform a good interpolation *and* extrapolation [330]. This is demonstrated in Fig. 7.1 that shows the PES of H_2/Pd(100) obtained by a tight-binding fit to the ab initio data [202]. The plots should be compared with the ab initio PES in Fig. 5.19. The filled circles denote the points that have been used to obtain the fit. While for the h–b–h cut (see p. 137) a relatively large number of input points were necessary for the fit (Fig. 7.1a), for the h–t–h three points were sufficient for a satisfactory agreement with the ab initio data (Fig. 7.1a). This is caused by the fact that the parameters of the tight-binding scheme, the Slater-Koster integrals [67], have a well-defined physical meaning.

An important issue is to judge the quality of the fit to an ab initio PES. Usually the root mean squared (RMS) error between fit and input data is used as a measure of the quality of a fit. If this error is zero, then everything is fine. However, normally this error is larger than zero. The systematic error of the ab initio energies is usually estimated to be of the order of 0.1 eV. Often it is said that the RMS error of the fit should be of the same order. But the dynamics of molecular dissociation at surfaces can be dramatically different depending on whether there is a barrier for dissociation of height

0.1 eV or not [331]. Hence for certain regions of the PES the error has to be much less than 0.1 eV, while for other regions even an error of 0.5 eV might not influence the dynamics significantly. Another example occurs in a reaction path parameterization. If the curvature in the parameterization is off by a few percent, the energetic distribution of barrier heights is not changed and the dynamical properties are usually not altered significantly. However, the location of the barriers is changed and consequently the RMS error can become rather large. Hence one has to be cautious by just using the RMS error as a quality check of the fit. Unfortunately there is no other simple error function for the assessment of the quality of a fit. If it is possible, one should perform a dynamical check. Obviously, if the dynamical properties calculated on a fitted PES agree with the ones calculated on the original PES, the quality of the fit should be sufficient.

7.4 Scattering at Surfaces

If a beam of atoms or molecules is hitting a surface that has a small adsorption well for the particular particles, most of them will be scattered back into the gas phase. Especially for the case of light atoms and molecules when the de Broglie wave length of the particles is of the order of the lattice spacing, the quantum nature of the scattering event has to be taken into account which leads to elastic scattering and diffraction.

Let us first consider a beam of atoms with initial wave vector $\boldsymbol{K}_i$ that is scattered elastically at a periodic surface. The component of the wave vector parallel to the surface $\boldsymbol{K}_f^{\parallel}$ after the scattering is given by

$$\boldsymbol{K}_f^{\parallel} = \boldsymbol{K}_i^{\parallel} + \boldsymbol{G}_{mn}\,, \tag{7.25}$$

where $\boldsymbol{G}_{mn}$ is a vector of the two-dimensional reciprocal lattice of the periodic surface. Since there is no energy transfer to the surface in elastic scattering, the total kinetic energy of the atoms is conserved:

$$\frac{\hbar^2 \boldsymbol{K}_f^2}{2M} = \frac{\hbar^2 \boldsymbol{K}_i^2}{2M}\,. \tag{7.26}$$

By (7.25) and (7.26) all possible final scattering angles are specified. This leads to a discrete, finite set of scattering channels. Note that for a given incident energy, angle and mass of the atoms the scattering angles are entirely determined by the geometry of the surface. The interaction potentials only influences the intensity of the scattering peaks, but not their position. That is why diffraction at surfaces can be used to determine the structure of surfaces.

Now we allow for energy transfer processes to the surface, i.e., we consider the inelastic scattering of atoms. The main source for inelastic effects is the excitation and deexcitation of substrate phonons. These phonons also carry momentum so that the conservation of parallel momentum leads to

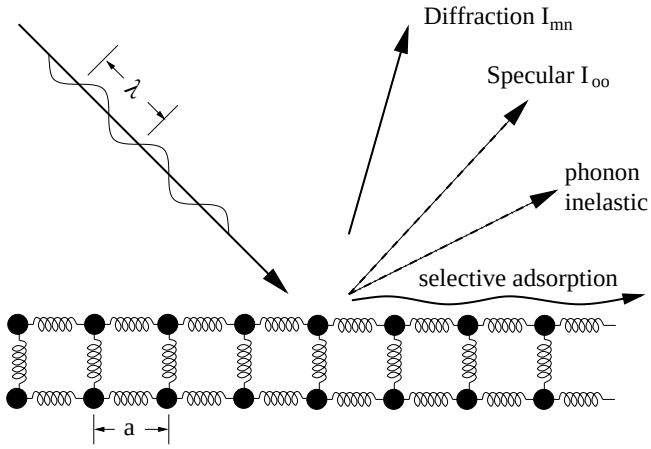

Fig. 7.2. Summary of the different collision processes in nonreactive scattering (after [332]).

$$\boldsymbol{K}_f^{\parallel} = \boldsymbol{K}_i^{\parallel} + \boldsymbol{G}_{mn} + \sum_{\text{exch.phon.}} \pm \boldsymbol{Q}\,, \tag{7.27}$$

where $\boldsymbol{Q}$ is a two-dimensional phonon-momentum vector parallel to the surface. The plus-signs in the sum correspond to the excitation or emission of a phonon while the minus-signs represent the deexcitation or absorption of a phonon. The excitation and deexcitation of phonons with momentum $\boldsymbol{Q}$ and mode index j also modifies the energy conservation relation:

$$\frac{\hbar^2 \boldsymbol{K}_f^2}{2M} = \frac{\hbar^2 \boldsymbol{K}_i^2}{2M} + \sum_{\text{exch.phon.}} \pm \hbar\omega_{\boldsymbol{Q},j}\,. \tag{7.28}$$

If only one phonon is emitted or absorbed in the collision process, the sums in (7.27) and (7.28) reduce to one term. If one-phonon processes are dominant in scattering, the phonon spectrum of a surface can be measured.

A schematic summary of possible collision processes in nonreactive scattering is presented in Fig. 7.2. With I_{mn} the intensity of the elastic diffraction peak mn according to (7.25) is denoted. The scattering peak I_{00} with $\boldsymbol{K}_f^{\parallel} = \boldsymbol{K}_i^{\parallel}$ is called the *specular peak*. The excitation of phonons usually leads to a reduced normal component of the kinetic energy of the back-scattered atoms or molecules. Thus the reflected beam is shifted in general to larger angles with respect to the surface normal compared to the angle of incidence. The resulting supraspecular scattering is indicated in Fig. 7.2 as the phonon-inelastic reflection event.

The coherent scattering of atoms or molecules from surfaces has been known as a tool for probing surface structures since 1930 [333]. The diffraction pattern yields direct information about the periodicity and lattice constants of the surface. Furthermore, if one measures the intensity of the specular

peak as a function of the angle of incidence, then at specific angles resonances appear [334]. They are due to so-called *selective adsorption resonances* which are also indicated in Fig. 7.2. These resonances occur when the scattered particle can make a transition into one of the discrete bound states of the adsorption potential. This can only happen if temporarily the motion of the particle is entirely parallel to the surface. The interference of different possible paths along the surface causes the resonance effects. Energy and momentum conservation yields the selective adsorption condition

$$\frac{\hbar^2 \boldsymbol{K}_i^2}{2M} = \frac{\hbar^2 (\boldsymbol{K}_i^{\parallel} + \boldsymbol{G}_{mn})^2}{2M} - |E_l| \,, \tag{7.29}$$

where E_l is a bound level of the adsorption potential. Usually these selective adsorption resonances only occur for relative weak adsorption potentials that are not strongly corrugated, i.e., mainly for physisorption potentials. The bound state energies can be obtained without detailed knowledge of the scattering process. Typically one assumes a Morse potential

$$V(z) = D_0 \, \left(\mathrm{e}^{-2\alpha(z-z_o)} - 2\mathrm{e}^{-\alpha(z-z_o)} \right) \,, \tag{7.30}$$

or some other parameterization of the interaction potential and can then derive the well depth, position and range of the adsorption potential from an adjustment of the parameters of the potential to reproduce the experimentally observed binding energies [109]. In particular helium atom scattering (HAS) has been used intensively to study surface crystallography and the shape of physisorption potentials (see, e.g., [335] and references therein). Helium atom scattering has furthermore been employed extensively in order to determine the surface phonon spectrum in one-phonon collisions via (7.27) and (7.28) [335].

Hydrogen molecules have been utilized less frequently in order to study interaction potentials [336]. The coherent elastic scattering of molecules is more complex than atom scattering because in addition to parallel momentum transfer the internal degrees of freedom of the molecule, rotations and vibrations, can be excited during the collision process. Then the total energy balance in the scattering reads

$$\frac{\hbar^2 \boldsymbol{K}_f^2}{2M} = \frac{\hbar^2 \boldsymbol{K}_i^2}{2M} + \Delta E_{\mathrm{rot}} \; + \; \Delta E_{\mathrm{vib}} + \sum_{\mathrm{exch.phon.}} \pm \hbar \omega_{\boldsymbol{Q},j} \,. \tag{7.31}$$

Usually the excitation of molecular vibrations in molecule-surface scattering is negligible, in contrast to the phonon excitation. This is due to the fact that the time-scale of the molecular vibrations is usually much shorter than the scattering time or the rotational period. Therefore the molecular vibrations follow the scattering process almost adiabatically. Molecular rotations, on the other hand, can be excited rather efficiently in the scattering at highly anisotropic surfaces. The rotational excitation leads to additional peaks in the diffraction spectrum, the *rotationally inelastic diffraction* peaks.

8. Kinetic Modeling of Processes on Surfaces

Many processes on surfaces such as diffusion, desorption etc. are hindered by large energetic barriers. On a microscopic time scale, these processes occur very rarely. Many unsuccessful attempts are performed before eventually the corresponding barrier is crossed. The time between two successful events can easily be in the order of nanoseconds or even longer. In any microscopic molecular dynamics simulation all unsuccessful events are explicitly included. Since the time scale of MD runs is typically limited to picoseconds, the simulation of these rare events is prohibited. Besides, such a simulation would mean a waste of computer time because a lot of useless information would be gathered.

Therefore, for the simulation of these processes a kinetic approach is necessary in which the single processes are described by the corresponding rates. Note that in the chemistry literature a rate usually has the dimension concentration per time. In contrast, here rates will simply be quantities with the dimension one over time which a chemist would call rate constants. In this chapter, we will first show how the rates can be determined from microscopic information via transition state theory. We will then show how processes such as diffusion and growth can be described either by rate equations or by kinetic Monte Carlo simulations. This allows to extend the information gained from microscopic electronic structure calculations to simulations on mesoscopic or even macroscopic time and length scales which will be illustrated in detail.

8.1 Determination of Rates

Experimentally it is well established that the rate of many processes as a function of temperature follows the Arrhenius behavior

$$k = k_0 \ \exp\left(-\frac{E_a}{k_\mathrm{B}T}\right) . \tag{8.1}$$

In (8.1), E_a is the apparent activation energy which is usually interpreted as the minimum barrier hindering the particular process. From a microscopic point of view, it is desirable to derive an expression for a rate from the properties of the underlying potential energy surface. This can in fact be done using transition state theory (TST) [439].

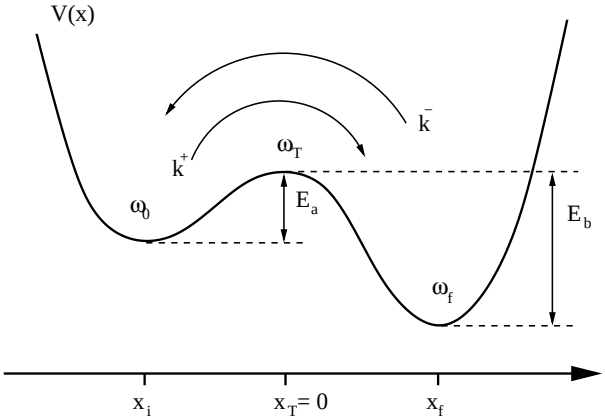

Fig. 8.1. Schematic representation of escape processes between to locally stable states with forward rate k^+ and backward rate k^-

Consider a potential $V(x)$ along the reaction path coordinate x connecting two locally stable states (Fig. 8.1). At $x = x_\mathrm{T} = 0$ the transition state is located. The barrier for the forward escape is given by E_a while the corresponding barrier for the backward process is E_b. In the following we are mainly concerned with the derivation of the forward rate k^+. The frequency of particles vibrating in the initial well around x_i is given by ω_0. The transition state is characterized by an imaginary frequency ω_T.

There are two basic assumptions underlying transition state theory. First, it is assumed that the moving particles are sufficiently strongly coupled to a heat bath so that there is local thermodynamic equilibrium along the whole reaction path. Secondly, the transition state corresponds to a point of no return which means that any trajectory passing through the transition state will not recross it. This last assumption is inherently coupled to classical mechanics because in quantum mechanics it does not make sense to speak of single trajectories with no recrossings. Hence transition-state theory is fundamentally a classical mechanical theory, although the concept can be generalized to consider the leading quantum corrections within semiclassical quantum theory [439].

Using the basic assumptions mentioned above, the equilibrium average of the one-way forward flux at the transition state can be expressed as

$$k^+_\mathrm{TST} = \frac{\langle\, \delta(x)\, \dot{x}\, \Theta(\dot{x})\, \rangle}{\langle \Theta(-x) \rangle}\,. \tag{8.2}$$

Here the average $\langle \ldots \rangle$ denotes the thermal expectation value. Θ is the step function defined by

$$\Theta(x) \;=\; \begin{cases} 1\,, & \text{for} \;\; x > 0 \\ 0\,, & \text{for} \;\; x < 0 \end{cases}\,. \tag{8.3}$$

Hence $\langle \Theta(-x) \rangle = \bar{n}_i$ corresponds to the equilibrium population for $x < 0$, i.e., of the initial state i in the left well of Fig. 8.1. It is important to note that the rate (8.2) always gives an upper bound for the true rate, i.e. $k^+_{\mathrm{TST}} \geq k$, since recrossing of reactive trajectories are neglected.

In order to derive the rate expression within TST, we start with the simple case of an one-dimensional system according to Fig. 8.1. A particle of mass m moves in the potential $V(x)$ with two local minima. Using (8.2), the transition-state forward rate from state i to state f is given by

$$k_{\mathrm{TST}} = Z_0^{-1} \, \frac{1}{2\pi\hbar} \int dq \; dp \; \delta(q) \; \dot{q} \; \theta(\dot{q}) \; \exp(-\beta H(q,p)) \,, \tag{8.4}$$

where we have identified the variable q with the reaction-path coordinate x. $\beta = 1/k_{\mathrm{B}}T$ is the inverse temperature and Z_0 denotes the partition sum in the initial well

$$Z_0 = \frac{1}{2\pi\hbar} \int\limits_{q<0} dq \; dp \; \exp(-\beta H(q,p)) \,. \tag{8.5}$$

The integral over the momentum coordinate p in (8.4) can easily be evaluated to yield

$$\begin{aligned} \int\limits_{-\infty}^{\infty} dp \; \dot{q} \; \theta(\dot{q}) \; \exp\left(-\beta \frac{p^2}{2m}\right) &= \int\limits_{0}^{\infty} dp \; \frac{p}{m} \; \exp\left(-\frac{p^2}{2mk_{\mathrm{B}}T}\right) \\ &= k_{\mathrm{B}}T \,, \end{aligned} \tag{8.6}$$

while the integral over the coordinate q simply gives

$$\int dq \; \delta(q) \; \exp\left(-\frac{V(q)}{k_{\mathrm{B}}T}\right) = \exp\left(-\frac{E_a}{k_{\mathrm{B}}T}\right) . \tag{8.7}$$

Inserting the expressions for the integrals into (8.4), we get for the reaction rate

$$k_{\mathrm{TST}} = \frac{k_{\mathrm{B}}T}{h} \; \frac{1}{Z_0} \; \exp\left(-\frac{E_a}{k_{\mathrm{B}}T}\right) . \tag{8.8}$$

In the harmonic approximation, the partition sum in the initial well is given by $Z_0 = k_{\mathrm{B}}T/\hbar\omega_0$, i.e., we obtain the following rate

$$k_{\mathrm{TST}} = \frac{\omega_0}{2\pi} \; \exp\left(-\frac{E_a}{k_{\mathrm{B}}T}\right) . \tag{8.9}$$

Here we already see that the prefactor before the exponential in (8.9) corresponds to an attempt frequency that yields the number of attempts that the particle tries to get over the barrier. The Boltzmann factor then gives the thermal probability that the particle has enough energy to cross the transition state.

This formalism can relatively easily be extended to the multi-dimensional case starting from the flux expression (8.2), in particular for the case of a

nonlinear coordinate ($i = 0$) coupled to N vibrational degrees of freedom. In the harmonic approximation, which is valid for $\hbar\omega \ll k_{\mathrm{B}}T$, the partition sums Z_0 and Z_{TS} in the initial well and at the transition state are simply given by

$$Z_0 \;=\; \prod_{i=0}^{N} \left\{ \frac{k_{\mathrm{B}}T}{\hbar\omega_i^{(0)}} \right\}, \quad Z_{\mathrm{TS}} \;=\; \prod_{i=1}^{N} \left\{ \frac{k_{\mathrm{B}}T}{\hbar\omega_i^{\mathrm{TS}}} \right\}, \tag{8.10}$$

where $\omega_i^{(0)}$ and ω_i^{TS} are the vibrational frequencies in the initial well and the transition state, respectively. We note in passing that often the transition state is denoted by $(\neq)$, i.e. $Z_{\mathrm{TS}} \equiv Z^{\neq}$. The transition rate can now be expressed as [439]

$$\begin{aligned} k_{\mathrm{TST}} &= \frac{k_{\mathrm{B}}T}{h}\, \frac{Z^{\mathrm{TS}}}{Z_0} \exp\left(-\frac{E_a}{k_{\mathrm{B}}T}\right) \\ &= \frac{1}{2\pi}\, \frac{\prod_{i=0}^{N} \omega_i^{(0)}}{\prod_{i=1}^{N} \omega_i^{\mathrm{TS}}}\, \exp\left(-\frac{E_a}{k_{\mathrm{B}}T}\right). \end{aligned} \tag{8.11}$$

This result for the TST rate can be reformulated employing the Helmholtz free energy F via the substitution

$$Z = \exp[-(E - TS)/(k_{\mathrm{B}}T)] = \exp[-F/(k_{\mathrm{B}}T)] \tag{8.12}$$

Inserting this expression into (8.11), we arrive at

$$k_{\mathrm{TST}} = \frac{k_{\mathrm{B}}T}{h}\, \exp\left(\frac{\Delta S}{k_{\mathrm{B}}}\right)\, \exp\left(-\frac{E_a}{k_{\mathrm{B}}T}\right) = k_0\, \exp\left(-\frac{E_a}{k_{\mathrm{B}}T}\right), \tag{8.13}$$

where $\Delta S = S_{\mathrm{TS}} - S_0$ is the entropy change and S_{TS} and S_0 are the entropy of the $2N$-dimensional phase space at the transition state and the $2(N+1)$-dimensional phase space in the initial well. Hence we have derived the Arrhenius expression (8.1) from transition state theory. Note that the prefactor k_0 which is usually assumed to be temperature-independent has in fact a linear dependence on the temperature according to (8.13). However, since the temperature dependence is dominated by the exponential term, it is still often justified to neglect the temperature dependence of the prefactor. Furthermore, as (8.11) shows, in the harmonic approximation the linear temperature dependence of the first factor is canceled by the temperature dependence of the entropy change.

In principle, all variables in (8.11) can be evaluated from electronic structure calculations since they are all related to the potential energy surface. However, usually the determination of eigenmode-frequencies is computationally very demanding since it involves the evaluation and diagonalization of a Hesse matrix. Hence often the prefactor in (8.11) is just estimated and only barrier heights are computed from first principles.

Furthermore, it is not trivial to locate the transition state. There is no uniquely defined way of finding the minimum energy path between a given initial and final state. One way to determine this path is to simply map out the relevant potential energy surface in great detail, but this can be computationally very demanding. However, there are robust methods that can be used to find a minimum energy path. In the *nudged elastic band method* [440,441], first the energy and the forces of the system are determined along a string usually interpolating linearly between initial and final state. Neighboring points along the string are connected by springs in order to guarantee a continuous path. Then an optimization algorithm is performed which involves force projections of both the true forces and the spring forces. Thus the string of points is dragged closer and closer to the minimum energy path until the transition state is located. In that way, also nonintuitive transition state geometries might be detected.

8.2 Diffusion

A single particle on a surface can jump laterally along the surface from one stable adsorption site to the next. This process is a typical process that is driven by thermal fluctuations. Each adsorbate performs thermal vibrations around the equilibrium site in the adsorption well. The rate for a jump to a next nearest neighbor site is then given by an Arrhenius expression

$$k_\mathrm{j} = k_0 \ \exp\left(-\frac{E_a}{k_\mathrm{B} T_s}\right) , \tag{8.14}$$

where E_a is the energetic barrier to the next-nearest neighbor site and T_s is the surface temperature. To obtain a more detailed understanding of the so-called self-diffusion process, we introduce the probability $P(\boldsymbol{R}, t)$ that the lattice site $\boldsymbol{R}$ on the surface is occupied a time t. The probability that the atom is still at site $\boldsymbol{R}$ at time $t + \Delta t$ can be expressed as

$$P(\boldsymbol{R}, t + \Delta t) = \sum_{\boldsymbol{R}'} \ W(\boldsymbol{R}, \boldsymbol{R}', \Delta t) \ P(\boldsymbol{R}', t) \, . \tag{8.15}$$

Here $W(\boldsymbol{R}, \boldsymbol{R}', \Delta t)$ describes the conditional probability that the atom is at site $\boldsymbol{R}$ at time $t + \Delta t$ given that it was at site $\boldsymbol{R}'$ at time t. Now we assume that only nearest-neighbor (n.n.) jumps can occur and that the time Δt is so short that at most one jump happens during this time. Since k_j is the overall rate that a jump to any of the nearest neighbors occurs, the rate of a jump to a particular nearest neighbor is given by k_j/N where N is the number of nearest neighbors. Then the probability of a jump to this nearest neighbor site within the time Δt is simply $\Delta t \cdot k_\mathrm{j}/N$. Thus we can write the probability W as

$$W(\boldsymbol{R},\boldsymbol{R}',\Delta t) \;=\; \begin{cases} k_{\mathrm{j}}\Delta t/N\;, & \text{if } \boldsymbol{R},\boldsymbol{R}' \text{ n.n.}\;, \\ 1 \;-\; \sum\limits_{n.n.} k_{\mathrm{j}}\Delta t/N\;, & \text{if } \boldsymbol{R} \;=\; \boldsymbol{R}'\;, \\ 0 & \text{else}\;, \end{cases} \tag{8.16}$$

where we have used the fact that W is a probability, i.e., $\sum\limits_{\boldsymbol{R}} W(\boldsymbol{R},\boldsymbol{R}',\Delta t) = 1$. This simply says that if a atom is at site $\boldsymbol{R}'$ at time t, it will also be at some lattice site at time $t+\Delta t$ with certainty (which means that desorption events are not considered).

If we insert (8.16) in (8.15), we obtain

$$P(\boldsymbol{R},t+\Delta t) = \sum_{n.n.} \frac{k_{\mathrm{j}}\Delta t}{N}\; P(\boldsymbol{R}',t) \;+\left(1-\sum_{n.n.} \frac{k_{\mathrm{j}}\Delta t}{N}\right) P(\boldsymbol{R},t)\,. \tag{8.17}$$

Now we subtract $P(\boldsymbol{R},t)$ from both sides of (8.17), divide by Δt, and take the limit $\Delta t \to 0$. This leads to the differential equation

$$\frac{\partial P(\boldsymbol{R},t)}{\partial t} = \frac{k_{\mathrm{j}}}{N} \sum_{n.n.} \left[P(\boldsymbol{R}',t) - P(\boldsymbol{R},t)\right]. \tag{8.18}$$

An equation such as (8.18) is called a *master equation*. In general, master equations give the time dependence of probability distributions of physical observables. Equation (8.18) is valid for diffusion via nearest-neighbor jumps in arbitrary environments. Let us now assume that the jumps are confined to a two-dimensional square lattice with lattice constant a. The number of nearest neighbors is 4. If we now perform a Taylor expansion of $P(\boldsymbol{R}',t)$ at the nearest-neighbor sites, for example in x-direction:

$$P(\boldsymbol{R} \pm a\hat{e}_x,t) = P(\boldsymbol{R},t) \pm a\; \frac{\partial P(\boldsymbol{R},t)}{\partial x} + \frac{a^2}{2}\; \frac{\partial^2 P(\boldsymbol{R},t)}{\partial x^2} \pm \ldots\,, \tag{8.19}$$

where $\hat{e}_x$ is the unit vector in x-direction, we obtain the well-known diffusion equation

$$\frac{\partial P(\boldsymbol{R},t)}{\partial t} = \frac{k_{\mathrm{j}}a^2}{4}\; \nabla^2 P(\boldsymbol{R},t)\,. \tag{8.20}$$

The factor

$$D_s = \frac{k_{\mathrm{j}}a^2}{4} \tag{8.21}$$

is called the *self-diffusion* or *tracer-diffusion coefficient*. It is often denoted by D^*. This coefficient also enters the mean square displacement of the particle on the surface. Let us assume that the adatom was at the origin $\boldsymbol{R} = 0$ at time $t = 0$. After the time t the particle has performed $t \cdot k_{\mathrm{j}}$ jumps, each with a square displacement of a^2. Hence the mean square displacement is given by

$$\begin{aligned} \langle \boldsymbol{R}^2(t)\rangle &= t\; k_{\mathrm{j}}\; a^2 \\ &= 4\; D_s\; t\,. \end{aligned} \tag{8.22}$$

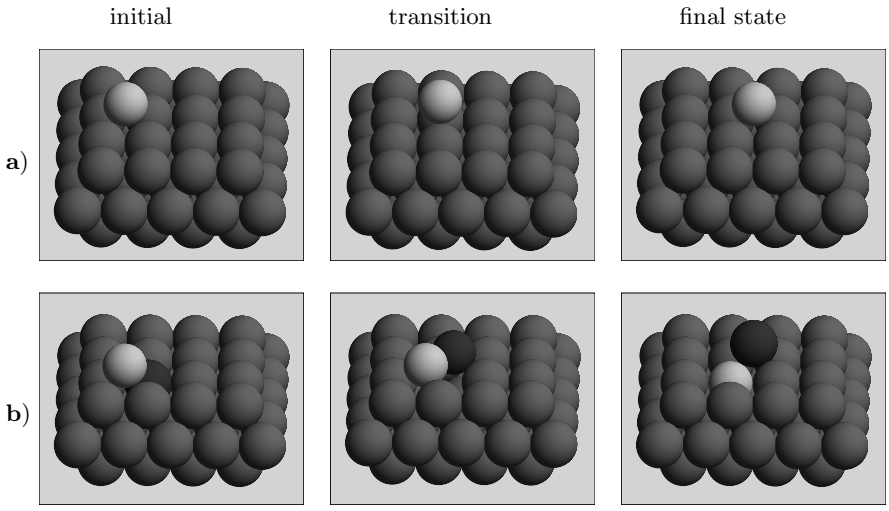

Fig. 8.2. Diffusion mechanisms on a fcc(100) surface. (**a**) hopping diffusion, (**b**) exchange diffusion

In fact, (8.22) is often used to define the self-diffusion coefficient D_s. It is important to note that D_s differs from the chemical diffusion coefficient D_c. Consider an ensemble of particles on the surface. If one assumes that the number of particles stays constant with time, their particle distribution function $n(\boldsymbol{R}, t)$ obeys a conservation law given by a continuity equation

$$\frac{\partial n(\boldsymbol{R}, t)}{\partial t} + \nabla \cdot \boldsymbol{j}(\boldsymbol{R}, t) = 0\,, \tag{8.23}$$

where $\boldsymbol{j}(\boldsymbol{R}, t)$ is the particle current. Now we assume that the particle current is driven by the non-uniformity of the density distribution. The simplest assumption is a linear dependence

$$\boldsymbol{j} = -D_c\ \nabla n(\boldsymbol{R}, t)\,. \tag{8.24}$$

This equation is known as *Fick's law*. Substituting Fick's law into the conservation law yields Fick's second law, the diffusion equation

$$\frac{\partial n(\boldsymbol{R}, t)}{\partial t} = \nabla \cdot (D_c \nabla n(\boldsymbol{R}, t))\,. \tag{8.25}$$

The chemical diffusion coefficient does not describe the motion of a single atom due to thermal fluctuations, but the transport of a large number of atoms due to a gradient in the particle density. In general, D_c depends on the particle density. Only in the case of vanishing particle densities when D_c does not depend on the density any more, D_s and D_c become equal, as a comparison of (8.20) and (8.25) confirms.

The usual mode of surface diffusion is assumed to proceed via hops between adjacent equilibrium adsorption sites (see Fig. 8.2a). This is indeed

9. Electronically Non-adiabatic Processes

So far we have almost entirely dealt with surface processes that proceed in to the electronic ground state. This means that we have assumed that the Born–Oppenheimer approximation is justified. Although there are many important processes at surfaces that involve electronic transitions [305,489,490], the status of the theoretical treatment of processes with electronically excited states is not very satisfactory. Many factors still hamper the development of quantitative models incorporating electronic excitations. Neither the determination of the electronically excited states nor the calculation of coupling matrix elements between these excited states is trivial. But even if the excited states and the coupling between them is known, the simulation of the reaction dynamics with electronic transitions still represents a challenge. In the next sections I will illustrate why the treatment of excited states is so complicated, but I will also show that there are some promising approaches to overcome the problems. In addition, concepts to treat reaction dynamics with electronic transitions will be discussed.

9.1 Determination of Electronically Excited States

In Sect. 4.3, we already saw that for example the GW approximation allows for an accurate determination of the electronic band structure including excited electronic states. However, no total energies can be derived from the GW approximation so that the evaluation of excited state potential energy surfaces is not possible.

In principle, energies of excited states can be determined by quantum chemistry methods. This has in fact been done successfully for the description of electronically nonadiabatic processes at surfaces, as will be shown in Sect. 9.5. Still, quantum chemistry methods are limited to finite systems of a rather small size. Density functional theory, which is so successful for electronic ground state properties of extended system, can not be directly used for electronically excited states since it is in principle an electronic ground-state theory.

Still DFT can be extended to allow the determination of excited states energies, namely in the form of the time-dependent density-functional theory (TDDFT) [491, 492]. It rests on the *Runge–Gross theorem* which is

the analogue to the Hohenberg–Kohn theorem of time-independent density-functional theory. The Runge–Gross theorem states:

> The densities $n(\boldsymbol{r},t)$ and $n'(\boldsymbol{r},t)$ evolving from a common initial state $\Psi_0 = \Psi(t_0)$ under the influence of two potentials $v(\boldsymbol{r},t)$ and $v'(\boldsymbol{r},t)$ are always different provided that the potentials differ by more than a purely time-dependent, i.e. $\boldsymbol{r}$-independent function $v(\boldsymbol{r},t) \neq v'(\boldsymbol{r},t) + c(t)$.

This means that there is an one-to-one mapping between time-dependent potentials and time-dependent densities. However, it is important to note that the functional depends on the initial conditions, i.e. on $\Psi_0 = \Psi(t_0)$. Only if the initial state corresponds to the electronic ground state, the functional is well-defined since then it depends on the density $n(\boldsymbol{r},t)$ alone.

The proof of the Runge-Gross theorem is a little bit more complex than the one for the Hohenberg–Kohn theorem. Still it is not too complicated [492]. Here I only sketch the main ideas of the lines of reasoning. First one shows by using the quantum mechanical equation of motion that the current densities

$$\boldsymbol{j}(\boldsymbol{r},t) = \left\langle \Psi(t) | \hat{\boldsymbol{j}}_p | \Psi(t) \right\rangle \tag{9.1}$$

and

$$\boldsymbol{j}'(\boldsymbol{r},t) = \left\langle \Psi'(t) | \hat{\boldsymbol{j}}_p | \Psi'(t) \right\rangle \tag{9.2}$$

are different for different potentials v and v'. The current densities are related to the density by the continuity equation. By using

$$\frac{\partial}{\partial t}(n(\boldsymbol{r},t) - n'(\boldsymbol{r},t)) = -\nabla \cdot (\boldsymbol{j}(\boldsymbol{r},t) - \boldsymbol{j}'(\boldsymbol{r},t)) \,, \tag{9.3}$$

the one-to-one mapping between time-dependent potentials and densities can be proven.

Still it does not seem to be obvious why time-dependent DFT should lead to the determination of electronic excitation energies. To see this, we have to use linear response theory. We consider an electronic system subject to an external potential of the form

$$v_{\text{ext}}(\boldsymbol{r},t) \;=\; \begin{cases} v_0(\boldsymbol{r}) & ; \quad t \;\leq\; t_0 \\ v_0(\boldsymbol{r}) \;+\; v_1(\boldsymbol{r},t) & ; \quad t \;>\; t_0 \end{cases} \,, \tag{9.4}$$

In perturbation theory, the change of the density due to the external potential $v_1(\boldsymbol{r},t)$ is expanded in powers of v_1, i.e., the density is written as

$$n(\boldsymbol{r},t) = n_0(\boldsymbol{r}) + n_1(\boldsymbol{r},t) + n_2(\boldsymbol{r},t) + \ldots \,, \tag{9.5}$$

where the single terms correspond to the different orders of v_1. The first order or linear response to the perturbation $v_1(\boldsymbol{r},t)$ is given by

$$n_1(\boldsymbol{r},t) = \int dt' \int d^3\boldsymbol{r}' \; \chi(\boldsymbol{r},t,\boldsymbol{r}',t') v_1(\boldsymbol{r}',t') \,, \tag{9.6}$$

where the density-density response function χ is defined as

$$\chi(\boldsymbol{r},t,\boldsymbol{r}',t') \;=\; \left.\frac{\delta n[v_{\rm ext}](\boldsymbol{r},t)}{\delta v_{\rm ext}(\boldsymbol{r}',t')}\right|_{v_0} . \tag{9.7}$$

The Runge–Gross theorem is not only valid for interacting particles, but also for non-interacting particles moving in an external potential $v_s(\boldsymbol{r},t)$. The density-density response function of non-interacting particles with unperturbed density n_0 corresponds to the Kohn–Sham response function and is given by

$$\chi_{\rm s}(\boldsymbol{r},t,\boldsymbol{r}',t') \;=\; \left.\frac{\delta n[v_s](\boldsymbol{r},t)}{\delta v_s(\boldsymbol{r}',t')}\right|_{v_s[n_0]} . \tag{9.8}$$

This linear response formalism can be used in order to determine polarizabilities not only of atoms and molecules [493], but also for large systems. For the fullerene molecule C_{60}, e.g., the results have been quite accurate; however, for polyacetylene chains the conventional exchange-correlation functionals fail [494]. I do not want to address this subject any further, but rather focus on another application of time-dependent DFT, the calculation of excitation energies [492, 495]. The main idea rests on the fact that the frequency-dependent linear response of a finite system, i.e. the Fourier transform of (9.6), has discrete poles at the excitation energies $\Omega_j = E_j - E_0$ of the unperturbed system. By using the functional chain rule, it can be shown that the noninteracting and interacting response functions are related by a Dyson-type equation [492, 495]. This leads to an integral equation for the frequency-dependent linear response $n_1(\boldsymbol{r},\omega)$

$$\int d^3\boldsymbol{x}\; K(\boldsymbol{x},\boldsymbol{r},\omega)\; n_1(\boldsymbol{x},\omega) = \int d^3\boldsymbol{r}'\; \chi_{\rm s}(\boldsymbol{r},\boldsymbol{r}',\omega)\; v_1(\boldsymbol{r}',\omega)\,, \tag{9.9}$$

where the Kernel $K(\boldsymbol{x},\boldsymbol{r},\omega)$ is given by

$$\begin{aligned} K(\boldsymbol{x},\boldsymbol{r},\omega) = \delta(\boldsymbol{r}-\boldsymbol{x}) - \int d^3\boldsymbol{r}'\; \chi_{\rm s}(\boldsymbol{r},\boldsymbol{r}',\omega) \\ \times \left(\frac{1}{|\boldsymbol{r}'-\boldsymbol{x}|} + f_{\rm xc}[n_0](\boldsymbol{r}',\boldsymbol{x},\omega)\right) , \end{aligned} \tag{9.10}$$

with the Fourier transform $f_{\rm xc}[n_0](\boldsymbol{r}',\boldsymbol{x},\omega)$ of the so-called time-dependent exchange-correlation kernel

$$f_{\rm xc}[n_0](\boldsymbol{r},t,\boldsymbol{r}',t') = \left.\frac{\delta v_{\rm xc}[n](\boldsymbol{r},t)}{\delta n(\boldsymbol{r}',t')}\right|_{n_0} . \tag{9.11}$$

Now one uses the fact that the Kohn–Sham excitation energies ω_j are in general not identical with the true excitation energies Ω_j. Hence the right hand side of (9.9) remains finite for $\omega \to \Omega_j$. On the other hand, the exact density response n_1 diverges for $\omega \to \Omega_j$. In order that the integral operator acting on n_1 on the left hand side of (9.9) yields a finite result, the eigenvalues of this integral operator have to vanish. This is equivalent to the statement

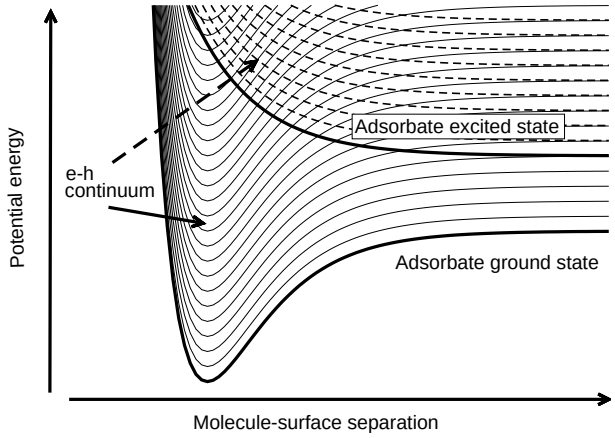

Fig. 9.1. Illustration of electronically excited states in the interaction of atoms or molecules with surfaces

that the true excitation energies Ω are characterized as those frequencies where the eigenvalues $\lambda(\omega)$ of

$$\int d^3\boldsymbol{x} \int d^3\boldsymbol{r}' \; \chi_{\rm s}(\boldsymbol{r},\boldsymbol{r}',\omega) \; \left(\frac{1}{|\boldsymbol{r}'-\boldsymbol{x}|} + f_{\rm xc}[n_0](\boldsymbol{r}',\boldsymbol{x},\omega) \right) \; g(\boldsymbol{r}',\omega)$$
$$= \; \lambda(\omega) \; g(\boldsymbol{r},\omega) \tag{9.12}$$

satisfy $\lambda(\Omega) = 1$. This can easily be shown by performing the integration over the delta function in (9.10). The solution of (9.12) is still not trivial. For practical purposes, further approximations have to be made. If the standard LDA is used in TDDFT for the exchange-correlation functional, then not only locality in space, but also locality in time is assumed. Therefore it is then called the adiabatic local density approximation (ALDA). Analogously, standard GGA functionals become the adiabatic generalized gradient approximation in TDDFT.

9.2 Electronic Excitation Mechanisms at Surfaces

If we consider electronic excitations in the interaction of atoms or molecules with surfaces, we have to distinguish between delocalized excited states of the surface and localized excitations at the adsorbate or the adsorbate-surface bond. These two different kinds of excitation modes are illustrated in Fig. 9.1 where potential energy surfaces reflecting the interaction of a molecule with a surface are plotted.

First of all, the interaction of a molecule with a surface can lead to the excitation of a electron-hole (e-h) pair in the surface. In particular in metals, the electronic states show a continuous spectrum. More importantly, they

are rather delocalized. Hence the local interaction of a molecule with a metal surface will hardly be influenced by the excitation of an electron-hole pair. In Fig. 9.1, this is schematically illustrated by a multitude of shifted ground state potentials. Still, the excitation of an electron-hole pair corresponds to an energy transfer process to the surface that leads to dissipation effects. Thus the influence of the excitation of e–h pairs on the molecule-surface dynamics can be described within a friction-dissipation formalism.

The situation is entirely different in the case of an electronic excitation of the molecule or atom interacting with the surface. Then the shape of the excited-state potential might be entirely different from the ground-state potential. In a theoretical description of such a process usually the potential of the excited state must be explicitly considered. These two scenarios can be considered as the adiabatic and the diabatic limit of electronic transitions at surfaces.

9.3 Reaction Dynamics with Electronic Transitions

In order to couple the direct determination of excited states by electronic structure methods with a dynamical simulation, a full quantum treatment of the system would be desirable. However, this is usually computationally not feasible because of the different mass and time scales associated with nuclei and electrons, respectively. In any case, for atoms heavier than hydrogen or helium a classical description of the reaction dynamics is usually sufficient. Hence a mixed quantum-classical dynamics method is appropriate in which a multi-dimensional classical treatment of the atoms is combined with a quantum description of the electronic degrees of freedom. The crucial issue in mixed quantum-classical dynamics is the self-consistent feedback between the classical and the quantum subsystems. There are two standard approaches that incorporate self-consistency, *mean-field* or *Ehrenfest* and *surface-hopping* methods [496].

These methods are based on the separation of the kinetic energy of the classical particles from the total Hamiltonian

$$H = T_{\boldsymbol{R}} + H_{\mathrm{el}}(\boldsymbol{r}, \boldsymbol{R})\,, \tag{9.13}$$

where $\boldsymbol{R}$ are the classical and $\boldsymbol{r}$ the quantum degrees of freedom. The time evolution of the quantum wave function is then given by the time-dependent Schrödinger equation using the electronic Hamiltonian H_{el}

$$i\hbar\frac{\partial}{\partial t}\;\psi(\boldsymbol{r}, \boldsymbol{R}, t) = H_{\mathrm{el}}(\boldsymbol{r}, \boldsymbol{R}(t))\;\psi(\boldsymbol{r}, \boldsymbol{R}, t)\,, \tag{9.14}$$

where the coordinates $\boldsymbol{R}$ of the classical degrees of freedom enter as parameters. In both the mean-field and the surface-hopping methods, the quantum particles are subject to a Hamiltonian that varies in time due to the motion of

the classical particles. On the other hand, the quantum state of the system determines the forces that act on the classical particles. Thus the self-consistent feedback cycle between quantum and classical particles is realized.

The difference between the two methods lies in the treatment of the back-response of the classical system to quantum transitions. In the mean-field method, the motion of the classical particles is determined by a single effective potential that corresponds to an average over quantum states

$$M_I \frac{d^2}{dt^2} \boldsymbol{R}_I = -\nabla_{\boldsymbol{R}_I} \big\langle \psi(\boldsymbol{r}, \boldsymbol{R}) | H_{\mathrm{el}}(\boldsymbol{r}, \boldsymbol{R}) | \psi(\boldsymbol{r}, \boldsymbol{R}) \big\rangle \,, \tag{9.15}$$

which, using the Hellmann–Feynman theorem, can be transformed to

$$M_I \frac{d^2}{dt^2} \boldsymbol{R}_I = -\big\langle \psi(\boldsymbol{r}, \boldsymbol{R}) | \nabla_{\boldsymbol{R}_I} H_{\mathrm{el}}(\boldsymbol{r}, \boldsymbol{R}) | \psi(\boldsymbol{r}, \boldsymbol{R}) \big\rangle \,. \tag{9.16}$$

The mean-field approach properly conserves the total energy, furthermore it does not depend on the choice of the quantum representation since the wave function can be directly obtained by the numerical propagation of the wave packet using (9.14). However, this approach violates microscopic reversibility, and it is subject to the deficiency of all mean-field methods: the classical path is mainly determined by the major channel trajectory so that branching and correlation effects in the time-evolution are not appropriately accounted for.

A proper treatment of the correlation between quantum and classical motion requires a distinct classical path for each quantum state. This is in fact fulfilled in the surface-hopping method. In this approach, the wave function is expanded in terms of a set of basis functions

$$\psi(\boldsymbol{r}, \boldsymbol{R}, t) = \sum_j c_j(t) \phi_j(\boldsymbol{r}, \boldsymbol{R}) \,. \tag{9.17}$$

With respect to this basis, matrix elements of the electronic Hamiltonian are constructed

$$V_{ij} = \big\langle \phi_i(\boldsymbol{r}, \boldsymbol{R}) | H_{\mathrm{el}}(\boldsymbol{r}, \boldsymbol{R}) | \phi_j(\boldsymbol{r}, \boldsymbol{R}) \big\rangle \,. \tag{9.18}$$

Furthermore, the *nonadiabatic coupling vector* is defined as

$$\boldsymbol{d}_{ij} = \big\langle \phi_i(\boldsymbol{r}, \boldsymbol{R}) | \nabla_{\boldsymbol{R}} | \phi_j(\boldsymbol{r}, \boldsymbol{R}) \big\rangle \,, \tag{9.19}$$

where the gradient is taken with respect to all atomic coordinates $\boldsymbol{R}$. Inserting the wave function (9.17) into (9.14), one obtains [497] (see Exercise 9.2)

$$i\hbar \dot{c}_k = \sum_j c_j (V_{kj} - i\hbar \dot{\boldsymbol{R}} \cdot \boldsymbol{d}_{kj}) \,. \tag{9.20}$$

In the adiabatic representation, the matrix elements V_{kj} are zero while in a diabatic representation the nonadiabatic coupling vector vanishes.

In any surface-hopping method, the classical particles move on the potential energy of one particular quantum state subject to the classical equation of motion

$$M_I \frac{d^2}{dt^2} \boldsymbol{R}_I = -\nabla_{\boldsymbol{R}_I} \left\langle \phi_i(\boldsymbol{r}, \boldsymbol{R}) | H_{\mathrm{el}}(\boldsymbol{r}, \boldsymbol{R}) | \phi_i(\boldsymbol{r}, \boldsymbol{R}) \right\rangle . \tag{9.21}$$

At the same time, the set of coupled differential equations (9.20) is solved in order to obtain the amplitudes c_j of each electronic quantum state. What is left, is the specification of a rule for the switches or jumps between the different potential energy surfaces. This rule can in fact not be uniquely defined so that many different algorithms exist (see, e.g., [498]). One particularly elegant method is the so-called *fewest-switches algorithm* [497] which is a variationally-based hopping algorithm that guarantees the correct population $|c_j(t)|$ of each state in an ensemble of many calculated trajectories with the minimum number of hops (see Exercise 9.3).

There are also caveats of surface hopping algorithms. They are not independent of the quantum representation [497,499], and there is some ambiguity in the velocity adjustment if $V_{kk}(\boldsymbol{R}) \neq V_{ll}(\boldsymbol{R})$ at the position of the switch between state k and l. In addition, they are computationally more demanding than mean-field methods, and in fact there are cases for which the mean-field method is more accurate [496]. We will first discuss processes that can be treated within a mean-field formalism.

9.4 Electronic Friction Effects

The determination of the role of electron-hole pairs in the scattering and sticking of molecules at surfaces is rather cumbersome. There are hardly any reliable studies where the influence of the e-h pairs has been investigated from first-principles. Hence there is also no accepted viewpoint about the importance of the e–h pairs. It seems that whenever there are some unclear results in sticking or scattering experiments, e–h pairs are made responsible. Equivalently, the validity of Born–Oppenheimer molecular dynamics simulations is often questioned because of the neglect of e–h pair excitations.

Using a thin polycrystalline Ag film deposited on n-type Si(111) as a Schottky diode device, the nonadiabatically generated electron-hole pairs upon both atomic and molecular chemisorption can be detected [500, 501]. A strong correlation between the adsorption energy and the measured *chemicurrent* has been observed. For NO adsorption on Ag (adsorption energy $\sim 1\,\mathrm{eV}$), it has been estimated that one quarter of the adsorption energy is dissipated to electron-hole pairs. Adsorption-induced electron hole-pair creation has also been found for other metal substrates, such as Au, Pt, Pd, Cu, Ni or Fe, and even for semiconductors such as GaAs and Ge [500, 502].

The understanding of this nonadiabatic dissipation channel is still rather incomplete. There are, however, theoretical studies that used ab initio input in order to assess the effects of electron-hole pair excitations in adsorption and reaction processes on surfaces. An approach based on time-dependent density functional theory was used in order to estimate the electron-hole

10. Perspectives

Traditionally, surface science studies have focused on the investigation of low-index single crystal surfaces and the interaction of atoms and simple molecules with them. As shown in the previous chapters, the focus in experimental as well as theoretical surface science shifts more and more to surfaces with well-defined defects such as for example the steps of vicinal surfaces. However, even more complex systems have become the subject of microscopic studies [541]. In this final chapter I present some examples of such microscopic studies based on ab initio electronic structure calculations. The examples do not only show the state of the art but they also indicate the promising perspective and future directions of theoretical research in surface science.

10.1 Solid-liquid Interface

All the examples presented so far have been concerned with solid surfaces either in vacuum or interacting with gas particles, i.e. we did not consider any liquids in contact with a solid surface. Still, the solid-liquid interface is of significant importance in the fields of electrochemistry and electrocatalysis which deal with reactions of molecule at this interface [542]. Such reactions are of enormous technological relevance, for example with respect to the development of more efficient fuel cells. In theoretical surface science, however, the solid-liquid interface has hardly been studied microscopically yet because of the difficulties in the reliable description of both the liquid or electrolyte and the solid surface. Often electronic structure studies addressing electrochemical systems omit the description of the electrolyte with the hope that the influence of it on, e.g., adsorption and reaction properties of molecules is negligible [543].

In principle, it is not particularly difficult to include a liquid in periodic supercell calculations. Instead of leaving the region between the slabs empty, it can well be filled with the liquid. This is illustrated in Fig. 10.1. Indeed there are first supercell calculations that have addressed surface energies and structures [544, 545] and even reactions at the solid-liquid interface. A particularly impressive study addressed the deprotonation of acetic acid (CH_3COOH) over Pd(111) [546]. In this study, DFT calculations were performed in order

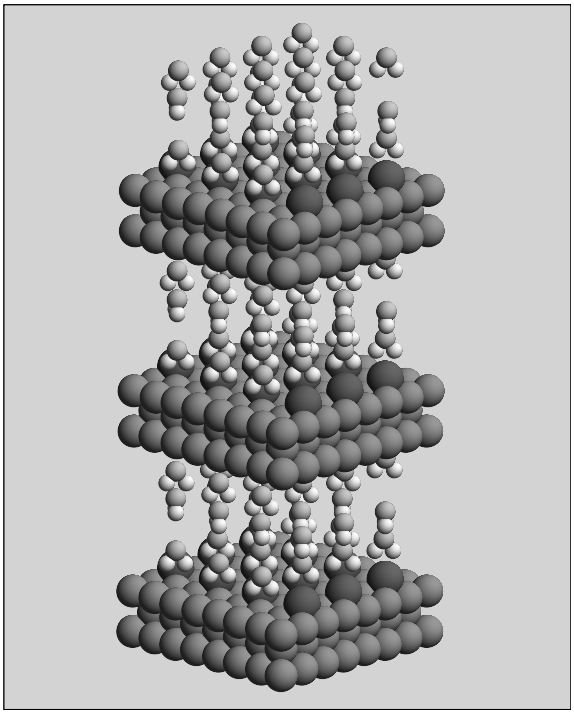

Fig. 10.1. Illustration of the description of the solid-liquid interface within the supercell approach in periodic electronic structure calculations. The region between the adsorbate covered slabs is filled with water molecules

to examine how solvating molecules influence the bond-breaking and bond-making process at metal surfaces. The dissociation of acetic acid into the acetate anion and a proton is highly endothermic in the gas phase. However, the DFT calculations found that this dissociation is almost thermoneutral in the presence of water molecules [546]. The dissociation is facilitated in an aqueous environment since the fragments which are highly unstable when formed in the gas phase become stabilized by the solvation. The Pd(111) surface also catalyzes the deprotonation of acetic acid and strongly binds the acetate intermediates, but the dissociative adsorption is more endothermic than the dissociation in water without the metal surface. The dissociation is even less favorable at Pd(111) if water is present at the surface because the solvating water molecules weaken the interaction of the acetic acid with the Pd(111) surface.

In the field of electrochemistry, the knowledge about reaction steps and mechanisms at the liquid-solid interface is still rather limited. Therefore there is a strong need for studies like the one just presented which will open the way to a microscopic description and analysis of electrocatalytic reactions. However, there is an additional problem associated with the theoretical descrip-

tion of electrochemical processes, namely the correct treatment of applied external fields always present in electrochemistry.

There have already been several attempts to model external fields or the electrochemical potential within the DFT slab approach. An external field can be explicitly included by using a dipole layer in the vacuum region between the slabs [547, 548], but in such an approach only a thin liquid layer covering the electrode can be modeled, and the evaluation of the corresponding electrochemical potential is not trivial. The electrochemical potential can be introduced by charging the slab which is counterbalanced by a homogeneous background charge [549–551], but this also introduces an interaction between the charged slab and the background charge which has to be subtracted from the total energy.

In yet another approach [552], hydrogen atoms are added to a water bilayer outside the slab. The hydrogen atoms become solvated as protons leading to the formation of hydronium ions (H_3O^+), and the electrons move to the metal electrode. By changing the hydrogen concentration, the surface charge and hence the electrochemical potential can be varied. However, the excess hydrogen atoms have to be kept fixed because otherwise they would propagate towards the surface. This can introduce errors due to geometrical constraints. It is certainly fair to say that there is still enough room for improvements in the realistic theoretical description of solid-liquid interfaces in the presence of external fields.

10.2 Nanostructured Surfaces

The last years have seen a tremendous interest in the so-called nanoscience and nanotechnology. Small particles or clusters with sizes in the nanometer range show strongly modified electronical, optical and chemical properties, compared to bulk materials. The research on nanosized particles has been fueled by the hope that the modified properties can be used to build new or better devices or chemical reactors [129].

The theoretical treatment of nanosized particles by electronic structure theory methods represents a great challenge. Due to the large number of symmetrically different atoms in nanostructures, the numerical effort required to treat these structures is enormous. On the other hand, there is definitely a need for the microscopic description of nanoparticles because the knowledge of the underlying mechanism leading to the modified nature of the particles is still rather limited. It is often not clear whether the specific properties are caused by the reduced dimension of the particles ("quantum size effects") or by the large surface area of the nanocluster where furthermore often many defects are present.

One of the most remarkable modifications of the properties of a material by going from the bulk to nanoscale particles has been found with respect to the catalytic activity of gold. While gold as a bulk material is chemically

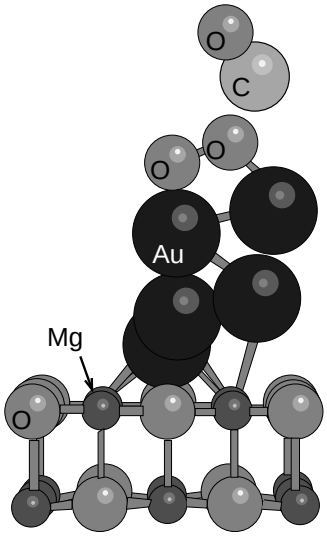

Fig. 10.2. CO oxidation on an Au_8 cluster adsorbed on a MgO(100) surface containing an oxygen-vacancy F-center. Due to the perspective, not all Au atoms are visible. A snapshot of a CO molecule approaching an adsorbed oxygen molecule is shown. (After [555])

inert [189], nanoscale gold particles supported on various oxides show a surprisingly large catalytic activity, especially for the low-temperature oxidation of CO [553, 554].

In a collaboration between experiment and electronic structure theory, the CO oxidation catalyzed by size-selected Au_n clusters with $n \leq 20$ supported on defect-poor and defect rich MgO(100) films has been investigated [555]. The experiments revealed that the gold clusters deposited on defect-rich MgO-films have a dramatically increased activity compared to clusters deposited on defect-poor films at temperature between 200 and 350 K. Furthermore, the Au_8 cluster was found to be the smallest catalytically active particle.

In order to explore the microscopic mechanisms underlying the observed behavior, LDA-DFT calculations have been performed [555]. Between 27 and 107 substrate atoms have been embedded into a lattice of about $2000 \pm 2\,\mathrm{e}$ point charges at the positions of the MgO lattice. In order to model the defect-rich substrate, an oxygen vacancy was introduced at the MgO(100) surface which is called a colour center or F-center (from German "Farbzentrum") because of its optical properties. The equilibrium shape of a Au_8 cluster adsorbed on the defect-free MgO surface and on the F-center was determined and reaction paths of the CO oxidation catalyzed by the Au_8 cluster were explored. Figure 10.2 shows a side view of the Au_8 cluster adsorbed on the F-center. The structure corresponds to a deformed close-packed stacking. A sizable charge transfer of $0.5\,\mathrm{e}$ from the MgO(100) surface to the gold octamer has been found.

In addition, a snapshot along the CO oxidation path according to an abstraction or so-called *Eley–Rideal mechanism* is shown. A CO molecule

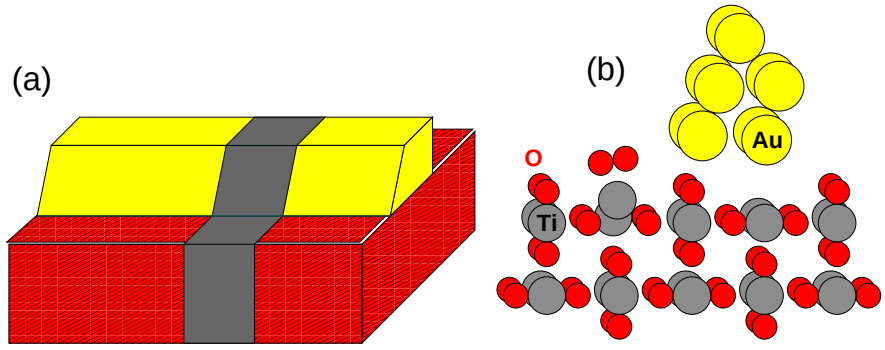

Fig. 10.3. One-dimensional rod model for the adsorption of O_2 an Au/TiO_2 nanoparticles used in GGA-DFT calculations. a) Illustration of the rod geometry. The dark-shaded area indicates the lateral extension of the unit cell. b) Relaxed structure of O_2 binding at the Ti trough close to a supported one-dimensional Au rod with a sharp Au edge (after [556, 557]).

approaches an adsorbed O_2 molecule and reacts spontaneously to form a weakly bound ($\sim$ 0.2 eV) CO_2 molecule that can directly desorb plus an adsorbed oxygen atom. Recall that although the CO oxidation is strongly exothermic, it is hindered by a large activation barrier in the gas phase. Another reaction pathway of the Langmuir-Hinshelwood type where the two reactants are initially coadsorbed on the top-facet of the Au_8 cluster has also been found with a similarly small barrier. Through these reaction channels the low-temperature CO oxidation down to 90 K can proceed. As far as the higher-temperature oxidation is concerned, further channels have been identified at the periphery of the gold cluster. Their barriers are much smaller at the Au_8 cluster adsorbed above the F-center than on the perfect surface giving an explanation for the enhanced activity of the clusters on the defect-rich substrate.

In general, supported clusters studied in the experiments are significantly larger than those accessible to first-principles electronic structure calculations where the number of clusters atoms is typically below 10, as just demonstrated. For example, the Au clusters deposited on $TiO_2(110)$ that exhibit a surprisingly high catalytic activity for the low-temperature oxidation of CO have a diameter of 3 nm [553, 554] which means that they contain several hundreds of atoms and thus are not accessible by DFT calculations. Still one can address binding of O_2 and CO to such supported nanoparticles by replacing the supported nanoparticle with one-dimensional rods [556,557]. This approach is illustrated schematically in Fig. 10.3a. One side of the rod was modeled according to the local bonding situation of the Au atoms at the edge of the supported nanoparticles while the other side of the rod only served the correct boundary conditions towards the interior of the supported clusters. Thus it could be shown that the adsorption of O_2 on top of a Ti trough

atom is strongly stabilized by the presence of an adjacent Au cluster with its edge above the bridging O atoms of the $TiO_2(110)$ surface (see Fig. 10.3b), resulting in a binding energy of 0.45 eV. In contrast, on clean, stoichiometric $TiO_2(110)$, O_2 does not bind [558].

10.3 Biologically Relevant Systems

Molecules relevant in biology, biochemistry and biological surface science [559] are usually much too complex to be fully treated by ab initio electronic structure methods. Typically, classical force field methods dominate in the simulation of biomolecular systems. However, these methods do not give any information about the electronic structure. These information can be obtained by mixed quantum-classical embedding schemes in which the active center treated by electronic structure methods is embedded in a classical potential of the remaining atoms at the periphery. This QM/MM (Quantum Mechanics/Molecular Mechanics) hybrid method [560] has been used successfully for, e.g., the simulation of enzymatic systems [64].

When the biomolecular systems are relatively simple, they can in fact nowadays be fully treated by periodic calculations [561]. However, using current DFT functionals, one faces one severe problem: The interaction of organic molecules with substrates and between organic molecules themselves is often dominated by weak van der Waals or dispersion forces which are often refered to as dispersion forces in quantum chemistry. Hence, one is often in a dilemma if one wants to treat the adsorption of organic molecules on substrates: For the description of the substrate a periodic DFT code is required in order to take the delocalized nature of the substrate states into account, but the functionals do not appropriately reproduce the weak van der Waals interaction necessary for an adequate treatment of the organic molecules.

One possibility to deal with this problem is to simply add the van der Waals interaction between to atoms i and j explicitly, e.g. via the London dispersion formula [562]

$$E_{ij}^{\mathrm{vdW}}(r) \;=\; -\frac{3}{2r^6}\frac{\alpha_i \alpha_j I_i I_j}{I_i + I_j} \tag{10.1}$$

This method has been successfully used to describe the interaction of the DNA base adenine with graphite [563]. However, due to the fact that GGA already contains some correlation effects, the additional van der Waals term has to be modified in an empirical way which depends on the particular system looked at. This is not very satisfactorily from a fundamental point of view.

One promising hybrid approach to treat dispersion effects in extended systems from first principles has recently been proposed [564–566] which is based on the observation that the error due to exchange-correlation effects

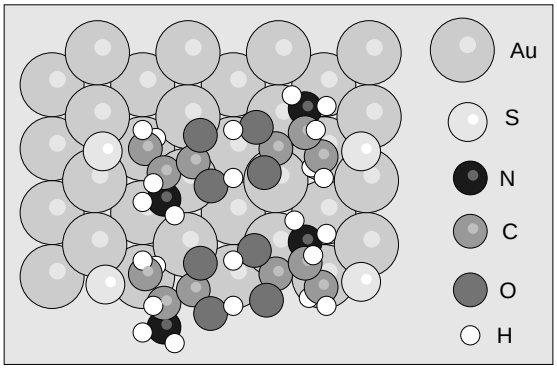

Fig. 10.4. The energetically most stable configuration of the amino acid cysteine on Au(110) calculated by DFT calculations [568]. It corresponds to two units of the double row structure of D cysteine.

converges rather rapidly with the size of the system. Hence one can determine the error due to the inaccuracy of the chosen DFT exchange correlation functional by doing cluster calculations. In practice, one starts by doing a DFT calculation for the extended periodic system. Then a cluster with the same geometry as the extended system is chosen, and for this cluster the difference between DFT and any appropriate post-HF method (see section 3.2) that takes the many-body effects correctly into account is evaluated. The corrected energy is then obtained by

$$E_{\text{hybrid}} = E(\text{DFT})_{\text{extended}} + E(\text{post} - \text{HF})_{\text{Cluster}} - E(\text{DFT})_{\text{Cluster}} \,. \quad (10.2)$$

If necessary, cluster of different sizes can be employed in order to obtain converged correction terms. This approach has for example successfully been applied to protonation reactions of isobutene in a zeolite [565] where for the clusters the MP2 method has been used in order to derive a damped dispersion expression (10.1) for the dispersion effects between the zeolite catalyst and the hydrocarbon species.

If the interaction of the organic molecules with the substrate is governed by strong bonds, as for example in the case of the interaction of thiols with gold because of the strong Au-S bond, current DFT functionals are able to give reliable results. As an example, we consider the adsorption of cysteine ($HS\text{-}CH_2\text{-}CH(NH_2)\text{-}COOH$), an amino acid, on Au(110) which has been investigated by both STM experiments and DFT calculations [567, 568]. Cysteine exists in two different so-called enantiomeric forms, L-cysteine and D-cysteine, i.e. two forms that are each others' mirror image with different chirality. The STM experiments have found a high stereoselectivity in the dimerization of adsorbed cysteine molecules on the Au(110) surface which reconstructs in the missing-row structure. Only either LL pairs or DD pairs have been identified.

These findings have been rationalized by DFT-GGA calculations [567]. The calculated most favourable adsorption configuration for a DD-cysteine dimer on Au(110) is illustrated in Fig. 10.4. The presence of sulfur causes the formation of four vacancies on the gold rows due to the tendency of sulfur to bind to low-coordinated atoms. Since sulfur prefers the bridge site, the DD dimer is slightly rotated. In this configuration, three bonds are formed which mainly stabilize this structure: sulphur–gold, amino–gold and carboxylic–carboxylic. In any possible LD dimer adsorption structure, at least one of these bonds is lost, making the LD dimer energetically unfavourable. This explains the high selectivity observed in the STM experiments and fits into the picture that chiral recognition might be in general driven by the formation of three-point contacts [569].

In the STM experiments, not only isolated cysteine dimers are found, but also extended molecular dimer rows [568]. In fact, Fig. 10.4 shows the energetically most stable structure of these rows. The driving force for the formation of these rows is the fact that the formation energy of the four-adatom vacancy on Au(110) required for the adsorption of cysteine is considerably lowered adjacent to already existing vacancies. Hence ones a cysteine dimer is adsorbed forming a first double-row unit, additional cysteine dimers will preferentially attach to the existing dimer instead of forming isolated adsorbates. Thus unidirectional, self-assemblied molecular nanowires can be formed even in the absence of any significant direct adsorbate-adsorbate interaction along the growth direction.

10.4 Industrial Applications

Quantum chemistry methods based on Hartree-Fock theory have been an integral part of research and development in the chemical and pharmaceutical industry for some decades. Companies which manufacture products for which surface structures are relevant have been much more reluctant to employ first-principles electronic structure methods. This is caused by the fact that surface structures that are employed for industrial purposes are usually far away from being perfect. Cluster or slab calculations containing in the order of 100 atoms are therefore often not directly relevant for the research and development process of new catalysts or semiconductor devices. Still, although it is impossible to create new products theoretically from the scratch (and probably will remain impossible for a long time), electronic structure calculations can still add valuable information to the research and development process, in particular for properties where measurements are much more time consuming or not possible [570].

This has already been realized by some manufacturers in the semiconductor and chemical industry. One of the first examples of a successful collaboration between fundamental academic research, both experimental and theoretical, and industrial development has led to the design of a new catalyst

for the steam-reforming process [571]. Here I will focus on the contribution of electronic structure calculations [257, 571] to the design of the catalyst; the corresponding experiments have already been reviewed in detail [572].

In the steam-reforming process, hydrocarbon molecules (mainly CH_4) and water are converted into H_2 and CO. This is a important process of great technological relevance since it is the first step for several large scale chemical processes such as ammonia synthesis, methanol production or reactions that need H_2 [572]. The catalysts usually used for this reaction are based on Ni. However, during the catalyzed reaction also an unwanted by-product, namely graphite, is formed. A graphite overlayer on the Ni surface leads to a poisoning of the reaction, i.e., it lowers the activity of the catalyst. Such poisoning processes are very costly since they reduce the time the catalyst can be used so that they require a more frequent maintenance of the reactor unit in the chemical plant.

One way of changing the reactivity of metal surfaces is to modify their chemical composition by alloying them with other metals. Some metals that are immiscible in the bulk may still be able to form alloys at the surface. Au and Ni is such a system. The rate-limiting process in the steam-reforming process on Ni is the dissociation of CH_4 into CH_3 and H. DFT calculations by Kratzer et al. showed that this process is hindered by a relatively high barrier of 1.1 eV on Ni(111) [257]. If a Ni atom on the (111) surface has one or two Au atoms as neighbors, this barrier is even increased by 165 meV and 330 meV, respectively. Due to the fact that Au is a noble metal, the CH_4 dissociation barrier over the Au atom is even much higher [571]. An analysis of the calculated electronic structure revealed that the presence of neighboring Au atoms leads to a downshift of the d states at the Ni atom which reduces the reactivity at the Ni atoms [189]. Hence alloying a Ni surface with Au atoms leads to a reduced activity of the catalyst. However, DFT calculations also demonstrated [571] that the presence of the Au atoms lowers the chemisorption energy considerably for C atoms on Ni. If carbon is less strongly bound to the surface, the formation of CO becomes more likely which prevents the building up of a graphite layer.

Altogether, the DFT calculations showed that the lowering of the C chemisorption energy by alloying Ni with Au is much more effective than the increase of the CH_4 dissociation barrier. Hence one ends up with a catalyst that is slightly less reactive but much more robust and stable due to its higher resistance to graphite formation. These fundamental theoretical results together with experimental studies have led to the design of a new catalyst that is now patented [572].

Besides this application for the development of better catalysts, DFT calculations have for example also contributed to the research and development process with respect to the equipment simulation in the electronic industry [573] and in the manufacturing of discharge fluorescent lamps [574]. Recent example of the impact of DFT on materials research are collected in

an issue of the *MRS Bulletin* [575]. However, although the number of DFT applications in industry is increasing, it is fair to say that there is still a long way to go before DFT calculations will become generally accepted as a valuable tool industrial research.